



Swansea University
Prifysgol Abertawe



Swansea University E-Theses

Scanning near-field optical microscopy studies of cell membrane proteins labelled with fluorescent quantum dots.

Walker, Kelly-Ann D

How to cite:

Walker, Kelly-Ann D (2010) *Scanning near-field optical microscopy studies of cell membrane proteins labelled with fluorescent quantum dots..* thesis, Swansea University.

<http://cronfa.swan.ac.uk/Record/cronfa43114>

Use policy:

This item is brought to you by Swansea University. Any person downloading material is agreeing to abide by the terms of the repository licence: copies of full text items may be used or reproduced in any format or medium, without prior permission for personal research or study, educational or non-commercial purposes only. The copyright for any work remains with the original author unless otherwise specified. The full-text must not be sold in any format or medium without the formal permission of the copyright holder. Permission for multiple reproductions should be obtained from the original author.

Authors are personally responsible for adhering to copyright and publisher restrictions when uploading content to the repository.

Please link to the metadata record in the Swansea University repository, Cronfa (link given in the citation reference above.)

<http://www.swansea.ac.uk/library/researchsupport/ris-support/>



Swansea University
Prifysgol Abertawe

**Scanning near-field optical microscopy studies of
cell membrane proteins labelled with fluorescent
quantum dots**

Kelly-Ann D Walker BSc (Hons) AMInstP

Submitted to Swansea University in the fulfilment of the
requirements for the degree of Doctor of Philosophy

2010

ProQuest Number: 10821506

All rights reserved

INFORMATION TO ALL USERS

The quality of this reproduction is dependent upon the quality of the copy submitted.

In the unlikely event that the author did not send a complete manuscript and there are missing pages, these will be noted. Also, if material had to be removed, a note will indicate the deletion.



ProQuest 10821506

Published by ProQuest LLC (2018). Copyright of the Dissertation is held by the Author.

All rights reserved.

This work is protected against unauthorized copying under Title 17, United States Code
Microform Edition © ProQuest LLC.

ProQuest LLC.
789 East Eisenhower Parkway
P.O. Box 1346
Ann Arbor, MI 48106 – 1346



Declaration

This work has not previously been accepted in substance for any degree and is not being concurrently submitted in candidature for any degree.

Signed (candidate)

Date

Statement 1

This thesis is the result of my own investigations, except where otherwise stated. Where correction services have been used, the extent and nature of the correction is clearly marked in a footnote(s).

Other sources are acknowledged by footnotes giving explicit references. A bibliography is appended.

Signed (candidate)

Date

Statement 2

I hereby give consent for my thesis, if accepted, to be available for photocopying and for inter-library loan, and for the title and summary to be made available to outside organisations.

Signed (candidate)

Date

Abstract

Scanning near-field optical microscopy (SNOM) has been employed to simultaneously acquire high-resolution fluorescence images along with shear-force atomic force microscopy of cell membranes. Implementing such a technique overcomes the limits of optical diffraction found in standard fluorescence microscopy and also yields vital topographic information. However, one of the biggest challenges of imaging fluorescent biological specimens with SNOM, is the photostability and low yield of fluorescent labelling agents. Semiconductor quantum dots are a recently developed class of fluorophores which exhibit superior optical properties. They are significantly brighter and more resistant to photo-degradation than organic fluorophores.

In this study, SNOM has been utilised in conjunction with quantum dot labelling to interrogate the biomolecular composition of cell membranes. The technique has been applied to investigate cell-cell adhesion in human epithelial cells. This has been realised through immunofluorescence labelling of the cell-cell adhesion protein E-cadherin. Moreover, a dual labelling protocol has been optimised to facilitate a comparative study of the adhesion mechanisms, and the effect of aberrant adhesion protein expression, in both healthy and cancerous epithelial cells.

This study reports clear differences in the morphology and phenotype of healthy and cancerous cells. In healthy prostate epithelial cells (PNT2 cells), E-cadherin was predominantly located along the cell periphery and within filopodial protrusion. The presence of E-cadherin appeared to be enhanced when cell-cell contact was established. Furthermore this study has revealed the interactions of filopodia and their functional relationship in establishing adherens junctions in PNT2 cells.

In contrast, examination of metastatic prostate cancer cells (PC-3 cells) revealed E-cadherin to be predominantly localised around the nuclear region of the cell, with no E-cadherin labelling around the periphery of the cells. This lack of functional E-cadherin in PC-3 cells coincided with a markedly different morphology and PC-3 cells were not observed to form tight cell-cell associations with their neighbours.

Facilitated by the high-resolution imaging afforded by the SNOM technique, this research further highlights the important role that E-cadherin plays in the development of invasive, metastatic cancers.

Acknowledgements

Although writing this thesis seemed at times an insurmountable task, knowing that I had the support of the following people made the process more manageable.

Firstly I would like to thank my supervisor Dr. Peter Dunstan for having confidence in my abilities and giving me the opportunity to work on this project. I am grateful for the vital encouragement, support and guidance Peter has provided throughout the duration of my studies.

I would also like to thank Dr. Shareen Doak for providing the opportunity to collaborate on this project and whose door has always been open to offer help and advice.

During my studies, I have had the opportunity to work alongside many talented researchers and research staff within the Physics Department. The members of my research group, Dr Mark Holton, Dr Omar Alhartomy and Jonathan Lloyd have an unparalleled amount of patience have been a great source of help and support. I would particularly like to express my thanks to Mark Holton for never laughing at the silly questions and always being at the end of the phone. Special thanks go to Julian Kivell and Hugh Thomas for their technical support and cups of tea, but mostly for their words of encouragement towards the end of my studies.

I have been lucky enough to cross disciplines and work with researchers from the Institute of Life Science. I am grateful to Margaret Clatworthy and Sally James for their help with all things biological and the many friends in the Institute of Life Science who have always been on hand to help me find my way around the lab.

For their endless support, encouragement and even bribery, I'd like to thank my family for always believing in my abilities.

Contents

1	Introduction	1
1.1	Classical microscopy and the diffraction limit	1
1.2	Super-resolution microscopy	2
1.3	Scanning near-field optical microscopy in biology	4
1.4	A new class of fluorescent probes	5
1.5	Thesis outline	6
2	Fluorescence	12
2.1	Introduction	12
2.2	Principles of fluorescence	13
2.2.1	Photoluminescence	13
2.2.2	Fluorescence spectra	14
2.2.3	Photobleaching	15
2.2.4	Quantum yield	16
2.2.5	Fluorescent lifetime	16
2.2.6	Quenching	17
2.2.7	Förster resonance energy transfer (FRET)	18
2.3	Semiconductor quantum dots	19
2.3.1	Introduction	19
2.3.2	Bulk semiconductors	20
2.4	Effects of quantum Confinement	23
2.4.1	Quantum dots	23
2.5	Synthesis and properties of quantum dots	26
2.5.1	Solvent synthesis	26

2.5.2	Core/shell quantum dots	27
2.5.3	Surface functionalisation for bio-medical applications . . .	27
2.5.4	Properties for bio-medical applications	28
2.6	Summary	30
3	Scanning near-field optical microscopy	35
3.1	Introduction	35
3.2	Optical resolution	36
3.3	Evanescent waves	38
3.4	Theory of SNOM	40
3.5	Heisenberg principle and near-field resolution	41
3.6	Development of SNOM	43
3.7	Applications and typical set-up	44
3.8	SNOM probes	45
3.8.1	Operational modes	45
3.8.2	Manufacture	46
3.9	Scanning technique	47
3.9.1	Feedback mechanism	47
3.9.2	Signal detection	47
3.10	FRET SNOM	48
3.10.1	Introduction	48
3.10.2	Realisation of active probes	49
3.11	Summary	50
4	Cell biology	56
4.1	Introduction to human cell biology	56
4.2	Adhesion mechanisms	58
4.2.1	E-cadherin and the adherens junction	60
4.2.2	Role of actin filaments and filopodia	61
4.3	Cancer	62
4.3.1	Aberrent adhesion in prostate cancer	65
4.4	Fluorescent labelling of target proteins <i>in situ</i>	67

4.5	Summary	69
5	Experimental procedures	75
5.1	Introduction	75
5.2	Equipment	75
5.2.1	Scanning near-field optical microscopy	75
5.2.2	Fluorescence microscopy	77
5.2.3	Modifications to facilitate imaging of biological materials	78
5.3	Image acquisition	82
5.3.1	Scanning parameters	82
5.3.2	Image processing	84
5.4	Preparation of biological samples	85
5.4.1	Sample preparations	85
5.4.2	Permeabilisation, fluorescent labelling and washing	87
5.5	Summary	92
6	Results: SNOM imaging of biological materials	95
6.1	Introduction	95
6.2	Development of fluorescent biological samples	96
6.2.1	Sample requirements	96
6.2.2	Organic labelling of membrane proteins	98
6.2.3	Quantum dot labelling of cytoskeletal proteins	103
6.3	Quantum dot labelling of E-cadherin	108
6.3.1	Development of methodology	108
6.3.2	Functional analysis of E-cadherin in confluent PNT2 samples	109
6.3.3	E-cadherin in non-confluent PNT2 samples	112
6.4	Conclusion	114
7	Results: Multiplexing with semiconductor quantum dots	119
7.1	Motivation for multiplexing	119
7.2	Development of multiplexed samples	120
7.2.1	Protocol tests	123

7.2.2	Further optimisation	127
7.3	Results of multiplexing in PNT2 cells	129
7.3.1	Spectral analysis	129
7.3.2	Multiplexing in PNT2	131
7.4	Structural analysis of PC-3 cells	135
7.5	Optimisation of dual labelling in PC-3	139
7.6	Results of multiplexing in PC-3	140
7.7	Conclusion	144
8	Conclusions	148
8.1	Comparison of E-cadherin distribution	148
8.2	Multiplexed detection using quantum dots	151
8.3	Difficulties addressed	152
8.4	Future directions	154

Abbreviations

AFM	Atomic Force Microscopy
APD	Avalanche Photodiode
BSA	Bovine Serum Albumin
CB	Conduction Band
CCD	Charge Coupled Device
CLSM	Confocal Laser Scanning Microscopy
DAPI	4',6-Diamidino-2-Phenylindole
DNA	Deoxyribonucleic Acid
DPPC	1- α -dipalmitoylphosphatidylcholine
FIONA	Fluorescence Imaging with One Nanometer Accuracy
FITC	Fluorescein isothiocyanate
FRET	Förster Resonance Energy Transfer
IgG	Immunoglobulin G
LED	Light Emitting Diode
PALM	Photoactivated Localisation Microscopy
PCR	Polymerase Chain Reaction
PBS	Phosphate Buffered Saline
Qdot	Quantum Dots - Invitrogen Trademark name
SNOM	Scanning Near-field Optical Microscopy
SPM	Scanning Probe Microscopy
STED	Stimulated Emission Depletion
STM	Scanning Tunnelling Microscopy
STORM	Stochastic Optical Reconstruction Microscopy
TIR	Total Internal Reflection
TIRFM	Total Internal Reflection Fluorescence Microscopy
TOPO	Tri- <i>n</i> -octylphosphine Oxide
VB	Valence Band

List of Figures

2.1	Jablonski diagram.	13
2.2	Absorption and emission spectra of Alexa Fluor 488.	15
2.3	Fluorescent lifetime and spectral imaging of FRET.	19
2.4	Illustration of electronic band structure in bulk semiconductors . .	20
2.5	Illustration of an exciton, a bound electron and hole pair	22
2.6	Absorption and emission spectra for CdSe nanocrystals of various sizes. Adapted from [16].	26
2.7	Anatomy of quantum dot conjugate.	28
2.8	Size dependent optical properties of quantum dots [2].	29
3.1	Determination of the numerical aperture of a microscope objective lens. Adapted from [12].	36
3.2	Illustration of Synge's proposal.	37
3.3	Illustration showing Newton's TIR experiment.	38
3.4	Electric field incident on an interface between materials of differing refractive indices.	39
3.5	Illustration of an electromagnetic field.	42
3.6	Schematic representation of typical SNOM experimental set-up. .	44
3.7	Operational modes of a fibre optic SNOM probe.	45
3.8	Schematic representation of FRET SNOM and images obtained using a FRET SNOM probe.	49
4.1	Morphology of different cell types found in the human body. Adapted from [1].	56

4.2	General anatomy of an animal cell [2]	57
4.3	Schematic illustration of cellular junctions in epithelial tissues [3].	59
4.4	Schematic illustration demonstrating E-cadherin mediated cell-cell contact	60
4.5	Mechanisms involved in establishing cell-cell contact [7].	62
4.6	Indirect method of immunofluorescent labelling.	68
4.7	Multicoloured fluorescent imaging [33].	69
5.1	Graphic illustration of experimental arrangement used for scanning near-field optical microscopy [1].	76
5.2	Schematic illustration of a standard fluorescence microscope. . . .	78
5.3	Schematic illustration of far-field illumination set-up used to examine fluorescent samples.	80
5.4	Photographs demonstrating far-field illumination method to identify fluorescence from the sample.	81
5.5	Schematic illustration of customised glass slide which facilitates examination of samples with fluorescence microscopy prior to SNOM.	81
5.6	Demonstration of poor quality topography images which are a result of sudden changes in height that are typical of PC-3 cells. . .	83
5.7	Demonstration of image levelling to correct for sample tilt.	85
5.8	Schematic illustration showing general experimental protocol followed for fixing and immunofluorescent labelling of cells.	88
5.9	Schematic illustration showing generalised experimental protocol followed for dual labelling of cells with quantum dots.	89
6.1	Typical SNOM topography images of PNT2 cells.	97
6.2	Fluorescence microscopy image of E-cadherin labelled with Alexa Fluor 488 in PNT2 cells.	99
6.3	Concurrent SNOM topography and optical images of PNT2 cells labelled with Alexa Fluor 488 against E-cadherin.	100
6.4	Measurements of height and diameter of filopodia.	101

6.5	SNOM acquisitions of PNT2 cells labelled with Alexa Fluor 488 and concurrent point spectroscopy.	102
6.6	SNOM acquisitions of quantum dot labelled F-actin in PNT2 cells.	105
6.7	Epifluorescence image of mouse fibroblast cells stained with quantum dots to reveal F-actin filaments. Adapted from [6].	106
6.8	Cross sections of SNOM optical image revealing optical resolution of 60 ± 1 nm.	107
6.9	Comparing the quality of fluorescence signals observed using different fixatives.	109
6.10	Confluent PNT2 cells specifically labelled with red quantum dots to reveal E-cadherin location at sites of cell-cell contact imaged by fluorescence microscopy.	110
6.11	SNOM images of confluent PNT2 cells labelled with quantum dots to reveal E-cadherin localisation.	111
6.12	SNOM topography image of confluent PNT2 cells.	112
6.13	SNOM acquisitions of non-confluent PNT2 cells labelled with quantum dots to reveal E-cadherin localisation.	113
6.14	AFM images revealing quilted appearance of filopodia surface. Adapted from [2].	114
7.1	Fluorescence microscopy images demonstrating E-cadherin and ZO-1 localisation in PNT2 cells.	121
7.2	Graphic illustration of dual labelling in PNT2 cells to localise E-cadherin and ZO-1 simultaneously.	122
7.3	Table summarising the protocols tested during initial optimisation of dual labelling.	124
7.4	Graphic illustration of dual labelling in PNT2 cells to localise E-cadherin and ZO-1 simultaneously.	127
7.5	Table summarising the protocols tested during further optimisation of dual labelling of PNT2 cells.	128

7.6	Comparison of emission spectra of red and green quantum dots with transmission properties of optical filters.	130
7.7	Fluorescence spectra of quantum dots collected with optical band pass filters.	131
7.8	Fluorescence microscopy images showing multiplexed detection of E-cadherin and ZO-1 in PNT2 cells.	132
7.9	Dual labelling to co-localise E-cadherin and ZO-1 in PNT2 cells using SNOM.	133
7.10	Comparison of the morphology of PNT2 and PC-3 cells. Adapted from [18].	135
7.11	Typical SNOM topography acquisitions of non-confluent PC-3 cells.	136
7.12	SNOM topography acquisitions of confluent PC-3 cells.	138
7.13	Dual labelling of ZO-1 and E-cadherin in PC-3 cells as shown by fluorescence microscopy.	141
7.14	SNOM topographic and fluorescence images showing ZO-1 and E-cadherin distribution in PC-3 cells.	142
8.1	Typical SNOM acquisitions comparing the distribution of E-cadherin in the prostate epithelial cell lines PNT2 and PC-3.	150
8.2	SNOM acquisitions of PNT2 cells labelled with Alexa FLuor 488 demonstrating poor photostability.	162

List of Tables

- 1.1 Comparison of optical microscopy techniques, adapted from [2]. 4
- 2.1 Comparison of quantum dots with fluorophores. Adapted from [24]. 30

Chapter 1

Introduction

1.1 Classical microscopy and the diffraction limit

Optical microscopy has been routinely applied to study the interactions and functions of cellular components for centuries. Since its conception, the optical microscope has been instrumental in developing our understanding in the field of cell biology. However as the demand to increase our knowledge and understanding of cellular and molecular biology continues, so does the need to examine samples on increasingly smaller dimensions.

Over the years key innovations to improve on the original design have been introduced to enable samples to be examined in greater detail. One such example is the development of fluorescence microscopy. The technique is a powerful and versatile tool which is used extensively in the life and biological sciences. Factors which have contributed to the technique's widespread use include its ease of use, its availability and its non-invasive nature. When coupled with immunofluorescent labelling, fluorescence microscopy enables specific subcellular components to be identified. Structures ranging from entire organelles to proteins and biomolecules, and even DNA can be localised in live or fixed samples.

However, conventional fluorescence microscopy techniques are limited by the optical diffraction limit. The resolutions achievable are governed by the Rayleigh criterion [1] which suggests that improvements are possible by using a higher energy excitation source and lenses with high numerical apertures. Yet at best, the

optical resolutions attainable are restricted to 200 – 300 nm, which is approximately half the wavelength of the illuminating light. The limitations imposed on fluorescence microscopy by the optical diffraction limit means that vital details which occur on the nanometer-scale are lost.

1.2 Super-resolution microscopy

Over recent years, a series of developments have resulted in the invention of a new class of microscopes in a bid to study samples on the nanoscale. The electron microscope pioneered the use of electrons rather than photons to irradiate a sample. However the technique requires extensive sample preparations and that imaging be carried out in a vacuum environment. Consequently imaging of live samples using electron microscopy is not possible.

A number of approaches have been developed which utilise light to illuminate a sample but achieve superior resolutions to classical microscopy. Confocal laser scanning microscopy (CLSM) employs a tightly focussed laser spot to provide point-like illumination of the sample. A small aperture or pinhole is used to allow only light emanating from the nominal focus plane to pass. Out of focus light from all other planes within the specimen is discarded. The illumination spot is scanned across the sample and the detected light is collected at each point to build up an image of the sample. A 3-dimensional picture of the sample can be constructed using confocal microscopy by imaging through a number of focal planes. The resolutions achieved in the sample depth direction are superior than those achieved with conventional microscopy. Furthermore, confocal microscopy affords slightly enhanced lateral resolution over conventional optical techniques since the pinhole also eliminates light from within the focal plane, that does not originate from the focal point [2].

Total internal reflection fluorescence microscopy (TIRFM) is another notable example of developments in optical microscopy. TIRFM relies upon the properties of evanescent waves which experience exponential decay with increasing distance from their source. Evanescent waves can only penetrate, and therefore cause

excitation, up to a depth of approximately 100 nm within a sample [3, 4]. As with confocal microscopy, the technique gives improved depth resolution compared to conventional microscopy methods. However TIRFM is limited to examine only the surface of samples, the internal structure can not be viewed with this method. Furthermore lateral resolutions are still restricted by the diffraction limit.

One major breakthrough was with subsequent development of scanning probe microscopy (SPM) techniques in the early 1980's, which was pioneered by the invention of the scanning tunnelling microscope [5]. SPM allows examination of samples metrology with nanometre resolution and often enables multiple sample properties to be studied simultaneously. Samples are scanned using a sharp tip which traverses the surface of the sample. The interaction between the tip and the sample allows characteristics such as topography, conductivity and even fluorescence to be studied at the nanoscale.

For the study of biological materials, the SPM techniques of atomic force microscopy (AFM) and scanning near-field optical microscopy (SNOM) are being increasingly utilised. Each of the techniques have the capacity to provide nanometre-scale topography information. Imaging can be performed on a wide variety of sample types and under ambient or even liquid environments. When combined with immunofluorescence labelling of samples, these techniques allow structural and functional information to be correlated. The AFM has to be combined with fluorescence microscopy instrumentation to facilitate this, such as AFM-CLSM [6], and thus the optical information collected is still restricted by the diffraction limit. SNOM however has the capacity to provide both high-resolution optical and topographical information from a wide variety of sample types, and can be adapted to carry out novel imaging approaches [7-9].

Subsequent developments in the field of high-resolution optical microscopy have seen the emergence of further techniques, such as stimulated emission depletion (STED), photo-activated localisation microscopy (PALM), stochastic optical reconstruction microscopy (STORM) and fluorescence imaging with one nanometer accuracy (FIONA). These methods however are still in their infancy and as yet

are not routinely applied microscopy techniques. Table 1.1 provides a summary and comparison of these optical techniques discussed, while a comprehensive review of some of these most recent developments in high-resolution optical imaging is given by Schermelleh *et al.* [2].

Name/Acronym	XY resolution	Z resolution	Comments
Confocal microscopy	180-250 nm	500-700 nm	Resolution diffraction limited
TIRFM	200-300 nm	100 nm	Surface technique
Aperture SNOM [10]	50-100 nm	10 nm	Surface technique
Apertureless SNOM [11]	20 nm		
STED	20-100 nm	560-700 nm	Live cell imaging restricted, complex instrumentation
STORM/PALM/ FIONA [12]	20-50 nm ~1 nm	20-75 nm	Live cell imaging restricted, requires fluorophores with special characteristics

Table 1.1: Comparison of optical microscopy techniques, adapted from [2].

1.3 Scanning near-field optical microscopy in biology

In recent years, SNOM's capacity to examine various biological samples has been demonstrated. For example, Höppener *et al.* [13] demonstrated that SNOM can be used to image fluorescently labelled biological samples under physiological conditions. Topography and SNOM images of a nuclear envelope were acquired and an optical resolution of 55 nm was demonstrated. In another study, Ianoul *et al.* [14] employed SNOM to investigate the distribution of ion channels on the membrane of fixed cardiac myocyte cells. Their study resolved localised ion channel clusters which ranged in size from <60–250 nm. SNOM has also been utilised to compare the effects of fluorescently labelling whole chromosomes by Baylis *et al.* [15]. The extent of chromatin collapse induced by two fluorescence *in situ* hybridisation methods was investigated; one involving fluorescence signal amplification and one without. Through utilising both topography and fluorescence SNOM modes simultaneously, Baylis *et al.* found amplification of fluorescence resulted in more extensive chromatin collapse. And more recently SNOM has

been utilised as a novel molecular recognition sensor. Hofer *et al.* [9] demonstrated that by functionalising a SNOM probe with bio-recognition molecules (biotin), streptavidin molecules on a surface could be identified by monitoring the interactions between the surface and the functionalised probe.

One of the biggest challenges of imaging biological samples with SNOM, and indeed all fluorescence microscopy techniques, is the availability of bright and photostable fluorescent labelling agents. Organic fluorophores that are typically used in fluorescence techniques are prone to rapid photobleaching which can hinder the acquisition of high quality images with good signal-to-noise levels.

1.4 A new class of fluorescent probes

The recent development of semiconductor quantum dots has led to a new class of fluorescent labels for biological applications. Their superior optical properties make them an attractive alternative to organic fluorophores that have been traditionally used in fluorescence microscopy. Quantum dots have a high quantum yield making them significantly brighter and more photostable [16, 17].

Although initially their use was limited due to problems creating water-soluble, functionalised bioconjugates, quantum dots are increasingly being utilised in biological applications. Quantum dots have been successfully employed in *in vivo* studies [18, 19] and in FRET/biosensing applications [20]. Furthermore the use of quantum dots has been demonstrated in immunofluorescent labelling, for the detection of individual biomolecules or proteins [6, 16, 18] and in multiplexing experiments to identify two or more different targets at the same time [21–24].

However, the use of SNOM to investigate biological materials that have been immunolabelled with quantum dots has been realised by few groups. In the publication by Zhong *et al.* [25], the benefits of fluorescent labelling with quantum dots have been combined with SNOM. Their study investigated the location of CD3 antigens on the surface of human T-lymphocytes. The antigens were specifically labelled with quantum dot-streptavidin conjugates which in turn bind to a biotinylated anti-CD3 primary antibody. Through topographic and fluores-

cence SNOM image acquisition, the distribution of CD3 molecules on the surface of T-lymphocytes were examined and their investigation demonstrated a spatial resolution of approximately 90 nm. Their report presented the first near-field images of biological samples labelled with quantum dots. In a further publication by the same research group, Chen *et al.* used SNOM imaging of quantum dot labelled macaque T-lymphocytes [26]. This study focussed on the distribution of two T-cell surface receptors and reported a best optical resolution of less than 50 nm.

In 2009, the study carried out by Zhong *et al.* has been extended to investigate the co-localisation of CD3 and CD4 or CD3 and CD8 surface antigens on T-lymphocytes simultaneously. Dual colour detection was carried out to assess the distribution and organisation of these antigens [27]. Their study, published as our studies in multiplexing were underway, demonstrated for the first time SNOM imaging combined with quantum dot based multiplexing.

1.5 Thesis outline

The work presented in this thesis will draw on the advantages afforded by quantum dot labelling when combined with SNOM imaging. The application of a quantum dot based/SNOM approach has been used to investigate cell-cell adhesion mechanisms in prostate epithelial cells. This has been achieved through immunofluorescent labelling of the cell-cell adhesion protein E-cadherin, and analysing its distribution at various stages of epithelial sheet formation using SNOM topography and fluorescence acquisitions.

The expression and correct functioning of E-cadherin has been linked to increased invasiveness and tumour grade [28–30]. Thus the lack of E-cadherin has important implications in the progression of cancer. Significant progress is underway towards understanding the relationship between cellular adhesion and the metastatic capacity of tumours, however many questions remain unanswered.

A standardised and rigorous sample preparation methodology has been developed to lead this investigation. Moreover, a dual labelling protocol has been

optimised to facilitate a comparative study of the adhesion mechanisms, and the effect of aberrant adhesion protein expression, in both healthy and cancerous epithelial cells.

The multidisciplinary nature of the research requires that this thesis attempts to explain the fundamental principles behind semiconductor quantum dots and the techniques employed, whilst also providing biological insight into the mechanisms of cell-cell interactions.

Chapter 2 introduces the principles of fluorescence and describes the photo-physics behind the phenomena. The physics of semiconductors and the energy states of an exciton in bulk material is briefly described. The effects of quantum confinement on the energy states is derived for an exciton which is confined in 3-dimensions. These principles are provided such that the reader may form a basic understanding of the concepts that are relevant to this work, and form the basis of later discussions. This chapter continues by describing the manufacture of quantum dots with particular emphasis on suitable adaptations for their use in biological applications. A comparison of the optical properties of conventional fluorophores and semiconductor quantum dots is provided, and the use of quantum dots in biological and medical sciences is reviewed.

The development of the scanning near-field optical microscope (SNOM) is discussed in Chapter 3. The effect of the diffraction limit on conventional optical techniques and the concept of circumventing this limit through exploiting the properties of evanescent waves is described. The theory of SNOM is treated and its applications and typical set-up are reviewed. This chapter also considers the design of the SNOM probe and various modes of operation. Finally, the scanning technique and the importance of the feedback mechanisms used in this work are discussed.

Chapter 4 briefly describes the relevant aspects of cell biology which are necessary to form an understanding of the work carried out in this thesis. Adhesion

mechanisms in epithelial tissues are the principle focus of this research, thus the proteins involved in cell-cell adhesion and their interactions with the actin cytoskeleton are discussed. Aberrant adhesion has important implications in disease and has been shown to result in increased invasiveness in cancer. The current understanding of the mechanisms involved in cancer progression is addressed. Particular emphasis is placed on the impact of cell-cell adhesion on the progression of prostate cancer, and the current understanding of the role that E-cadherin plays is described.

Imaging procedures and the developments in experimental design required to lead this work are discussed in Chapter 5. Complete methodologies used for the preparation of samples are provided and summarised with the aid of a flow chart for the benefit of other researchers.

Chapter 6 explores adhesion mechanisms in healthy prostate epithelial cells using SNOM. These are identified through immunofluorescent labelling of E-cadherin and correlated with the structural information provided by the simultaneously acquired topography images. Comparisons are made between various stages of epithelial sheet formation and with observations by other researchers.

To continue this study, and extend it to examine E-cadherin expression and localisation in other cell lines, Chapter 7 details the development of a multiplexed approach to sample preparation. A dual labelling methodology was devised to facilitate the study of E-cadherin in cancerous cells, where E-cadherin expression has been reported to be down-regulated. Important aspects of sample preparation are addressed in this chapter.

Finally, Chapter 8 concludes this thesis and evaluates the findings of Chapters 6 and 7. The successes of this work and future developments to continue such studies will be considered.

Bibliography

- [1] Lord Rayleigh. Investigations in optics with special reference to the spectroscope. *Philosophical Magazine*, 8:261–274, 1879.
- [2] L. Schermelleh, R. Heintzmann, and H. Leonhardt. A guide to super-resolution fluorescence microscopy. *The Journal of Cell Biology*, 190(2):165–175, 2010.
- [3] D. Axelrod. Cell-substrate contacts illuminated by total internal reflection fluorescence. *Journal Of Cell Biology*, 89(1):141–145, 1981.
- [4] D. Axelrod. *Total Internal Reflection Fluorescence Microscopy*, volume 89 of *METHODS IN CELL BIOLOGY*. Elsevier Academic Press Inc, 2008.
- [5] G. Binnig and H. Rohrer. Scanning tunneling microscopy. *Helvetica Physica Acta*, 55(6):726–735, 1982.
- [6] S. H. Doak, D. Rogers, B. Jones, L. Francis, R. S. Conlan, and C. Wright. High-resolution imaging using a novel atomic force microscope and confocal laser scanning microscope hybrid instrument: essential sample preparation aspects. *Histochem. Cell. Biol.*, 130(5):909–916, 2008.
- [7] V. Deckert, D. Zeisel, R. Zenobi, and T. Vo-Dinh. Near-field surface enhanced raman imaging of dye-labeled dna with 100-nm resolution. *Analytical Chemistry*, 70(13):2646–2650, 1998.
- [8] S. A. Vickery and R. C. Dunn. Scanning near-field fluorescence resonance energy transfer microscopy. *Biophysical Journal*, 76(4):1812–1818, 1999.
- [9] M. Hofer, S. Adamsmaier, T. S. van Zanten, L. A. Chtcheglova, C. Manzo, M. Duman, B. Mayer, A. Ebner, M. Moertelmaier, G. Kada, M. F. García-Parajó, P. Hinterdorfer, and F. Kienberger. Molecular recognition imaging using tuning fork-based transverse dynamic force microscopy. *Ultramicroscopy*, 110(6):605–611, 2010.
- [10] R. C. Dunn. Near-field scanning optical microscopy. *Chemical Reviews*, 99(10):2891–2927, 1999.
- [11] E. J. Sanchez, L. Novotny, and X. S. Xie. Near-field fluorescence microscopy based on two-photon excitation with metal tips. *Physical Review Letters*, 82(20):4014–4017, 1999.

- [12] A. Yildiz, J. N. Forkey, S. A. McKinney, T. Ha, Y. E. Goldman, and P. R. Selvin. Myosin v walks hand-over-hand: Single fluorophore imaging with 1.5-nm localisation. *Science*, 300(5628):2061, 2003.
- [13] C. Höppener, J. P. Siebrasse, R. Peters, U. Kubitscheck, and A. Naber. High-resolution near-field optical imaging of single nuclear pore complexes under physiological conditions. *Biophysical Journal*, 88(5):3681–3688, 2005.
- [14] A. Ianoul, M. Street, D. Grant, J. Pezacki, R. S. Taylor, and L. J. Johnston. Near-field scanning fluorescence microscopy study of ion channel clusters in cardiac myocyte membranes. *Biophysical Journal*, 87(5):3525–3535, 2004.
- [15] R. M. Baylis, S. H. Doak, M. D. Holton, and P. R. Dunstan. Fluorescence imaging and investigations of directly labelled chromosomes using scanning near-field optical microscopy. *Ultramicroscopy*, 107(4-5):308–312, 2006.
- [16] X. Wu, H. Liu, Q. Liu, K. N. Hayley, J. A. Treadway, J. P. Larson, N. Ge, F. Peale, and M. P. Bruchez. Immunofluorescent labelling of cancer marking her2 and other cellular targets with semiconductor quantum dots. *Nature Biotechnology*, 21(1):41–46, 2003.
- [17] W. C. W. Chan and S. M. Nie. Quantum dot bioconjugates for ultrasensitive nonisotopic detection. *Science*, 281(5385):2016–2018, 1998.
- [18] B. Dubertret, P. Skourides, D. J. Norris, V. Noireaux, A. H. Brivanlou, and A. Libchaber. In vivo imaging of quantum dots encapsulated in phospholipid micelles. *Science*, 298(5599):1759–1762, 2002.
- [19] J. K. Jaiswal, H. Mattoussi, J. M. Mauro, and S. M. Simon. Long-term multiple color imaging of live cells using quantum dot bioconjugates. *Nature Biotechnology*, 21(1):47–51, 2003.
- [20] I. L. Medintz, A. R. Clapp, H. Mattoussi, E. R. Goldman, B. Fisher, and J. M. Mauro. Self-assembled nanoscale biosensors based on quantum dot fret donors. *Nature Materials*, 2(9):630–638, 2003.
- [21] E. Sweeney, T. H. Ward, N. Gray, C. Womack, G. Jayson, A. Hughes, C. Dive, and R. Byers. Quantitative multiplexed quantum dot immunohistochemistry. *Biochemical and Biophysical Research Communications*, 374(2):181–186, 2008.
- [22] B. B. Zhang, X. H. Liu, D. N. Li, H. Tian, G. P. Ma, and J. Chang. Preparation of multi-color quantum dots and its application to immunohistochemical analysis. *Chinese Science Bulletin*, 53(13):2207–2083, 2008.
- [23] D. H. Huang, X. H. Peng, L. Su, D. S. Wang, F. R. Khuri, D. M. Shin, and Z. Chen. Comparison and optimization of multiplexed quantum dot-based immunohistofluorescence. *Nano Research*, 3(1):61–68, 2010.

-
- [24] J. Liu, S. K. Lau, V. A. Varma, R. A. Moffitt, M. Caldwell, T. Liu, A. N. Young, J. A. Petros, A. O. Osunkoya, T. Krogstad, B. Leyland-Jones, M. D. Wang, and S. M. Nie. Molecular mapping of tumor heterogeneity on clinical tissue specimens with multiplexed quantum dots. *ACS Nano*, 4(5):2755–2765, 2010.
- [25] L. Y. Zhong, W. T. Liao, X. P. Wang, and J. Y. Cai. Detection the specific marker of cd3 molecules of human peripheral blood t-lymphocytes using snom and quantum dots. *Colloids and Surfaces A - Physicochemical and Engineering Aspects*, 313(Sp. Iss.):642–646, 2008.
- [26] Y. Chen, L. Shao, Z. Ali, J. Cai, and Z. W. Chen. Nsom/qd-based nanoscale immunofluorescence imaging of antigen-specific t-cell receptor responses during an in vivo clonal v gamma 2v delta 2 t-cell expansion. *Blood*, 111(8):4220–4232, 2008.
- [27] L. Y. Zhong, G. C. Zeng, X. X. Lu, R. C. Wang, G. M. Gong, L. Yan, D. Huang, and Z. W. Chen. Nsom/qd-based direct visualization of cd3-induced and cd28-enhanced nanospatial coclustering of tcr and coreceptor in nanodomains in t-cell activation. *PLoS ONE*, 4(6):c5945, 2009.
- [28] R. Umbas, J. A. Schalken, T. W. Aalders, B. S. Carter, H. F. M. Karthaus, H. E. Schaafsma, F. M. J. Debruyne, and W. B. Isaacs. Expression of the cellular adhesion molecule e-cadherin is reduced or absent in high-grade prostate cancer. *Cancer Research*, 52(18):5104–5109, 1992.
- [29] L. J. McWilliam, W. F. Knox, C. Hill, and N. J. R. George. E-cadherin expression fails to predict progression and survival in prostate cancer. *The Journal of Urology*, 155(Supplement 5):516A, 1996.
- [30] G. Davies, W. G. Jiang, and M. D. Mason. Cell-cell adhesion molecules and signaling intermediates and their role in the invasive potential of prostate cancer cells. *Journal of Urology*, 163(3):985–992, 2000.

Chapter 2

Fluorescence

2.1 Introduction

Fluorescence techniques are valuable tools applied widely across the biological and life sciences. In cellular and molecular biology, fluorescence techniques are used to study the interactions of bio-molecules and to characterise the function of cellular components.

Understanding the principles of fluorescence becomes important when developing fluorescence protocols or when faced with imaging problems. This chapter attempts to outline these principles and the important optical properties that are intrinsic to the fluorophores commonly used in fluorescent techniques.

Semiconductor quantum dots are a new class of fluorescent labels with superior optical properties to conventional fluorophores. Semiconductor physics and the effects of quantum confinement are introduced in this chapter in order to provide a basic understanding of the properties of quantum dots. Their use in a variety of biomedical applications and their optical properties is reviewed and compared with conventional organic fluorophores.

2.2 Principles of fluorescence

2.2.1 Photoluminescence

Photoluminescence is the process where a substance absorbs and subsequently re-emits photons and is (typically) due to electron transitions within the substance. Fluorescence is a specific type of photoluminescence which occurs when the electrons are optically excited and undergo internal energy transitions before being re-emitted. The mechanisms involved in photoluminescence are graphically illustrated in Figure 2.1.

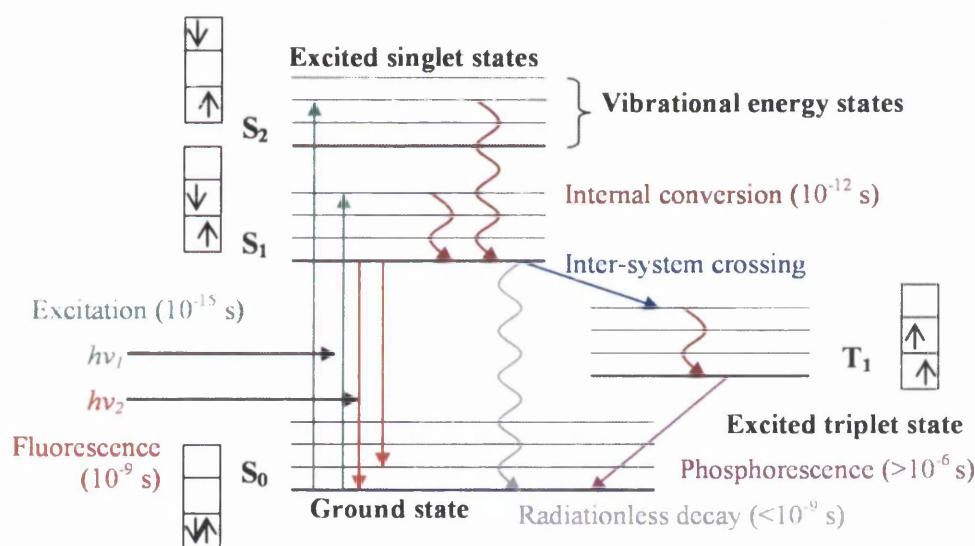


Figure 2.1: Jablonski diagram showing available energy states within a molecule and the possible electronic transitions between states. Adapted from [1].

When a ground state electron in a fluorescent molecule is irradiated with light, all the energy of an incident photon, $h\nu_1$, is absorbed. If the energy of the incident photon is sufficient, the electrons in the ground state, S_0 , are excited to a higher energy orbital, S_1 . The electrons can be excited to a number of vibrational and rotational states within S_1 , or even excited to a higher energy orbital S_2 , depending on the energy of the absorbed photon. However, the electron will rapidly relax to the lowest vibrational state within S_1 via a non-radiative process called internal conversion; this excess energy is dissipated through molecular vibrations.

If the electron in the excited orbital is spin paired with the electron in the

ground state, transition of the excited electron back to the ground state, S_0 , is allowed. As the electron relaxes back to the ground state, a photon is emitted. This process is called fluorescence. The emitted photon is of lower energy, $h\nu_2$, (longer wavelength) than that of the photon which was absorbed, due to the non-radiative relaxation of the excited electron to the lowest vibrational state in S_1 (internal energy transitions). The process of fluorescence occurs rapidly and fluorescence lifetimes (average time between photon absorption and emission) of the order 10 ns are typical for common fluorophores.

There is also the possibility that the excited electron may be converted to a parallel spin state (triplet state, represented by T_1), by the process of inter-system crossing. Although such transitions are 'forbidden' in quantum theory, electrons do experience inter-system crossing and in order to return to the singlet ground state S_0 , the electron must again undergo a forbidden transition. Such a transition is called phosphorescence and is characterised by much longer lifetimes than fluorescence, owing to the unfavourable nature of the process.

2.2.2 Fluorescence spectra

A range of energies can be used to excite a fluorescent molecule and these can be represented by an absorption spectrum. The absorption and emission spectra of the commonly used fluorophore, Alexa Fluor 488, is shown in Figure 2.2. The minimum amount of energy required to cause excitation within a fluorophore is equal to the difference in energies of the ground state, S_0 , and the first excited orbital, S_1 . This is characterised by a steep cut off at higher wavelength (lower energy) scales. The various vibrational and rotational states that an excited electron may occupy, are represented by the peaks and troughs present in the absorption spectra. However these generally become smoothed out when the fluorophore is in solution. The absorption maximum reflects the wavelength which is most effective for causing excitation. It is the wavelength that results in the highest proportion of excited fluorophores.

Similarly, the fluorophore can emit a range of wavelengths as it returns to any number of the available states in S_0 . However as mentioned earlier, the emitted

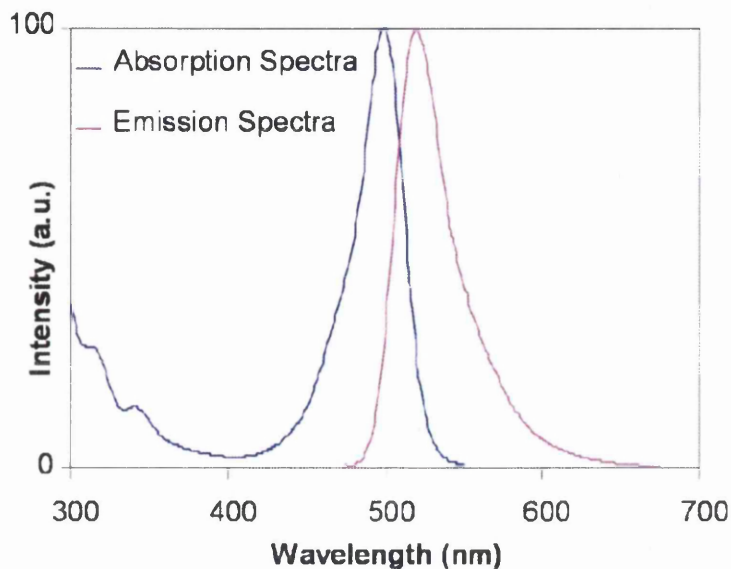


Figure 2.2: *Absorption and emission spectra of Alexa Fluor 488 [2].*

photon will in general be of lower energy than that which was absorbed, resulting in a shift in the maximum. This shift is known as the Stokes shift. For practical purposes, a large Stokes shift is desirable as this enables more precise separation of fluorescent signals from the illumination source.

2.2.3 Photobleaching

Fluorophores can undergo many excitation/ emission events; they can repeatedly cycle between ground state, excitation and fluorescence emission. However, fluorophores can permanently lose the ability to fluoresce if structural damage occurs. This is known as photobleaching and can arise as a result of exposure to high intensity light or prolonged periods of excitation. Lichtman and Conchello discuss the process of bleaching and its implications in fluorescence imaging [1]. Although the photophysics of bleaching is not well understood, it is thought to be associated with triplet state formation. The triplet state is a relatively long lived state, during which time the fluorophore has an opportunity to interact with other molecules which may cause irreversible chemical damage.

Even though the Alexa Fluor series of fluorophores are more robust than other

organic dyes such as fluorescein, photobleaching remains one of the greatest challenges in fluorescence imaging and there are limited ways in which to reduce the rate at which it occurs. One of the most promising developments in combatting the limitations imposed by photobleaching is the utilisation of quantum dots in fluorescence microscopy [3]. The advantageous optical properties afforded by quantum dots are discussed in more detail later in this chapter, (see section 2.5.4).

2.2.4 Quantum yield

The quantum yield of a fluorophore is the proportion of excitation events that result in photon emission. It is a measure of the emission efficiency of a fluorophore. The quantum yield, ϕ , is defined as:

$$\phi = \frac{\text{number of photons emitted}}{\text{number of photons absorbed}} \quad (2.1)$$

Quantum yields vary widely from approximately 0.05 to nearly 1 depending on the fluorophore; however this value can be affected greatly by local environmental factors. In general, fluorophores with a high quantum yield have high fluorescence intensity. Additionally, a high quantum yield means the occurrence of intersystem crossing is reduced. As such, the likelihood of associated chemical changes, e.g. bleaching, is lessened.

2.2.5 Fluorescent lifetime

The fluorescence lifetime of a fluorophore is the average time an electron will remain in the excited state before decaying back to the ground state by photon emission. The level of fluorescence is directly related to the proportion of molecules residing in the excited singlet state, or put another way, the fluorescence intensity is proportional to the number of photons emitted. Therefore the fluorescence lifetime can be measured experimentally by monitoring the intensity in the period immediately following excitation. Doing so reveals that the time taken to return to the ground state follows an exponential behaviour, and the

intensity, I , can be written as a function of time, t ,

$$I(t) = I_0 e^{-t/\tau} \quad (2.2)$$

where I_0 is the intensity at $t = 0$ and τ is the fluorescence lifetime. Thus the lifetime can be measured by calculating the time taken for the intensity to reduce by a factor e .

Non-radiative pathways, such as quenching and Förster resonance energy transfer (FRET), compete with fluorescence as a mechanism for the fluorophore to return to the ground state. Thus the decay time for non-radiation relaxation processes, $1/\kappa_{nr}$, is taken into account in the fluorescence lifetime,

$$\tau = \frac{1}{\kappa_f + \kappa_{nr}} \quad (2.3)$$

where κ_f is the decay rate for radiative relaxation.

2.2.6 Quenching

Fluorescence quenching is a process of non-radiative relaxation. It competes with fluorescence as a mechanism for excited state decay and can therefore result in a dramatically decreased fluorescence intensity and cause a reduction in the fluorescent lifetime. Fluorescence quenching is different to bleaching in that it is a reversible process and can be exploited as a means to detect the presence of the quencher molecule. However for most applications, quenching is an undesirable process since it can inhibit the detection of fluorescence.

Collisional quenching of an excited fluorophore in solution occurs following a diffusive encounter with another molecule. The fluorophore returns to the ground state without emitting a photon. Alternatively, quenching may occur when a non-fluorescent complex is formed between a ground state fluorophore and a quencher molecule. In either case the quencher molecule may be of the same or different species as the fluorophore and may itself be fluorescent or non-fluorescent. The mechanisms involved in quenching are comprehensively described by Lakowicz [4].

2.2.7 Förster resonance energy transfer (FRET)

As mentioned previously, there are alternative pathways available for an excited fluorophore to return to its ground state. FRET is the non-radiative transfer of energy from an excited donor fluorophore to an acceptor molecule, which may or may not be fluorescent. The process is not due to photon emission by the donor and absorption by the acceptor; it is the result of a dipole-dipole interaction between the donor-acceptor pair. The donor fluorophore can be considered as an oscillating dipole that can couple to the acceptor with similar resonant frequency. This results in energy transfer to the acceptor molecule.

The degree of FRET depends on the physical separation between the donor-acceptor pair, r , the relative orientation of the dipoles and the spectral overlap between the donor emission and the acceptor absorption as described by R_0 , the Förster radius. The rate of energy transfer, κ , between an acceptor-donor pair is related to the lifetime of the donor in the absence of an acceptor molecule, τ , and is expressed as:

$$\kappa = \tau^{-1} \times \left(\frac{R_0}{r} \right)^6 \quad (2.4)$$

The efficiency of the transfer process at a distance, r , between the pair is given by:

$$E = \frac{R_0^6}{R_0^6 + r^6} \quad (2.5)$$

From equation (2.5), one can see that the Förster radius, R_0 , is equal to the distance between the pair at which the energy transfer process is 50 % efficient. That is, when $r = R_0$, the donor intensity is half the intensity measured when no acceptor molecule is present and the transfer rate is equal to the decay rate of the donor in the absence of the acceptor. R_0 typically ranges from 2 – 10 nm.

Practically, FRET manifests itself in numerous ways. FRET causes changes to the fluorescence lifetime of donor molecules, an increase in acceptor fluorescence intensity (coupled with decrease in donor fluorescence intensity) and/or can change the polarisation of the emitted light. Detection of FRET may be carried out by monitoring one of these physical variables. For example, the lifetime of the donor molecules will become shortened in the event that FRET occurs be-

tween the donor and acceptor molecules. This is demonstrated by Figure 2.3(a), where mCerulean are the donor molecules and mVenus are the acceptor molecules. FRET may also be observed spectrally through a reduction in the fluorescence intensity of the donor molecule in the presence of the acceptor molecules. As demonstrated in Figure 2.3(b), the donor fluorescence can be re-instated upon photobleaching of the acceptor molecule.

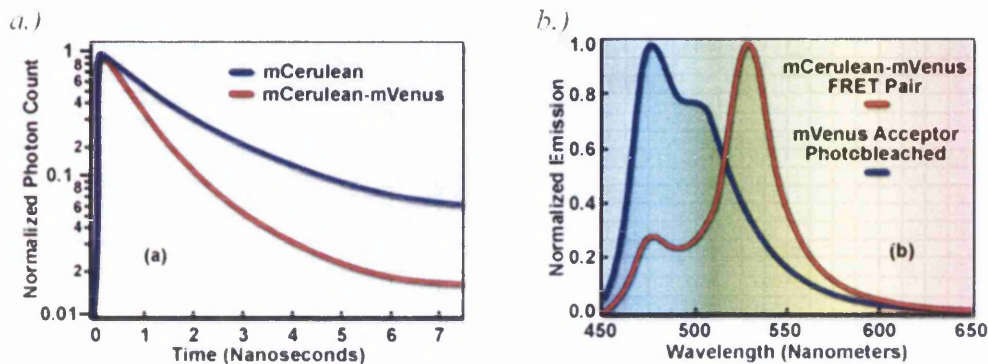


Figure 2.3: (a) Shortening of fluorescent lifetime of FRET donor molecules (mCerulean) in the presence of acceptor molecules (mVenus). (b) Decrease in intensity of fluorescence emission from donor molecules in the presence of acceptor (red spectra) which is reinstated upon acceptor bleaching (blue spectra) [5].

The high dependency of FRET on the separation between the donor-acceptor pair makes FRET a valuable tool in a variety of fluorescence applications; from biosensing [6], as a spectroscopic ruler [7] and as a novel method of achieving higher resolutions in scanning probe techniques [8].

2.3 Semiconductor quantum dots

2.3.1 Introduction

Quantum dots are semiconductor nanocrystals that are typically a few nanometers in diameter. Their conduction characteristics and their physical chemistry are defined not only by the material they are composed of, but also by their physical dimensions. Quantum dots exhibit atomic-like behaviour in that they have discrete energy states rather than continuous bands, resulting in unique optical

properties. Such properties arise as a result of quantum confinement effects and can be fine-tuned by simply changing the size of the nanocrystal.

In 1993, Murray et al. [9] reported a procedure for synthesising high optical quality, low size distribution CdSe quantum dots dispersed in organic solvents. However it was not until 1998 when methods for producing water soluble quantum dots were reported [3, 10], did quantum dots emerge as a promising alternative to traditional organic fluorophores.

In order to fully understand the properties of quantum dots and their potential for use in bio-medical applications, some background information on semiconductor physics and the quantum mechanical description of quantum confinement shall be introduced.

2.3.2 Bulk semiconductors

Semiconductors are materials with conduction properties between that of conductors and insulators. In a semiconductor the energy states for electrons form a series of allowed energy bands separated by band gaps. Within the band there is a continuum of energy levels available. This is illustrated in Figure 2.4. The valence

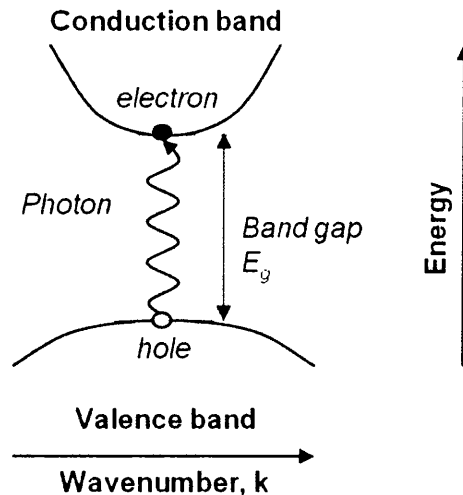


Figure 2.4: Simple illustration of electronic band structure in bulk semiconductors, comprising the valence and conduction bands which are separated by forbidden energy states which form the band gap.

band (VB) is the name given to the uppermost occupied energy states and the conduction band (CB) is the name given to the lowest available unoccupied energy states. These bands are separated by a forbidden energy gap which is called the semiconductor band gap, E_g . The size of E_g varies according to composition and for cadmium selenide (CdSe) bulk semiconductors, $E_g \approx 1.7 \text{ eV}$ [9, 11].

When an incident photon with sufficient energy is absorbed, an electron will be excited to the CB and an empty state (or hole) is left behind in the VB. This hole behaves like a positive charge. The pair will recombine if the electron returns to the VB and, if conditions support radiative recombination, a photon will be emitted to carry away the excess energy. When such an electron-hole pair is formed upon photon absorption, the CB electron is attracted to the positive hole in the VB via a Coulomb potential, described by equation (2.6).

$$V(r) = -\frac{e^2}{4\pi\epsilon_0\epsilon_r|\mathbf{r}_e - \mathbf{r}_h|} \quad (2.6)$$

where e denotes the electron charge, ϵ_0 the permittivity of free space, ϵ_r the dielectric constant of the material and \mathbf{r}_e and \mathbf{r}_h the position of the electron and hole respectively. This can result in the formation of an exciton: a hydrogen-like bound state between an electron and hole. The exciton is free to move through the crystal lattice, transporting energy as it does so. An exciton has lower energy than the unbound electron-hole pair due to its intrinsic binding energy. Thus the exciton exists below the CB and the photon energy required to produce an exciton can be less than E_g .

The interaction of the bound electron-hole pair can be described by the Hamiltonian,

$$H = -\frac{\hbar^2}{2m_e^*}\nabla_e^2 - \frac{\hbar^2}{2m_h^*}\nabla_h^2 - \frac{e^2}{4\pi\epsilon_0\epsilon_r|\mathbf{r}_e - \mathbf{r}_h|} \quad (2.7)$$

where the effective mass of the electron is described by m_e^* and the effective mass of the hole, m_h^* and $\nabla_{e,h}^2$ the differential operators with respect to the electron and hole positions. The relative position, \mathbf{r} , of the electron and hole is given by equation (2.8) and the position of the centre of mass, \mathbf{R} , by (2.9).

$$\mathbf{r} = \mathbf{r}_e - \mathbf{r}_h \quad (2.8) \quad \mathbf{R} = \frac{m_e^* \mathbf{r}_e + m_h^* \mathbf{r}_h}{m_e^* + m_h^*} \quad (2.9)$$

The full mass, M and the reduced mass, μ of the system can be introduced,

$$M = m_e^* + m_h^* \quad (2.10) \quad \mu = \frac{m_e^* m_h^*}{m_e^* + m_h^*} \quad (2.11)$$

Thus, the Hamiltonian (2.7) can then be expressed as follows,

$$H = -\frac{\hbar^2}{2M} \nabla_R^2 - \frac{\hbar^2}{2\mu} \nabla_r^2 - \frac{e^2}{4\pi\epsilon_0\epsilon_r r} \quad (2.12)$$

The first term in equation (2.12) corresponds to the Hamiltonian of a free particle of mass M , the remaining terms describe the Hamiltonian of a particle of mass μ in a Coulomb potential.

In analogy, to the Bohr radius of the Hydrogen atom, the physical separation of the bound electron and hole is known as the exciton Bohr radius, a_B , as illustrated in Figure 2.5 and is defined as follows,

$$a_B = \frac{4\pi\epsilon_0\epsilon_r \hbar^2}{\mu e^2} \quad (2.13)$$

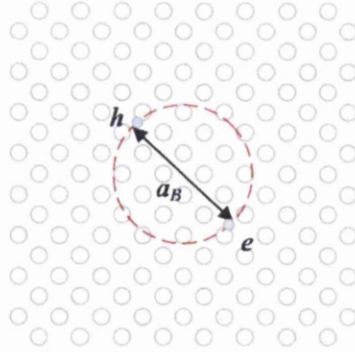


Figure 2.5: An exciton, a bound state between an electron, e and hole, h , separated by an exciton Bohr radius, a_B .

Additionally, we can define the exciton Rydberg energy:

$$R_y^* = \frac{e^2}{8\pi\epsilon_0\epsilon_r a_B} \quad (2.14)$$

Thus, the energy states of an exciton are derived from the solution to the Hamil-

tonian and are described by the following dispersion relation,

$$E_n(\mathbf{k}) = E_g - \frac{R_y^*}{n^2} + \frac{\hbar^2 \mathbf{k}^2}{2M} \quad (2.15)$$

with \mathbf{k} the exciton wavevector as given by, $\mathbf{k} = \mathbf{k}_e + \mathbf{k}_h$. The exciton behaves as a single, uncharged particle of mass M . Equation (2.15) takes into account the kinetic energy associated with motion of the exciton's centre of mass.

2.4 Effects of quantum Confinement

It is possible to manufacture semiconductor structures with 1, 2 or all 3-dimensions comparable to the size of the exciton bohr radius. When the physical dimensions of the structure in a particular direction are smaller than the exciton bohr radius, the motion of the exciton becomes confined in this direction. A quantum well is a structure which permits motion of the exciton in two directions but with restricted motion in the other direction. When the motion of an exciton is confined in two directions, the structure is called a quantum wire. While in a quantum dot, the exciton becomes restricted in all 3-dimensions. When the exciton is confined, the allowed energy levels are no longer continuous as in bulk semiconductors, but become discrete. Quantum confinement results in the unique optical properties we find quantum dots to exhibit.

In order to derive the allowed states for a quantum dot, a simplified model must be used that describes a particle confined in a spherical box. The result can be then be modified for two limiting cases: weak and strong confinement as discussed by Efros and Efros [12].

2.4.1 Quantum dots

By considering the Hamiltonian of a particle in a spherically symmetric potential of width a , the following energy levels can be derived:

$$E_{nl} = \frac{\hbar^2 \chi_{nl}^2}{2ma^2} \quad (2.16)$$

where m is the mass of the particle and χ_{nl} are the roots of the spherical Bessel functions with n the number of the root and l the order of the function.

When considering an exciton confined in a spherical quantum dot, the energy states for a particle in a spherically symmetric potential must be incorporated into the dispersion relation for a free exciton.

Weak confinement

In the case when the radius of the quantum dot is small, but still larger than the exciton Bohr radius, weak confinement exists and the dispersion relation (Equation (2.15)), is re-written to include the solution for a particle confined in a spherical potential, with width governed by the radius of the quantum dot, R ,

$$E_{nml} = E_g - \frac{R_y^*}{n^2} + \frac{\hbar^2 \chi_{ml}^2}{2MR^2} \quad (2.17)$$

In this case, motion of the excitons centre of mass is quantised and the exciton is characterised by the quantum numbers n , m , and l . n describes the internal states due to the Coulomb interaction ($1S$, $2S$, $2P$; $3S$, $3P$, $3D\dots$), while m and l are connected to the states which arise due to the motion of the centre of mass in the presence of an external potential barrier ($1s$, $1p$, $1d\dots$, $2s$, $2p$, $2d\dots$). The energy of the lowest state ($n = 1$, $m = 1$, $l = 0$) is therefore,

$$E_{1S1s} = E_g - R_y^* + \frac{\pi^2 \hbar^2}{2MR^2} \quad (2.18)$$

where $\chi_{10} = \pi$ was used. Equation (2.18) can be re-written using equations (2.13) and (2.14) to give,

$$E_{1S1s} = E_g - R_y^* \left(1 - \frac{\mu}{M} \left(\frac{\pi a_B}{R} \right)^2 \right) \quad (2.19)$$

Strong confinement

When the radius, R , of a quantum dot is such that the electron-hole pair are confined in a space smaller than the exciton bohr radius, a_B , the Coulomb interaction experienced by the pair is significant. Brus [13] found the energy of

the ground state electron-hole pair (1s1s) is given by,

$$E_{1s1s} \approx E_g + \frac{\pi^2 \hbar^2}{2\mu R^2} - 1.8 \frac{e^2}{\epsilon R} \quad (2.20)$$

The term $e^2/\epsilon R$ describes effective Coulomb interaction between the electron-hole pair which, upon comparison with the exciton Rydberg energy, equation (2.14) and taking into account $R \ll a_B$, one can see that the contribution to the energy from this term is more significant than for a bulk crystal, as discussed by Gaponenko [14].

Confinement effects in real quantum dots

Ekimov *et al.* [15] examined CdSe nanoparticles with average radii 25, 8, 3.8, 2.6 and 2.1 nm. They observed that the absorption spectrum for the weakly confined 25 nm particles is the same as for bulk CdSe with three absorption edges visible. Since $a_B \simeq 5.6$ nm for CdSe, this result is as one would expect. The absorption spectra for the 8 nm particles started to exhibit the effects of quantum confinement and only two absorption edges were present in their spectra. The confinement effects were clearly visible on the absorption spectra for the smaller CdSe nanoparticles, with discrete peaks appearing near the absorption edge corresponding to the most prominent exciton transitions.

Figure 2.6 illustrates the absorption (dashed lines) and emission (solid lines) spectra of strongly confined CdSe quantum dots with diameters 3.5, 4.5, 6.0 and 7.0 nm, as observed by Javier *et al.* [16]. The spectra demonstrate the size dependent nature of the optical properties of the quantum dots, with a blue shift in the absorption edge as the diameter of the quantum dot decreases. The two most prominent transitions are indicated on the absorption spectra for the 3.5 nm diameter quantum dot. Additionally, and as noted by Ekimov *et al.* [15], the Stokes shift is larger for smaller sized quantum dots.

The commercially available quantum dots used in this study display peak emission at the wavelengths 525, 605 and 655 nm, further information relating to their size and composition is included in Appendix 8.4 [2]. The effects of strong

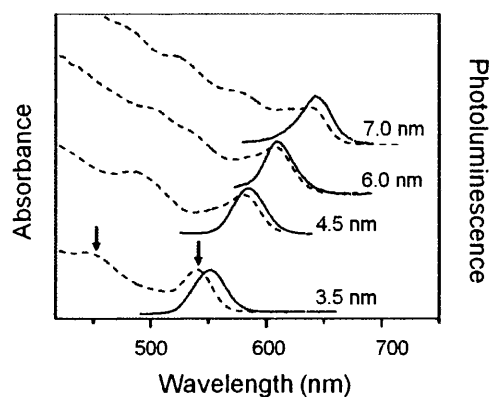


Figure 2.6: Absorption (dashed lines) and emission (solid lines) spectra for a series CdSe nanocrystals of diameters shown. The most prominent transitions are indicated for the 3.5 nm quantum dots. Adapted from [16].

confinement can be seen in their optical properties.

2.5 Synthesis and properties of quantum dots

2.5.1 Solvent synthesis

Although alternative methods have been reported for the synthesis of semiconductor nanocrystals, Murray et al [9] were the first to report a reliable technique for producing high optical quality quantum dots with a low size distribution (<5 % rms in diameter). The methodology employed by Murray involves injection of organometallic reagents into a hot coordinating solvent. The growth of the nanocrystals is monitored by observing the absorption spectra of aliquots of the reaction solution and is controlled by adjusting the temperature and pressure conditions. When the desired optical characteristics are observed in the reaction solution, small quantities can be removed. This permits a range of sizes to be manufactured from a single reaction solution. The size distribution of these nanocrystals can be further reduced with a centrifuge and the remaining quantum dots can be dispersed in a number of solvents.

2.5.2 Core/shell quantum dots

The high surface-volume ratio of quantum dots means that the surface properties have important effects on other properties such as optical, structural and solubility. The procedure utilised by Murray [9], employs a Tri-*n*-octylphosphate oxide (TOPO) monolayer on the surface of the nanocrystals which prevents their aggregation when in solvent. However, TOPO coated quantum dots are prone to photooxidation and are therefore unstable and degrade with time.

Alternatively, nanocrystals can be capped with an inorganic shell consisting of a thin layer of semiconductor of higher band gap which effectively helps to confine the exciton. This process requires a close match in lattice constants of the core-shell materials to passivate the interface. The shell reduces the number of trap states at the surface of the core which lead to non-radiative recombination of the exciton. This promotes band edge emission and results in improved quantum yield. Experimental details for the synthesis of ZnS capped CdSe nanocrystals is reported by Hines [17] and Dabbousi [18].

2.5.3 Surface functionalisation for bio-medical applications

When the synthesis of quantum dots is carried out, they are typically dispersed in a solvent such as toluene or chloroform and they are coated with a surfactant layer which renders them hydrophobic. For most biological applications however, quantum dots need to be soluble in aqueous solutions. There are many methods that have been reported to make quantum dots water soluble. Replacing the surfactant layer with molecules that have functional groups reactive towards the surface, such as mercapto functionalities (-SH) and hydrophilic tails, such as carboxyl functionalities (-COOH), at the other end has successfully produced water soluble quantum dots. This method was first described by Chan and Nie [3].

Other options are to grow a hydrophilic silica shell around the surface [10] or to coat the dots with a polymer and embed them in phospholipid micelles [19].

Once the quantum dots have been made water soluble, it is then possible to conjugate them to various biomolecules such as biotin, antibodies, and proteins

such as streptavidin. Such functionalised quantum dots can be used for a wide variety of biological applications and a selection of quantum dot-biomolecule conjugates, of various emission wavelengths are available to purchase 'off-the-shelf'. Figure 2.7 depicts the typical layered structure of quantum dots available to purchase from Invitrogen, Paisley, UK [2].

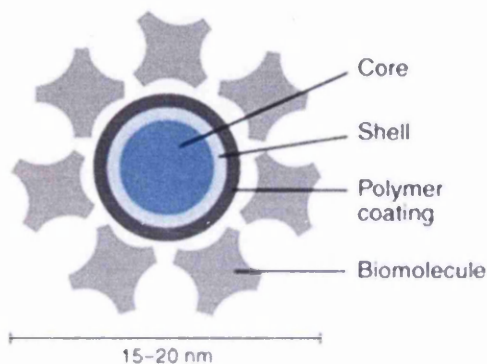


Figure 2.7: Illustration showing anatomy of quantum dot conjugate [2].

2.5.4 Properties for bio-medical applications

Quantum dots have unique optical properties which make them an attractive alternative to the traditional fluorophores that are routinely utilised in a multitude of biological and medical applications. The use of quantum dots has been reported in many recent publications: Fluorescent detection of specific biomarkers in immunoassays [3, 19, 20], and other high-affinity interactions [10, 21], including real-time and long-term studies of molecule tracking in living cells [21]; *in vivo* studies [19, 22]; genetics [23] and bio-sensing as reviewed by Sapsford *et al.* [24].

Unlike organic fluorophores, quantum dots exhibit narrow, symmetric emission spectra with a large Stokes shift. The effects of quantum confinement result in their emission wavelength being size dependent, as discussed in section (2.4) and illustrated in Figure 2.8(a). Thus, changing the size of the quantum dot, changes the band-gap energy and consequently the emission wavelength. More specifically, decreasing the size of the nanocrystals will result in a larger band-gap energy and therefore the quantum dot fluorescence will be 'blue-shifted'.

This ability to precisely tune the emission wavelength, by changing the size

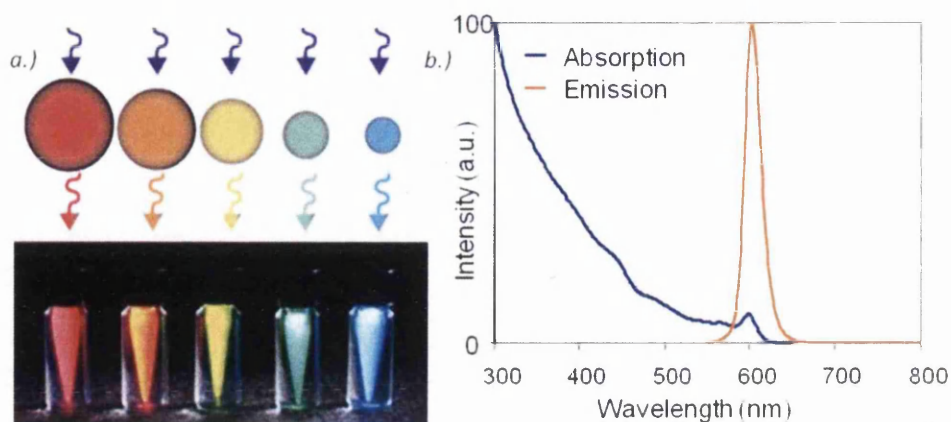


Figure 2.8: (a) Size dependent fluorescence emission due to quantum confinement effects. (b) Broad absorption and narrow emission spectra of 605 nm emitting quantum dots. Data from [2].

and/or the composition material, allows quantum dots with fluorescence emission ranging from UV - Infrared to be fabricated. Additionally, quantum dots possess continuous, broad absorption spectra which generally extend into the UV. This is demonstrated in Figure 2.8(b) which shows the absorption and emission spectra of red emitting CdSe/ZnS quantum dots.

These features facilitate multiplexing studies; where a mixed ensemble of quantum dots (with differing emission wavelengths), is simultaneously excited with a single light source. The illumination source used in multiplexing studies can be selected such that its wavelength is far removed from that of the emission wavelengths of the quantum dots present. This enables straightforward separation of fluorescence signals from the illuminating light. Typically, multiplexing studies involving organic fluorophores are difficult to implement since they have a relatively small Stokes shift. This can make it difficult to spectrally separate the emission fluorescence from one type of fluorophore from another, and also from the excitation source.

Moreover, quantum dots are significantly more resistant to photobleaching and chemical degradation than organic fluorophores. This has practical implications in long term imaging, for example in studies of transport processes, cell tracking and repeated imaging of a single sample. Their photostability is further enhanced by the addition of an inorganic capping layer that has larger band gap than that

of the quantum dot core material. This shell increases the quantum yield of the dots by reducing the probability of non-radiative recombination and reducing the effects of crystal defects at the surface. They also have a relatively long fluorescent lifetime, allowing the effects of background fluorescence to be minimised during fluorescence lifetime imaging microscopy (FLIM).

These properties are summarised in Table 2.1 and compared to typical optical properties of conventional fluorophores.

Property	Fluorophores	Quantum dots	Reference
Absorption spectra	Variable/narrow	Broad spectra, steadily increases towards the UV from the first absorption band edge	[18, 25-27]
Emission spectra	Broad, assymetric red-tailed emission	Narrow, Gaussian emission	[3, 18, 27]
Stokes shift	Generally <100 nm	>200 nm possible	[27, 28]
Tunable emission	NA	Unique to quantum dots; can be size/composition tuned from the UV to IR	[10, 28, 29]
Quantum yield	Variable	Generally high, 0.2 to 0.7 in buffer depending on surface coating	[17, 18, 25, 28]
Fluorescent lifetime	Short <5 ns	Long 10 - 20 ns or greater	[27, 28]
Spectral range	Fixed; a different dye every 40-60 nm	Tunable from UV - IR depending on material, Visible light from CdSe	[10, 18, 25, 28]
Photostability	Variable to poor	Excellent, strong resistance to photobleaching several orders of magitude that of dyes	[3, 10, 20]
Multiplexing capabilities	Rare	Excellent potential, largely unexplored	[10, 27, 28]
FRET capabilities	Variable, mostly single donor-single acceptor configurations	Excellent donors, size tune emission to improve the overlap with an acceptor dye	[30, 31]
Blinking	Negligible	Problematic in isolated circumstances (single molecule tracking)	[27, 28]
Reactivity	Multitude of conjugation chemistries commercially available	Availability of variety of conjugation chemistries improving	[2, 27]
Size	<0.5 nm	4-7 nm diameter for CdSe core material, up to 20 nm when conjugated	[2, 28, 29]

Table 2.1: *Comparison of quantum dots with fluorophores. Adapted from [24].*

2.6 Summary

Fluorescence techniques are routinely applied in many areas of cell and molecular biology. This chapter has introduced the principles of fluorescence which are

key to understanding the optical properties of fluorescent labels. Moreover this knowledge is necessary when developing protocols that utilise fluorescence, when solving imaging problems and are also important when selecting appropriate fluorescent labels.

The unique optical properties of semiconductor quantum dots have received much attention from the biomedical research community. Quantum dots are increasingly being used in many biological applications and are emerging as a new and improved class of fluorescent labelling agents. This chapter has reviewed many of these applications and has discussed the underlying principles that are responsible for their enhanced optical properties.

Bibliography

- [1] J. W. Lichtman and J. A. Conchello. Fluorescence microscopy. *Nature Methods*, 2(12):910–919, DEC 2005.
- [2] <http://www.invitrogen.com/site/us/en/home.html>.
- [3] W. C. W. Chan and S. M. Nie. Quantum dot bioconjugates for ultrasensitive nonisotopic detection. *Science*, 281(5385):2016–2018, 1998.
- [4] J. R. Lakowicz. *Principles of Fluorescence Spectroscopy*. Springer, 2006.
- [5] <http://www.microscopyu.com/articles/fluorescence/fret/fretintro.html>.
- [6] I. L. Medintz, A. R. Clapp, H. Mattoussi, E. R. Goldman, B. Fisher, and J. M. Mauro. Self-assembled nanoscale biosensors based on quantum dot fret donors. *Nature Materials*, 2(9):630–638, 2003.
- [7] R. M. Clegg. Fluorescence resonance energy transfer. *Current Opinion in Biotechnology*, 6(1):103–110, 1995.
- [8] A. Lewis and K. Lieberman. Near-field optical imaging with a non-evanescently excited high-brightness light-source of subwavelength dimensions. *Nature*, 354(6350):214–216, 1991.
- [9] C. B. Murray, D. J. Norris, and M. G. Bawendi. Synthesis and characterization of nearly monodisperse cde (e = s, se, te) semiconductor nanocrystallites. *Journal of the American Chemical Society*, 115(19):8706–8715, 1993.
- [10] M. Bruchez, M. Moronne, P. Gin, S. Weiss, and A. P. Alivisatos. Semiconductor nanocrystals as fluorescent biological labels. *Science*, 281(5385):2013–2016, 1998.
- [11] M. Nirmal and L. Brus. Luminescence photophysics in semiconductor nanocrystals. *Accounts of Chemical Research*, 32(5):407–414, 1999.
- [12] A. L. Efros and A. L. Efros. Interband absorption of light in a semiconductor sphere. *Soviet Physics Semiconductors - USSR*, 16(7):772–775, 1982.
- [13] L. E. Brus. Electron electron and electron-hole interactions in small semiconductor crystallites - the size dependence of the lowest excited electronic state. *The Journal of Chemical Physics*, 80(9):4403–4409, 1984.

- [14] S. V. Gaponenko. *Optical Properties of Semiconductor Nanocrystals*. Cambridge University Press, 1998.
- [15] A. I. Ekimov, F. Hache, M. C. Schanne-Klein, D. Ricard, C. Flytzanis, I. A. Kudryavtsev, T. V. Yazeva, A. V. Rodina, and A. L. Efros. Absorption and intensity-dependent photoluminescence measurements on cdse quantum dots: assignment of the first electronic transitions. *Journal of the Optical Society of America*, 10(1):100–107, 1993.
- [16] A. Javier, C. S. Yun, J. Sorena, and G. F. Strouse. Energy transport in cdse nanocrystals assembled with molecular wires. *The Journal of Physical Chemistry*, 107(2):435–442, 2003.
- [17] M. Hines and P. Guyot-Sionnest. Synthesis and characterisation of strongly luminescing zns-capped cdse nanocrystals. *Journal of Physical Chemistry*, 100:468–471, 1996.
- [18] B. O. Dabbousi, J. Rodriguez-Viejo, F. V. Mikulec, J. R. Hines, H. Mattoussi, R. Ober, K. F. Jensen, and M. G. Bawendi. (cdse)zns core-shell quantum dots: Synthesis and characterization of a size series of highly luminescent nanocrystallites. *Journal of Physical Chemistry*, 101(46):9463–9475, 1997.
- [19] B. Dubertret, P. Skourides, D. J. Norris, V. Noireaux, A. H. Brivanlou, and A. Libchaber. In vivo imaging of quantum dots encapsulated in phospholipid micelles. *Science*, 298(5599):1759–1762, 2002.
- [20] X. Wu, H. Liu, Q. Liu, K. N. Hayley, J. A. Treadway, J. P. Larson, N. Ge, F. Peale, and M. P. Bruchez. Immunofluorescent labelling of cancer marking her2 and other cellular targets with semiconductor quantum dots. *Nature Biotechnology*, 21(1):41–46, 2003.
- [21] J. K. Jaiswal, H. Mattoussi, J. M. Mauro, and S. M. Simon. Long-term multiple color imaging of live cells using quantum dot bioconjugates. *Nature Biotechnology*, 21(1):47–51, 2003.
- [22] X. et. al. Gao. In vivo cancer targeting and imaging with semiconductor quantum dots. *Nature Biotechnology*, 10:1038, 2004.
- [23] S. Pathak, S. K. Choi, N. Arnheim, and M. E. Thompson. Hydroxylated quantum dots as luminescent probes for *in situ hybridisation*. *Journal of American Chemical Society*, 123(17):4103–4104, 2001.
- [24] K. E. Sapsford, T. Pons, I. L. Medintz, and H. Mattoussi. Biosensing with luminescent semiconductor quantum dots. *Sensors*, 6:925–953, 2006.
- [25] *The molecular probes handbook - a guide to fluorescent probes and labeling technologies.* <http://www.invitrogen.com/site/us/en/home/References/Molecular-Probes-The-Handbook.html>.

- [26] C. A. Leatherdale, W. K. Woo, F. V. Mikulec, and M. G. Bawendi. *On the absorption cross section of cdse nanocrystal quantum dots*. The Journal of Physical Chemistry B, 106(31):7619–7622, 2002.
- [27] M. Ozkan. *Quantum dots and other nanoparticles: what can they offer to drug discovery?* Drug Discovery Today, 9(24):1065–1071, 2004.
- [28] X. Michalet, F. F. Pinaud, L. A. Bentolila, J. M. Tsay, S. Doose, J. J. Li, G. Sundaresan, A. M. Wu, S. S. Gambhir, and S. Weiss. *Quantum dots for live cells, in vivo imaging and diagnostics*. Science, 307(5709):538–544, 2005.
- [29] Alivisatos AP. *Semiconductor clusters, nanocrystals, and quantum dots*. Science, 271(5251):933–937, 1996.
- [30] A. R. Clapp, I. L. Medintz, J. M. Mauro, B. R. Fisher, M. G. Bawendi, and H. Mattoussi. *Fluorescence resonance energy transfer between quantum dot donors and dye-labeled protein acceptors*. Journal of the American Chemical Society, 126(1):301–310, 2004.
- [31] A. R. Clapp, I. L. Medintz, and H. Mattoussi. *Forster resonance energy transfer investigations using quantum-dot fluorophores*. ChemPhysChem, 7(1):47–57, 2006.

Chapter 3

Scanning near-field optical microscopy

3.1 Introduction

Advances across the science and engineering disciplines have constantly required the capacity to study materials on increasingly smaller dimensions. However, the resolutions achievable in conventional optical techniques are restricted by the diffraction limit to 200 – 300 nm, approximately half the wavelength of the visible illuminating light source.

The development of scanning probe techniques in the early 1980's enabled samples to be imaged with nanometre resolution and provided the ability to examine multiple features simultaneously. The advances in scanning probe microscopy (SPM) were pioneered by Binnig and Rohrer in 1982 by the invention of the scanning tunnelling microscope (STM) [1]. The technologies they developed in order to facilitate STM, proved to be a catalyst for the advancement of other SPM techniques, such as atomic force microscopy (AFM) [2] and scanning near-field optical microscopy (SNOM) [3, 4].

SNOM is somewhat unique in that it has the capacity to provide high-resolution optical and topographical information simultaneously from a wide variety of sample types. SNOM can be performed under ambient or near-physiological conditions and unlike STM, it does not require the sample to be conducting. Thus,

in recent years SNOM has emerged as a powerful tool for studying a variety of biological samples and is being increasingly applied across the life science discipline [5–10].

3.2 Optical resolution

In conventional optical microscopy techniques, much information is lost because of the limitations in spatial resolution. In the 19th century, Ernst Abbe [11] specified that the resolution of a lens, r , is given by the following relationship

$$r \geq \frac{\lambda}{2NA} \quad (3.1)$$

where λ is the illuminating wavelength; the numerical aperture, $NA = n \sin \alpha$; n is the refractive index of the imaging medium and α is half the acceptance angle of the lens, as illustrated in Figure 3.1.

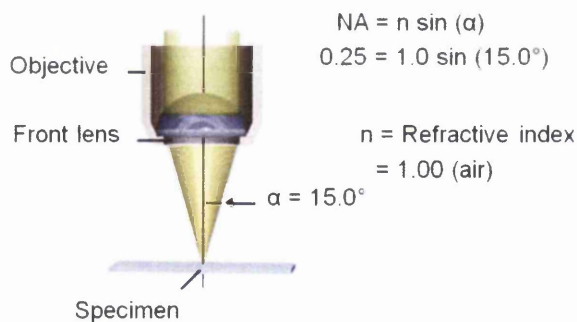


Figure 3.1: *Determination of the numerical aperture of a microscope objective lens. Adapted from [12].*

This limit in resolution was later redefined by Lord Rayleigh [13], to more precisely specify that two point sources can be resolved if they are separated by a distance R , where

$$R = \frac{1.22\lambda}{2n \sin \alpha} \quad (3.2)$$

This fundamental limit is known as known as the Rayleigh criterion. It can be seen from this criterion that improvements to the resolution can be accom-

plished by using a shorter wavelength to illuminate; by using a material of higher refractive index, for example an oil immersion lens; or by increasing the aperture angle. These changes however, do not result in significant improvements to the resolution and at best a resolving power only slightly better than 0.5λ can be achieved. Yet this resolution limit is only applicable when considering the propagating component of light.

Light is composed of propagating and non-propagating (evanescent waves) elements, thus one key to beating the diffraction limit lies with the ability to detect the non-propagating waves. In 1928, Synge [14, 15] proposed that this could be achieved by passing light through a sub-wavelength aperture in an opaque screen, in order to create an evanescent or near-field. As depicted in Figure 3.2, Synge proposed that the screen should be positioned within a few nanometers of the sample such that the evanescent waves generated at the aperture would interact with the surface.

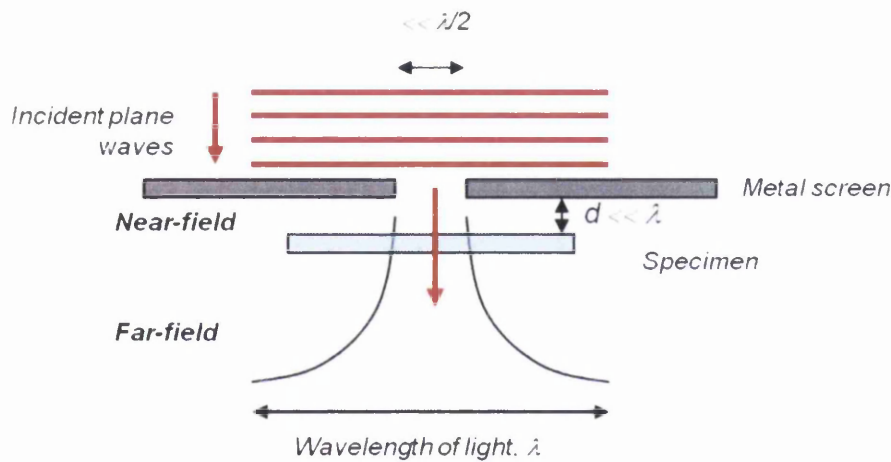


Figure 3.2: *Illustration of Synge's proposal. Evanescent field is generated by illuminating a sub-wavelength aperture. The sample is positioned such that interactions with the evanescent field occur and sub-wavelength information can be accessed.*

If the screen was then scanned across the surface in a raster fashion and the interactions detected, the resolution of the resulting image would be governed only by the size of the aperture and sub-wavelength information could be recorded. However, Synge realized that there were numerous technical difficulties that would

need to be addressed in order for his ideas to be realised: illumination; aperture formation and sample positioning. It took many years before technological advances had made sufficient progress and Synge's proposal could be implemented. In 1984, Pohl *et al.* [3] and Lewis *et al.* [4] simultaneously realised SNOM.

3.3 Evanescent waves

Evanescent waves are non-propagating components of electromagnetic waves and exhibit exponential decay with increasing distance from its source. They were first recorded by Newton during experiments on total internal reflection (TIR), which are illustrated in Figure 3.3.

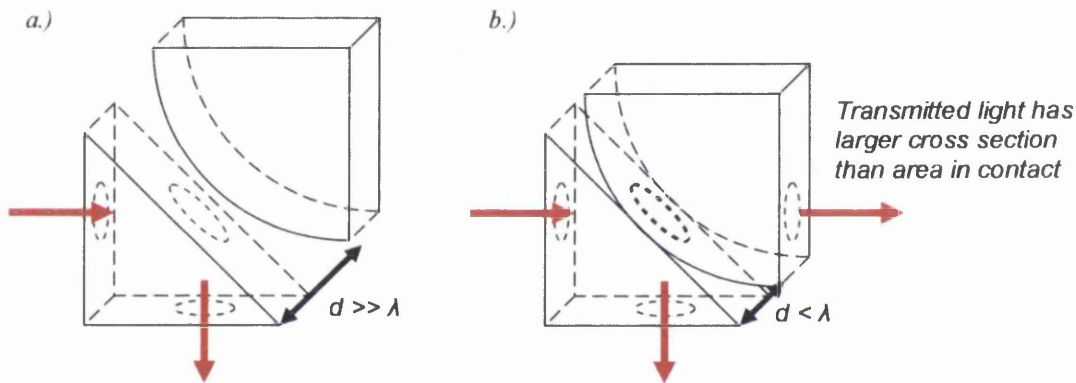


Figure 3.3: *Illustration showing Newton's TIR experiment. (a) A beam of light undergoes total internal reflection upon striking the prism surface (b) Frustrated TIR occurs when a second, curved prism is introduced to the first. The area of transmission is found to be larger than the region in contact.*

During his studies, Newton found that it was possible to totally reflect a beam of light inside a prism, providing the angle at which it strikes the inner surface of the prism is greater than the critical angle. By introducing a second, curved prism and placing it in contact with the first, Newton expected that the light would be transmitted only at the point of contact. However, he observed that the transmitted light had a larger cross-section than the area in contact.

This can be explained by the fact that electromagnetic fields must be continuous at a boundary: If a field exists at or inside a surface, it must also be present outside the surface. Such a field is found to propagate along the surface but

decays exponentially with increasing distance. This evanescent field is converted into propagating waves upon coupling to the second prism. The effect is known as photon tunnelling and can be generalised to other dielectric materials.

In order to describe the behaviour of an evanescent wave, consider an electromagnetic wave incident upon an interface, with angle greater than the critical angle such that TIR occurs, as illustrated in Figure 3.4. The transmitted wave

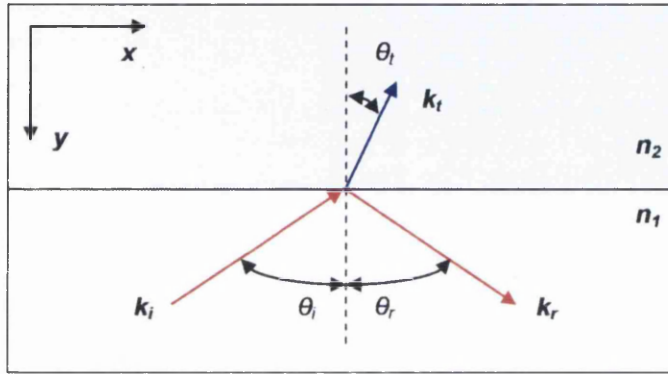


Figure 3.4: *Electric field incident on an interface between materials of differing refractive indices.*

vector can be expressed as

$$E_t(r, t) = E_{0t} \exp[i(\mathbf{k} \cdot \mathbf{r} - \omega t)] \quad (3.3)$$

and has components along and perpendicular to the interface. The wave vector component along the interface is given by

$$k_{tx} = \mathbf{k}_t \sin \theta_t \quad (3.4)$$

and the component perpendicular to the interface is

$$k_{ty} = \mathbf{k}_t \cos \theta_t \quad (3.5)$$

Using Snell's law of refraction, $(n_i \sin \theta_i = n_t \sin \theta_t)$, one finds that the per-

pendicular component of the transmitted wave vector can be expressed as

$$k_{ty} = k_t \cos \theta_t = k_t \sqrt{1 - \left(\frac{n_i}{n_t}\right)^2 \sin^2 \theta_i} = k_t \nu \beta \quad (3.6)$$

Therefore equation 3.3 can be re-written

$$E_t(x, y, t) = E_{0t} \exp[-k_t \nu \beta y] \exp[i(k_t \frac{n_i}{n_t} \sin \theta_i x - \omega t)] \quad (3.7)$$

Equation 3.7 describes an evanescent wave which decays exponentially with increasing distance from the interface (y -direction) and describes the propagation of the field in the plane of the interface (x -direction).

The behaviour of an evanescent field is described more generally by equation 3.8, as given by Courjon [16], where the field propagates along the surface in the (x, y) plane and decays exponentially in the z -direction. A is the amplitude of the field at (x, y, z) and the coefficient α depends upon the properties of the material and upon its spatial structure.

$$U(x, y, z, t) = \underbrace{A(x, y, z, t)}_{\text{Amplitude term}} \underbrace{\exp[-i(k_x x + k_y y)]}_{\text{Propagation term}} \underbrace{\exp[-\alpha z]}_{\text{Attenuation term}} \underbrace{\exp[i\omega t]}_{\text{Time-dependence term}} \quad (3.8)$$

3.4 Theory of SNOM

Newton's experimental work on frustrated TIR discussed in section 3.3, describes the formation of evanescent waves based on macroscopic interactions. In near-field microscopy, an evanescent field is generated by a sub-wavelength aperture, therefore diffraction effects must be taken into account.

The diffraction of electromagnetic radiation by a sub-wavelength hole in a conducting plane was first considered theoretically in a publication by Bethe [17]. The spatial distribution of the emitted radiation in the vicinity of the aperture was calculated, by applying boundary conditions to Maxwell's equations. However, Bethe's treatment of the problem was found not to accurately predict the behaviour of the fields in the vicinity of the aperture and was later corrected by Bouwkamp [18]. The work of Bethe and Bouwkamp provided a platform

for further studies that more accurately predict the distribution of the radiation emitted from a SNOM probe.

The behaviour of evanescent fields in the vicinity of limited objects (objects characterised by sub-wavelength features) was discussed by Wolf and Nieto-Vesprinas [19]. Their work shows that light incident on a limited object, i.e. a sample with sub-wavelength features, is converted into propagating and non-propagating components. The diffraction limited propagating components are carried away towards a detector, while the non-propagating components are confined to the surface of the object and contain the high spatial frequency information relating to the sample.

In order to detect these non-propagating components, the evanescent field must in turn be converted into both propagating and non-propagating components by a limited object, i.e. a sharp tip. Thus the corresponding propagating components can be detected and since the conversion between evanescent field and the detected field is linear, sub-wavelength information can be reproduced.

3.5 Heisenberg principle and near-field resolution

In order to determine ultimate resolution capabilities, one must neglect any technical difficulties and examine the relationship between near-field resolution and the Heisenberg uncertainty principle. Consider a point $P(x, y, z)$ that exists in an electric field $U(x, y, z)$ as shown in Figure 3.5. The electric field can be described by its amplitude at this point and by a propagation vector k . The field strength is given by

$$k = \frac{2\pi n}{\lambda} \tag{3.9}$$

where n is the refractive index of the medium through which the wave propagates. Since the electric field varies between two points, the minimum detectable variation in the field defines the ultimate resolution capabilities.

If $\Delta x, \Delta y, \Delta z$ are defined as the uncertainty in the position of point P and $\Delta k_x, \Delta k_y, \Delta k_z$ as the uncertainty in the propagation vector k , one can use the

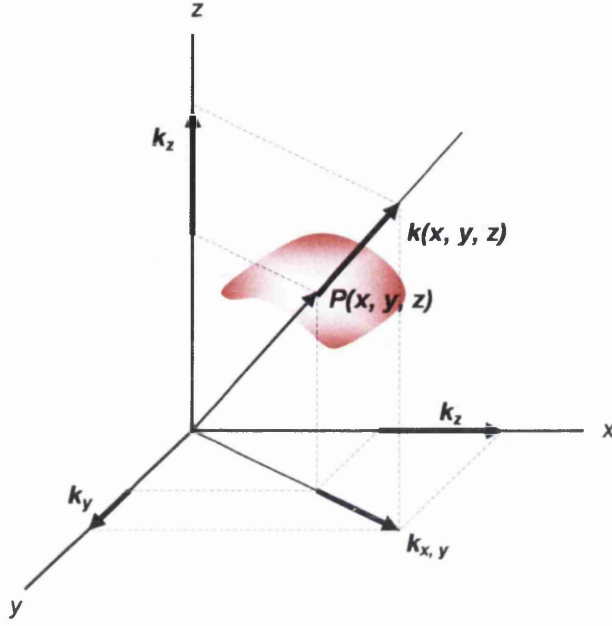


Figure 3.5: *Illustration of an electric field that is described by its amplitude and the propagation vector $k(x, y, z)$ at any point. The smallest detectable field variation is given by the Heisenberg principle and governs the near-field resolution.*

Heisenberg uncertainty relation to state

$$\Delta x \Delta k_x \geq 2\pi \quad (3.10)$$

and the same is true for the y and z -directions. It can be seen from equation 3.10 that Δx only takes small values when Δk_x is large, i.e. for a field which varies rapidly (Δx is small) the light is strongly scattered (Δk_x becomes large). To determine the largest value that k_x can take, consider the projection of the propagation vector onto the x -axis

$$k_x = |k| \sin \theta \quad (3.11)$$

thus k_x is always smaller than $|k|$. If $\delta k_x = 2k_{xMAX}$, where k_{xMAX} is the largest value that k_x can take, then equation 3.10 can be re-written to reproduce the Abbe limit

$$\delta x \geq \frac{\lambda}{2n \sin \theta} \quad (3.12)$$

However, given that

$$|k_x| = \sqrt{|k|^2 - k_y^2 - k_z^2} \quad (3.13)$$

if either the k_y or k_z components of the wave vector take complex values, $|k_x|$ will not be limited to $|k|$ as in equation 3.11, i.e. sub-wavelength resolutions can be achieved. For the case when k_x and k_y are real and k_z is imaginary, the wave propagates in the (x, y) directions and is confined in the plane of the surface (z - *direction*), as was described by equation 3.8.

3.6 Development of SNOM

In 1972, Ash and Nicholls [20] were the first to verify Synge's ideas experimentally, but not with visible light. Using microwave radiation of wavelength 3 cm to image a metal grating with regular spacings of 0.5 mm, they demonstrated that it was possible to achieve resolutions far beyond the diffraction limit of their radiation source. Although Ash and Nicholls recognised that fabricating apertures small enough for use with visible radiation was not an obstacle, they acknowledged that the development of a "super-resolution optical microscope" would be hindered by the difficulties in maintaining the sample position to within a distance approximately the size of the aperture.

In 1981, Binnig and Rohrer [1] developed the first STM which exploits the piezoelectric effect to achieve precise, nano-scale movements of a metal tip across the surface of a conducting or semi-conducting sample. The technological advances required for the STM lead to the development of AFM instruments [2], which make measurements of the interactions between a tip and sample.

The ability to achieve such fine movements in tip positioning facilitated the progress in developing a scanning near-field optical microscope and in 1984, two groups simultaneously reported to have extended the efforts made by Ash and Nicholls in order to utilize visible light. Pohl *et al.* [3] reported a maximum resolution of 25 nm using 488 nm radiation. This was realised by scanning a metal coated quartz tip with sub-wavelength aperture across a surface containing a series of opaque and transparent lines. While Lewis *et al.* [4, 21] demonstrated

resolutions of 50 nm using 500 nm radiation with their SNOM set-up.

3.7 Applications and typical set-up

Since these initial publications, there has been much progress in developing the SNOM technique and it has found applications in many disciplines. The original experimental set-up has been modified to facilitate a variety of purposes: Single molecule detection [22, 23]; fluorescence lifetime measurements [24, 25]; thin film analysis [26, 27] and Raman spectroscopy [28, 29]. In biological sciences, SNOM has been utilized for membrane studies [6, 30, 31]; protein localization [32] and it has been successfully applied to image in liquid environments [5, 33].

Although the actual experimental set-up employed will depend on the properties of the sample, a typical arrangement is shown in Figure 3.6. Laser light is coupled into a single-mode optical fibre and in turn coupled into a SNOM probe. Light emitted from the SNOM probe illuminates and excites the sample and the resulting fluorescence is collected by the objectives. Laser light can be removed from the signal by a Raman edge filter and in such a set-up any remaining fluorescence can be directed towards a detector. Multiple variations for the illumination of samples and the collection of fluorescence can be utilised, these are illustrated in Figure 3.7.

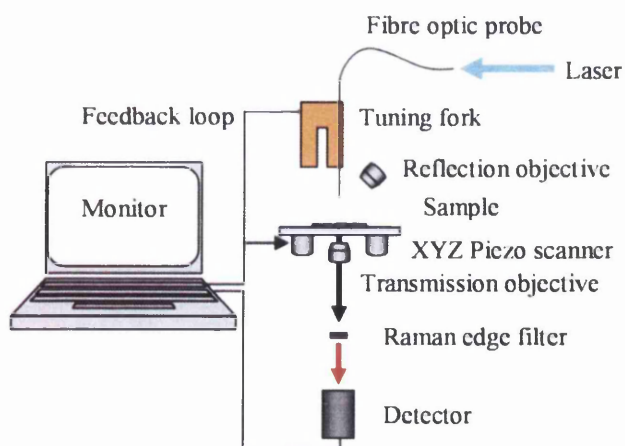


Figure 3.6: Schematic representation of typical SNOM experimental set-up.

3.8 SNOM probes

As with their SPM techniques, when imaging with a SNOM the probe is critical for obtaining high quality images. During the subsequent development of SNOM, extensive research on probe design was carried out. Various probe designs have been utilised including tapered optical fibres; pulled micro-pipettes and apertureless probes. Although aperture probes can be problematic and have numerous issues associated with their use (they are sensitive to heating effects and the ultimate resolution obtained is governed by the aperture size), they remain the most popular choice for use with both commercial and home-built SNOMs.

Commercially available, pulled-fibre optic probes were chosen for this work, thus their manufacture and operational modes will be discussed in this section.

3.8.1 Operational modes

There are several modes of operation available when utilising fibre optic probes with SNOM. These options provide a flexibility to select the most appropriate mode for scanning according to the properties of the sample.

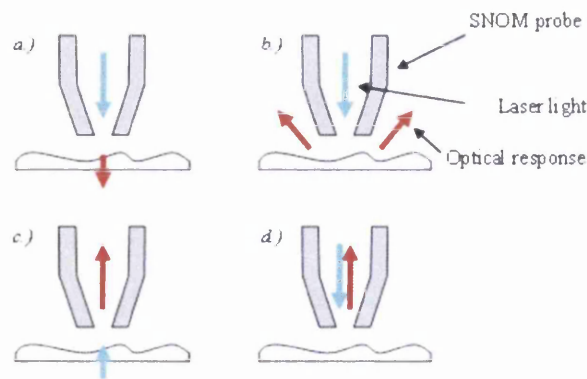


Figure 3.7: *Operational modes of SNOM when a fibre optic probe is utilised; (a) Probe illumination/Transmission collection, (b) Probe illumination/Reflection collection, (c) Probe collection, (d) Probe illumination/Probe collection mode.*

Illumination mode is implemented by coupling an external light source to the tail of the nano-apertured, fibre optic probe. Transmission through the aperture is of the order of $10^{-4} - 10^{-7}$, therefore this method lends itself well for use with photosensitive samples. Coupling of the evanescent light into the sample can lead

to propagating light, which in turn can be transmitted or reflected, as illustrated in Figures 3.7(a) and (b) respectively. This light from the sample is collected by an objective lens and directed towards a detector. Transmission collection mode requires the sample to be transparent, and the reflection collection mode is used for opaque samples. Probe collection mode is employed when the sample is illuminated externally or when the sample is optically active (for example a laser structure) as shown in Figure 3.7(c). Here the optical signal from the sample is collected up through the fibre probe and directed on to a detector. A further, more difficult, option is illustrated in Figure 3.7(d), where the probe is used to both illuminate the sample and to collect the optical response up through the fibre. Other options include monitoring sample response to light, for example using photocurrents. Filters and spectrometers can also be employed within these set-ups.

3.8.2 Manufacture

Fibre optic SNOM probes are routinely manufactured via controlled heating and pulling. Single mode optical fibres, with core diameter approximately $3\text{--}5\ \mu\text{m}$ are placed in a micro-pipette puller and heated under tension to create a sharp drawn taper, until eventually a breakage occurs. The taper and end aperture geometries are controlled by the heating and pulling parameters. The method results in highly reproducible tapered fibre optic probes.

The optical fibres are subsequently coated with an opaque metal in order to confine the light along the sides of the fibre. Aluminium is generally used due to its low skin depth for visible light, meaning only a thin coating is required to ensure optical opacity. Coating is achieved by thermal evaporation while rotating the probe at an angle, directed away from the aluminium source. This creates an even film along the length of the fibre and leaves the end aperture uncoated. Typically, the thickness of the aluminium coating is approximately $50\text{--}100\ \text{nm}$. Additives, such as chromium, may be involved to improve adhesion of the metal coating to the glass fibre taper.

3.9 Scanning technique

The ability to achieve sub-wavelength resolution when scanning with SNOM is subject to numerous technical difficulties. Since the near-field decays exponentially with increasing distance from the aperture of the probe, maintenance of a fixed tip-sample separation is vital. This ensures that the sample is positioned within, and illuminated by, the near-field and also ensures that the illumination power on the sample surface is constant throughout the duration of the scan. Maintaining a fixed tip-sample distance is also important to prevent tip damage caused by contact with the surface.

3.9.1 Feedback mechanism

As the topography of a sample changes during scanning, the separation between the tip and the surface is affected. A shear-force feedback mechanism is commonly employed to regulate a fixed tip-sample distance.

The fibre optic probe is mounted onto a tuning fork and oscillated at resonance laterally to the surface. As the probe-surface separation decreases, the oscillation amplitude becomes damped by the shear-forces acting between the probe and the sample surface. Maintaining a fixed oscillation amplitude forms the basis of the feedback signal which regulates the probe-surface separation. Thus, monitoring the necessary probe movements required to maintain a fixed separation effectively generates a topographic map of the surface.

3.9.2 Signal detection

Typically, low fluorescent signals are generated by the sample following excitation by the evanescent field that is emitted from the SNOM probe. Efficient mechanisms are therefore required to collect the optical signals. High numerical aperture, achromatic objectives are used to collect transmitted or reflected signals. Filters are then used to remove stray light and ensure that high signal-to-noise levels are achieved before the signal is focussed onto a detector. Highly sensitive detectors such as avalanche photodiodes (APDs) are typically employed

to monitor fluorescence. APDs are sensitive to low light levels and can in theory count individual photons by internally amplifying the photocurrent generated by incident photons.

Two silicon APDs (single photon counting modules from Perkin Elmer), with dark counts <100 Counts/s and <50 Counts/s were available for use during this study. In general, the APD with dark counts <50 Counts/s was utilised.

3.10 FRET SNOM

3.10.1 Introduction

The ultimate resolutions achievable with a conventional fibre optic probe are restricted. Reducing the aperture size to increase optical resolution results in low power throughput and consequently reduced fluorescent response.

The quest to achieve smaller resolutions has resulted in novel modifications to the typical SNOM set-up. One such example is the active or functionalised probe. This approach relies on Förster resonance energy transfer or FRET, a non-radiative energy transfer process between two fluorophores, an excited donor molecule and an acceptor molecule. The process of FRET depends highly on the physical separation between the donor-acceptor pair. The principles of FRET are discussed in more detail in section 2.2.7. By combining FRET with conventional SNOM, a powerful tool can be assembled with the ability to provide ultra-high resolution imaging. Thus, a FRET SNOM instrument has huge potential for the imaging of biological studies.

FRET SNOM was originally proposed as a means to improve the resolutions achievable with SNOM in 1991 [34] and has since been realised by numerous other research groups. To facilitate FRET SNOM imaging, donor (or acceptor) molecules are attached to the apex of a SNOM probe which is then utilised to scan a sample containing acceptor (or donor) molecules. Only the donor molecules are excited by the laser light emitted from the SNOM probe. As the tip scans across the sample, FRET occurs between the donor-acceptor pairs and the resulting acceptor fluorescence is detected. The resolutions are governed by the FRET

radius, which for good FRET pairs, is of the order of a few nanometers.

3.10.2 Realisation of active probes

Vickery and Dunn [35] were the first to demonstrate an improved resolution directly owing to the occurrence of FRET. Acceptor molecules, (Rhodamine dye molecules) were deposited onto the apex of a SNOM probe while donor molecules (Fluorescein) were incorporated into the sample. The acceptor/donor molecules were integrated into L-alpha-dipalmitoylphosphatidylcholine (DPPC) lipid films in order to ensure that the thickness of the dye films could be effectively controlled. A schematic illustration of the tip-sample configuration employed by Vickery and Dunn is shown in Figure 3.8(i). The sample consists of two DPPC/fluorescein layers separated by three layers of arachidic acid, while a single layer of DPPC/rhodamine has been deposited onto a (non-metal) coated SNOM probe.

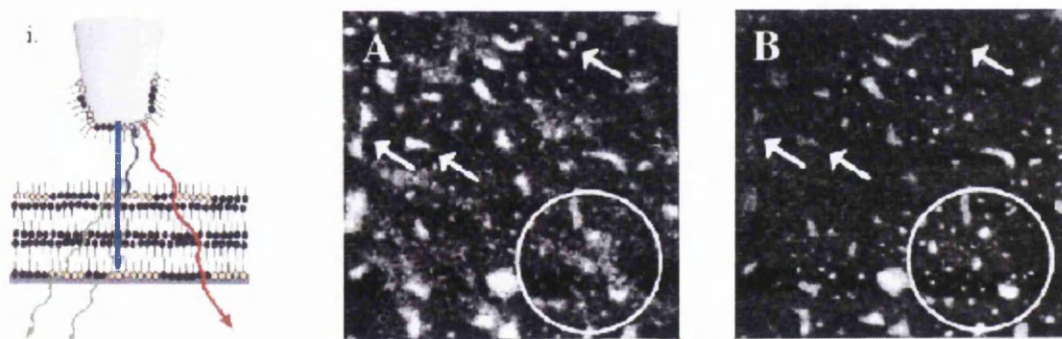


Figure 3.8: (i) Schematic representation of tip-sample configuration employed during FRET SNOM imaging; (A) $50\ \mu\text{m} \times 50\ \mu\text{m}$ SNOM image showing donor fluorescence; (B) FRET SNOM image showing acceptor fluorescence [35]

Vickery and Dunn demonstrated improvements in the resolution obtained by using a 458 nm excitation source, which predominantly excites the donor molecules, to scan the sample with the functionalised probe. The resulting fluorescence was collected and passed through a $548 (\pm 5)$ nm band pass filter, in order to observe only the fluorescence originating from the donor, as shown in Figure 3.8(A). An additional scan of this area was obtained, shown in Figure 3.8(B),

however during this scan, the fluorescence was passed through a 590 (± 5) nm band pass filter in order to observe only the acceptor fluorescence. In this second image, fewer fluorescent regions are observed (indicated by arrows in Figures 3.8(A) and (B)), owing to the fact that FRET is only efficient between the fluorescein dye in the upper layer of the sample and the rhodamine dye present on the tip apex. Upon comparison of the two circled regions in these images, an observed improvement to the resolution is seen in Figure 3.8(B). This improvement can be attributed to the distance dependent nature of the FRET process.

Since this original work by Vickery and Dunn, many other materials have been proposed and used to functionalise SNOM probes: Organic dyes [36]; nitrogen-vacancy colour centres in diamond [37]; gold nanoparticles [38] and F_2 colour centres in LiF [39]. The use of semi-conductor quantum dots in FRET SNOM applications has also been demonstrated. CdSe/ZnS quantum dots embedded in a polymer matrix were used to coat a SNOM probe by Shubeita *et al.* [40]. This probe was then used to image a sample doped with OM57 dye molecules and to demonstrate the occurrence of FRET. In another study, a polystyrene bead coated with CdTe quantum dots was attached to the apex of SNOM tip and which was subsequently utilised for FRET SNOM imaging [41]. More recently, a publication by Sonnefraud [42] has shown SNOM images recorded with the tip having a single, active quantum dot at the tip apex, although no FRET SNOM images were presented with such a tip.

3.11 Summary

SNOM was originally conceived by Synge [14] in 1928 however, its realisation was hindered by numerous technical difficulties. These issues were resolved following the invention of STM by Binnig and Rohrer [1] and the first SNOM was developed in 1984 [3, 4]. SNOM has since been increasingly utilised in a variety of applications, and undergone further developments to facilitate these studies.

The theory of SNOM and evanescent waves has been introduced in this section and the principles behind near-field detection have been outlined. A typical

SNOM set-up has been described and the mechanisms involved in scanning have been discussed. The quest to further improve the resolutions achievable has resulted in the development of functionalised probes to facilitate FRET SNOM. A summary of the literature has been presented in this section.

The versatility and flexibility afforded by SNOM is the key to its success across a variety of disciplines. For biological applications in particular, its ability to provide high-resolution optical and topographical information, makes SNOM an ideal instrument to probe structure-function relationships of cellular constituents. FRET SNOM has vast potential to further the progress in this area of research.

Bibliography

- [1] G. Binnig and H. Rohrer. Scanning tunneling microscopy. *Helvetica Physica Acta*, 55(6):726–735, 1982.
- [2] G. Binnig, C. F. Quate, and C. Gerber. Atomic force microscope. *Physical Review Letters*, 56(9):930–933, 1986.
- [3] D. W. Pohl, W. Denk, and M. Lanz. Optical stethoscopy: Image recording with resolution $\lambda/20$. *Applied Physics Letters*, 44(7):651–653, 1984.
- [4] A. Lewis, M. Isaacson, A. Harootunian, and A. Muray. Development of a 500 Å spatial resolution light microscope: I. light is efficiently transmitted through $\lambda/16$ diameter apertures. *Ultramicroscopy*, 13(3):227–231, 1984.
- [5] C. Höppener, J. P. Siebrasse, R. Peters, U. Kubitscheck, and A. Naber. High-resolution near-field optical imaging of single nuclear pore complexes under physiological conditions. *Biophysical Journal*, 88(5):3681–3688, 2005.
- [6] A. Ianoul, M. Street, D. Grant, J. Pezacki, R. S. Taylor, and L. J. Johnston. Near-field scanning fluorescence microscopy study of ion channel clusters in cardiac myocyte membranes. *Biophysical Journal*, 87(5):3525–3535, 2004.
- [7] R. M. Baylis, S. H. Doak, M. D. Holton, and P. R. Dunstan. Fluorescence imaging and investigations of directly labelled chromosomes using scanning near-field optical microscopy. *Ultramicroscopy*, 107(4-5):308–312, 2006.
- [8] L. Y. Zhong, W. T. Liao, X. P. Wang, and J. Y. Cai. Detection the specific marker of cd3 molecules of human peripheral blood t-lymphocytes using nsom and quantum dots. *Colloids and Surfaces A - Physicochemical and Engineering Aspects*, 313(Sp. Iss.):642–646, 2008.
- [9] L. Y. Zhong, G. C. Zeng, X. X. Lu, R. C. Wang, G. M. Gong, L. Yan, D. Huang, and Z. W. Chen. Nsom/qd-based direct visualization of cd3-induced and cd28-enhanced nanospatial coclustering of tcr and coreceptor in nanodomains in t-cell activation. *PLoS ONE*, 4(6):e5945, 2009.
- [10] M. Hofer, S. Adamsmaier, T. S. van Zanten, L. A. Chtcheglova, C. Manzo, M. Duman, B. Mayer, A. Ebner, M. Moertelmaier, G. Kada, M. F. García-Parajó, P. Hinterdorfer, and F. Kienberger. Molecular recognition imaging using tuning fork-based transverse dynamic force microscopy. *Ultramicroscopy*, 110(6):605–611, 2010.

-
- [11] E. Abbe. Beitrge zur theorie des mikroskops und der mikroskopischen wahrnehmung. *Arch. mikrosk. Anat. Entwicklungsmech.*, 9:413–468, 1873.
- [12] <http://www.microscopyu.com/articles/formulas/formulasna.html>.
- [13] Lord Rayleigh. Investigations in optics with special reference to the spectroscope. *Philosophical Magazine*, 8:261–274, 1879.
- [14] E. H. Synge. A suggested method for extending microscopic resolution into the ultra-microscopic region. *Philosophical Magazine*, 6:356–362, 1928.
- [15] E. H. Synge. An application of piezoelectricity to microscopy. *Philosophical Magazine*, 13:297, 1932.
- [16] D. Courjon and C. Bainier. Near field microscopy and near field optics. *Reports on Progress in Physics*, 57(10):989–1028, 1994.
- [17] H. A. Bethe. Theory of diffraction by small holes. *The Physical Review*, 66(7-8):163–182, 1944.
- [18] C. J. Bouwkamp. Diffraction theory. *Reports on Progress in Physics*, 17(1):35–100, 1954.
- [19] E. Wolf and M. Nieto-Vesperinas. Analyticity of the angular spectrum amplitude of scattered fields and some of its consequences. *Journal of the Optical Society of America A-Optics and image science*, 2(6):886–889, 1985.
- [20] E. A. Ash and G. Nicholls. Super-resolution aperture scanning microscope. *Nature*, 237:510–512, 1972.
- [21] A. Lewis, M. Isaacson, A. Muray, and A. Harootunian. Scanning optical spectral microscopy with \AA spatial resolution. *Biophysical Journal*, 41(2):A405, 1983.
- [22] E. Betzig and R. J. Chichester. Single molecules observed by near-field scanning optical microscopy. *Science*, 262(5138):1422–1425, 1993.
- [23] J. K. Trautman, J. J. Macklin, L. E. Brus, and E. Betzig. Near-field spectroscopy of single molecules at room-temperature. *Nature*, 369(6475):40–42, 1994.
- [24] X. S. Xie and R. C. Dunn. Probing single-molecule dynamics. *Science*, 265(5170):361–364, 1994.
- [25] W. P. Ambrose, P. M. Goodwin, J. C. Martin, and R. A. Keller. Alterations of single-molecule fluorescence lifetimes in near-field optical microscopy. *Science*, 265(5170):364–367, 1994.
- [26] J. W. Blatchford, T. L. Gustafson, A. J. Epstein, D. A. VandenBout, J. Kerimo, D. A. Higgins, P. F. Barbara, D. K. Fu, T. M. Swager, and A. G. MacDiarmid. Spatially and temporally resolved emission from aggregates in conjugated polymers. *Physical Review B*, 54(6):R3683–R3686, 1996.

-
- [27] J. A. DeAro, K. D. Weston, S. K. Buratto, and U. Lemmer. Mesoscale optical properties of conjugated polymers probed by near-field scanning optical microscopy. *Chemical Physics Letters*, 277(5-6):532–538, 1997.
- [28] V. Deckert, D. Zeisel, R. Zenobi, and T. Vo-Dinh. Near-field surface enhanced raman imaging of dye-labeled dna with 100-nm resolution. *Analytical Chemistry*, 70(13):2646–2650, 1998.
- [29] C. L. Jahncke, M. A. Paesler, and H. D. Hallen. Raman imaging with near-field scanning optical microscopy. *Applied Physics Letters*, 67(17):2483–2485, 1995.
- [30] J. Hwang, L. A. Gheber, L. Margolis, and M. Edidin. Domains in cell plasma membranes investigated by near-field scanning optical microscopy. *Biophysical Journal*, 74(5):2184–2190, 1998.
- [31] F. de Lange, A. Cambi, R. Huijbens, B. de Bakker, W. Rensen, M. García-Parajó, N. van Hulst, and C. G. Figdor. Cell biology beyond the diffraction limit: near-field scanning optical microscopy. *Journal of Cell Science*, 114(23):4153–4160, 2001.
- [32] M. García-Parajó, B. de Bakker, M. Koopman, A. Cambi, F. de Lange, C. Figdor, and N. van Hulst. Near-field fluorescence microscopy an optical nanotool to study protein organisation at the cell membrane. *NanoBioTechnology*, 1(1):113–120, 2005.
- [33] M. Koopman, A. Cambi, B. I. de Bakker, B. Joosten, C. G. Figdor, N. F. van Hulst, and M. F. García-Parajó. Near-field scanning optical microscopy in liquid for high resolution single molecule detection on dendritic cells. *FEBS Letters*, 573(1-3):6–10, 2004.
- [34] A. Lewis and K. Lieberman. Near-field optical imaging with a non-evanescently excited high-brightness light source of sub-wavelength dimensions. *Nature*, 354:214, 1991.
- [35] S. A. Vickery and R. C. Dunn. Scanning near-field fluorescence resonance energy transfer microscopy. *Biophysical Journal*, 76(4):1812–1818, 1999.
- [36] G. T. Shubeita, S. K. Sekatskii, G. Dietler, and V. S. Letokhov. Local fluorescent probes for the fluorescence resonance energy transfer scanning near-field optical microscopy. *Applied Physics Letters*, 80(15):2625, 2002.
- [37] S. Kühn, C. Hettich, C. Schmitt, J-PH. Poizat, and V. Sandoghdar. Diamond colour centres as a nanoscopic light source for scanning near-field optical microscopy. *Journal of Microscopy*, 202(1):2, 2001.
- [38] T. Kalkbrenner, M. Ramstein, J. Mlynek, and V. Sandoghdar. A single gold particle as a probe for apertureless scanning near-field optical microscopy. *Journal of Microscopy*, 202(1):72, 2001.

- [39] S. K. Sekatskii, G. Dietler, F. Bonfigli, S. Lorcti, T. Marolo, and R. M. Montereali. Subwavelength-size local fluorescent sources based on color centers in lithium fluoride for scanning near-field optical microscopy. *Journal of Luminescence*, 122-123:362, 2007.
- [40] G. T. Shubeita, S. K. Sekatskii, G. Dietler, I. Potapova, A. Mews, and T. Basché. Scanning near-field optical microscopy using semi-conductor nanocrystals as a local fluorescence and fluorescence resonance energy transfer source. *Journal of Microscopy*, 210(3):274, 2003.
- [41] F. Müller, S. Götzinger, N. Gaponik, H. Weller, J. Mlynek, and O. Benson. Investigation of energy transfer between cdte nanocrystals on polystyrene beads and dye molecules for fret-snom applications. *The Journal of Physical Chemistry*, 108:14527, 2004.
- [42] Y. Sonnefraud, N. Chevalier, J.-F. Motte, S. Huant, P. Reiss, J. Bleuse, F. Chandezon, M. T. Burnett, W. Ding, and S. A. Maier. Near-field optical imaging with a cdse single nanocrystal-based active tip. *Optics Express*, 14(22):10596, 2006.

Chapter 4

Cell biology

4.1 Introduction to human cell biology

The cell is the smallest functional unit of life. Living organisms may be composed of a single cell (such as bacteria) or cells may be the building blocks for more complex structures within organisms. There are many types of cells found within the human body. Although they share several common features, these different cell types have very specific functions to perform which is reflected in their structure. This is exemplified in Figure 4.1 which illustrates a selection of cells found in the human body.

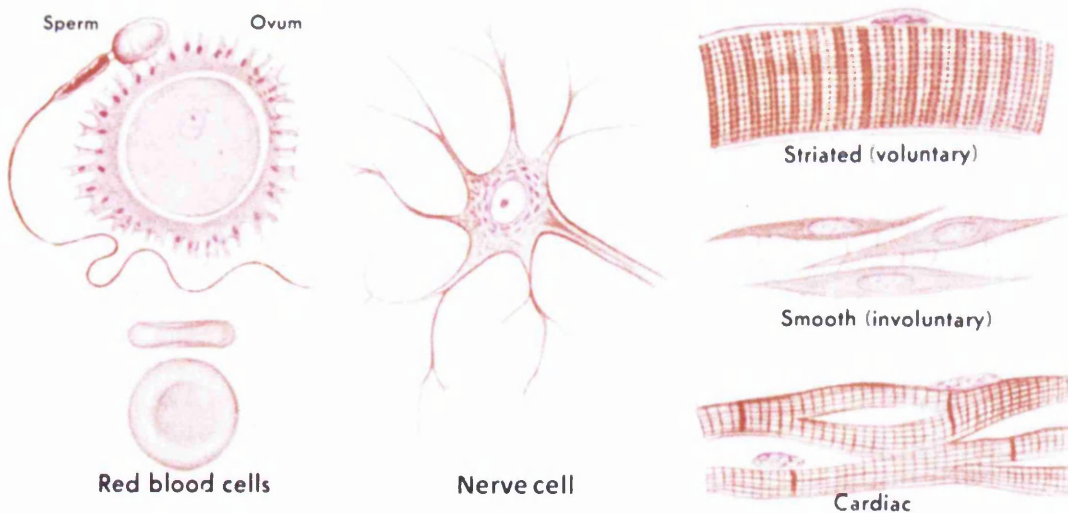


Figure 4.1: *Morphology of different cell types found in the human body. Adapted from [1].*

The structure of the cells is specifically designed to assist the cells in effectively performing their role within the body. For example, dendrites are branch-like structures found on nerve cells which receive electrical signals from other neurons. Whereas the biconcave disk morphology typical of red blood cell (also called erythrocytes), facilitates flow through the blood vessels. Human cells vary widely in shape and size depending on their function. However a general overview of cellular anatomy and common components is shown in Figure 4.2.

The nucleus is the control centre of the cell. The majority of a cell's genetic material is housed within the nucleus and is organised into long strands of DNA. These strands of DNA form structures called chromosomes. The nucleus is responsible for preserving the integrity of the genetic information, regulating gene expression and thus directing the activities of the cell.

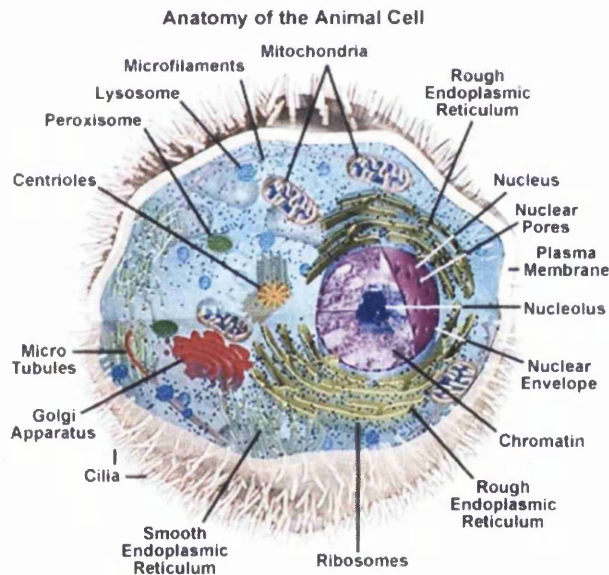


Figure 4.2: *General anatomy of an animal cell [2]*

The cytoplasm is the site of most cellular activities and contains most of the cell's organelles. For example; mitochondria, which are the powerhouse of the cell and the rough endoplasmic reticulum, which is the site of protein synthesis. The cytoplasm contains many filaments, such as actin and microtubules, which collectively form the cytoskeleton. These filaments act as a scaffold which maintains the architecture of the cell and also play a vital role in cell motility

through assembling cytoplasmic protrusions such as cilia, flagella, lamellipodia and filopodia.

Animal cells differ from plant cells in that they have only a plasma membrane, no cell wall is present. The plasma membrane is a lipid bilayer which surrounds the cytoplasm, isolating the cell from the external environment. Many proteins are embedded within the plasma membrane which perform a range of functions including transport into and out of the cell, cell adhesion and cell signalling. To provide cellular shape the cytoskeleton is anchored to the plasma membrane.

Cells of a particular type will often organise themselves into tissues which in turn combine to form organs. Tissues in humans are categorised into four main types: Connective, muscular, nervous and epithelial tissue. The epithelium is a layer of cells that forms a lining on all cavities and structures within the body and on exterior surfaces. The epithelium forms the basis of the investigations undertaken in this thesis.

4.2 Adhesion mechanisms

Cellular adhesion plays a vital role in the organisation of cells and in maintaining the overall architecture and function of tissues and organs. Adhesion between adjacent cells and binding to the extracellular matrix are both essential components of tissue formation. These rely on an array of adhesion receptors and the formation of thousands of adhesive contacts. Furthermore, cellular adhesion is a dynamic process and requires continuous maintenance to sustain stable contacts.

Multiple proteins are involved in any one adhesion complex, of which there are numerous types. Each type of adhesion complex is grouped together on the membrane in regions known as junctions. A schematic illustration of the various junctions abundant in epithelial tissues is presented in Figure 4.3. The basis of each junctional complex involves transmembrane proteins that interact with similar proteins on other cells to form cell-cell contacts, or directly with the extracellular matrix. The formation of stable adhesive contacts also requires interactions between the cytoplasmic domain of these transmembrane proteins

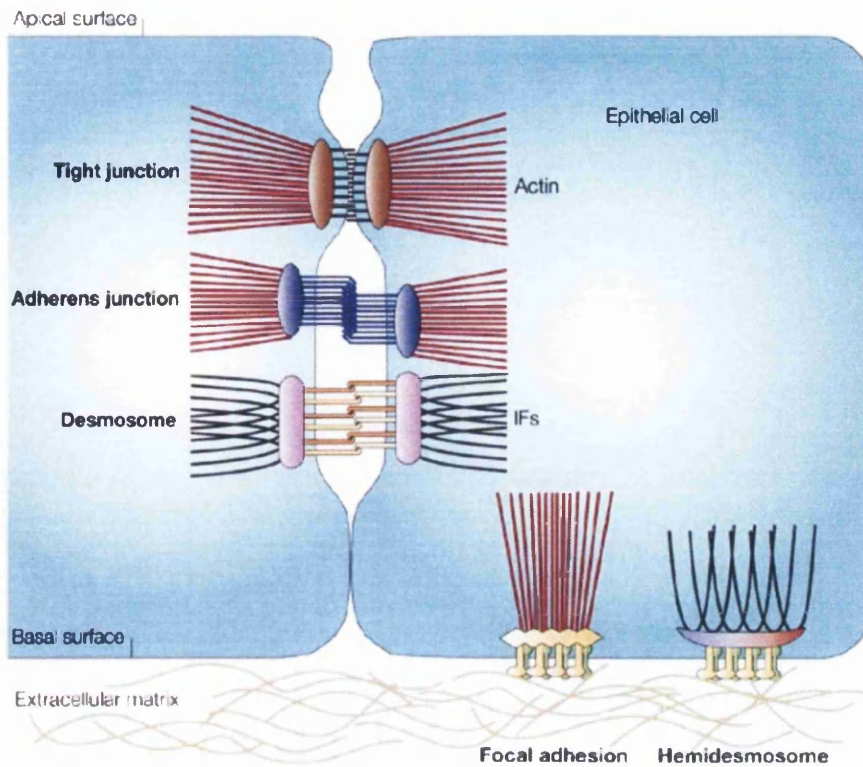


Figure 4.3: *Cellular junctions present in epithelial tissues. Adhesion between adjacent cells and binding to the extracellular matrix are essential to maintain tissue architecture. Adapted from [3].*

and the cytoskeleton, via a selection of intermediate plaque proteins.

As mentioned previously, epithelial tissues form a lining on all interior and exterior surfaces of the body. An essential property of epithelial tissues is the ability to selectively control their permeability to small molecules and ions. Tight junctions seal adjacent cells together and play an important role in the formation of a barrier between the apical and basal surfaces of tissues. Tight junctions divide tissues into two distinct regions that are biochemically separate. The transmembrane proteins responsible for the formation of tight junctions are occludins and claudins, which link to the actin cytoskeleton through ZO proteins.

The principal mediators of cell-cell adhesion are the cadherins which form adherens junctions and are discussed in detail in the following section. The presence of adherens junctions promotes the formation of other junctional complexes [4]. Desmosomes are formed by desmosomal cadherins which link to the intermediate

filaments of the cytoskeleton, labelled by IF's on Figure 4.3. They are abundant in tissues which are subject to high levels of mechanical stress and act to resist the shearing effect of such forces [5]. Both focal adhesions and hemidesmosomes are responsible for the binding of cells to the extracellular matrix. Hemidesmosomes are similar to desmosomes in that they resist the effects of mechanical stress that is applied to the tissue. Focal adhesions play a central role during cell migration and are continuously assembled and disassembled. Focal adhesions also serve to communicate information to the cell regarding the extracellular matrix [6].

4.2.1 E-cadherin and the adherens junction

Like other cellular junctions, the adherens junction relies on the interaction of numerous proteins to mediate adhesion. The adherens junction links cells together through transmembrane glycoproteins called cadherins and also act as an anchor site for the actin cytoskeleton through specialised linker molecules called catenins.

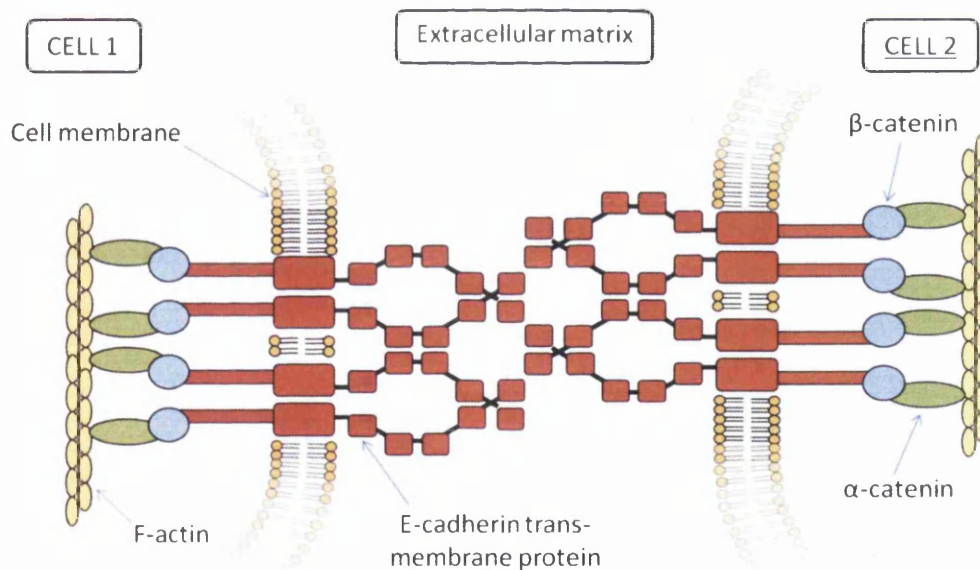


Figure 4.4: *Illustration showing mechanisms of E-cadherin mediated cell-cell adhesion and involvement of other proteins in adherens junction complex.*

E-cadherin is the foremost cadherin present in epithelial tissues. The extracellular domain of E-cadherin is responsible for mediating cell-cell adhesion via ho-

motypic, Ca^{2+} dependent interactions with similar molecules on opposing cells [4]. The illustration shown in Figure 4.4 demonstrates how E-cadherin molecules are directed outwards from the plasma membrane and each interdigitate with two further E-cadherin molecules from the opposing cell.

The cytoplasmic domain of E-cadherin can associate with a number of the catenin family of proteins. The catenin proteins link E-cadherin to the actin cytoskeleton and play an important role in maintaining proper cell-cell adhesion.

4.2.2 Role of actin filaments and filopodia

Filopodia are cytoplasmic projections that play an active role in cell migration. Filopodia are thin cylindrical structures that are packed with parallel bundles of filamentous (F)-actin. These dynamic structures are rapidly assembled and disassembled through actin polymerisation and are found on the leading edge of motile cells. Furthermore, they have been observed to sweep up and down, and from side to side while sensing their local environment. Their highly dynamic nature facilitates exploration of the extracellular matrix in their efforts to guide the cell and promote adhesion to other cells or to the substrate.

Analysis of these cell nano-structures has revealed that filopodia are typically found to measure 100 – 300 nm in diameter. However the degree to which they protrude from the membrane varies across different cell types. Due to their small dimensions and their dynamic properties, filopodia are known to be difficult to image as they often do not survive fixation. Consequently, these structures have been analysed using live imaging techniques. However when coupled with fluorescence, imaging of live samples can be problematic since this requires transfecting the cells with genetic material which encodes for a fluorescent protein. When the protein of interest is subsequently expressed in the transfected cell, the fluorescent protein will also be expressed and is tagged onto that protein. This enables live tracking of the movements of the protein through the cell. This technique is difficult to implement compared to immunofluorescence labelling of fixed cells.

In addition to their role in migration, filopodia have been shown to play an essential role in initiating cell-cell contact and in establishing adhesion between

adjacent cells. In a study of mouse keratinocytes, Vasioukhin et al [7] reported that calcium stimulates the formation of filopodia, which were subsequently observed making contact with opposing filopodia. The filopodia were observed to interdigitate and form anti-parallel dimers, before eventually embedding into the opposing cell membrane. The formation of adherens junctions occurred at the tips of these embedded filopodia and E-cadherin was visualised to form double rows of puncta through immunofluorescent labelling.

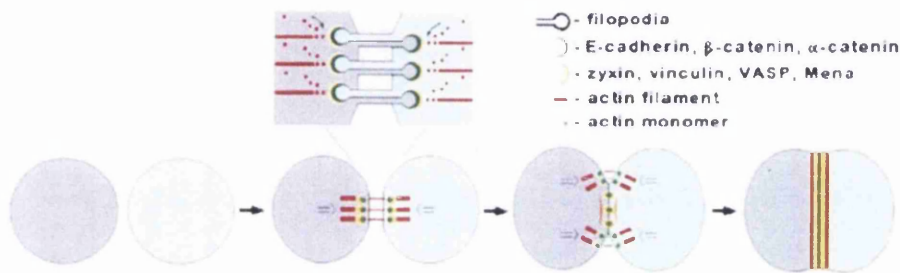


Figure 4.5: *Adjacent cells in close proximity extend filopodia across the intercellular region. Upon establishing contact, filopodia interdigitate and punctate adherens junctions form (green). Anchored filopodia tug the two cells together. As the gap closes, further adherens junctions are established and filopodia regress. F-actin (red) reorganises and aligns parallel to the sealed cells [7].*

As illustrated by Figure 4.5, this initial functional contact between opposing filopodia physically draws the cells together, gradually forming a seal between the two cells. The filopodia regress via actin depolymerisation and the initial double row of E-cadherin puncta closes to form a single row.

The actin cytoskeleton plays an active role in the formation of intercellular adhesion and is required to form a seal between adjacent cells [7]. As the gap between adjacent cells is closed, filopodia regress and F-actin filaments reorganise to align parallel to the sealed membranes. The actin filaments form a circumferential belt around the periphery of the cells [8].

4.3 Cancer

Maintenance and repair of tissues within the body requires that cells continuously grow and divide to replace old or damaged cells. This process is regulated

by the cell to ensure that growth takes place in a controlled manner. However various changes can occur during the lifetime of the cell which may result in the cell becoming defective in the mechanisms that underlie normal proliferation and homeostasis. These changes may be induced by numerous factors; for example DNA mutations can result from exposure to environmental carcinogens and mutagens. If these mutations are not removed or repaired by the cells various error-checking mechanisms, these mutations will be passed down to the daughter cells. The accumulation of these mutations over many generations of cells will cause a gradual change in the cells phenotype. Of special importance to the process of carcinogenesis is the inactivation of genes that are directly or indirectly involved with the regulation of the cell cycle. Other important genes include those that influence differentiation, regulate DNA repair machinery and maintain normal extracellular signalling, such as cell-cell adhesion.

Each case of cancer will progress in a slightly different manner but in general, there are multiple features that the majority of cancer cells will acquire during carcinogenesis. While some cancers may not progress to the later stages of carcinogenesis, instead forming non-invasive benign tumours, or acquire these features at different stages, this can be seen as a basic schematic for cancer progression.

Hanahan and Weinberg's review [9] provides a comprehensive outline of the mechanisms involved at the cellular level in cancer progression. The review identifies multiple abilities that cancer cells acquire which are summarised here.

1. **Growth Factors:** Normal cells require growth signals which instruct them to enter into an active proliferative state whereas this dependence appears reduced in tumour cells. This may be engendered through up-regulation of growth signalling receptors in tumour cells or the ability to synthesise their own growth factors to which they are responsive.
2. **Antigrowth signals and evasion of apoptosis:** Tumour cells are able to circumvent anti-growth signals which operate in healthy tissues and are able to avoid apoptosis (programmed cell death).

3. **Unlimited replicative potential:** Although properties 1 and 2 enable tumour cell populations to proliferate without inhibition, healthy cells have in-built mechanisms which limit the number of times they can divide. Thus for cancer cells to develop into much larger masses, cells must overcome this barrier and acquire the ability to replicate indefinitely.
4. **Angiogenic ability:** As a tumour develops the demand for oxygen and nutrients increases and the mass must acquire the ability to form new blood vessels.
5. **Invasion and metastasis:** Of particular interest to this study is the down-regulation of surface proteins which mediate cell-to-cell adhesion and binding to the extracellular matrix in late-stage cancerous cells. This leads to their being able to invade the local tissue. Ultimately they can become detached from the main tumour mass (primary tumour) and travel to a new region within the body through the blood or lymph nodes where secondary tumours will form (metastases).

The responsiveness of cancer to treatment will depend on the type of cancer and its stage of progression. However, in general the prognosis of a patient is significantly poorer when metastases are formed. Diagnosis of cancer is usually confirmed by histological examination of a biopsy specimen and histological markers can be helpful in determining the prognosis and in tailoring treatments for individual cases.

Prostate cancer is one of the most common malignancies in males and approximately 35,000 new cases are diagnosed every year in the UK. Prostate cancer can be a relatively slow growing disease and often patients will show no symptoms and require no treatment. However, prostate cancer has a propensity to metastasise, leading to poor patient prognosis especially when secondary tumours occur on the bones or lymph nodes.

4.3.1 Aberrant adhesion in prostate cancer

Normal cellular adhesion is essential for proper functioning of tissues and organs. Aberrant adhesion has implications in the development of many illnesses and diseases. A large body of research has been produced in an effort to better understand the mechanistic relationship between cellular adhesion and the metastatic capacity of tumours. E-cadherin is one of the principal mediators in epithelial cell-cell adhesion and its role in the progression and metastasis of cancer has been extensively studied. E-cadherin has been shown to act as a tumour invasion suppressor of numerous carcinomas [10–12].

Significant efforts have been made to find a clinical marker which would enable differentiation between relatively benign and invasive tumour types. Furthermore, a reliable prognostic marker would assist in tailoring medical treatment of individual patients. Numerous clinical studies have been undertaken to develop a deeper understanding of the role that E-cadherin and its associated proteins play in the progression of prostate cancer.

Umbas *et al.* [13, 14] reported that E-cadherin downregulation is linked to loss of prostate cancer tumour differentiation and more aggressive tumour grade. Furthermore, a reduced level of E-cadherin was shown to inversely correlate with poor patient survival rate. These results were confirmed in a later study by Cheng *et al.* [15]. E-cadherin's potential as a prognostic marker in prostate cancers was proposed as a result of these findings.

Subsequent clinical investigations have explored the relationship between E-cadherin and α -catenin and their role in maintaining adhesion. It was shown that α -catenin plays a vital role in the cadherin complex and its presence is required for E-cadherin function. Aberrant expression of α -catenin was found to be concomitant with abnormal E-cadherin levels. This was found to correspond with more aggressive prostate cancers and lower survival rates [16–18].

Numerous studies have since been undertaken which confirm E-cadherin's prognostic value. These studies indicate that a combination of the proteins involved in the cadherin complex may be more effective than E-cadherin alone as prognostic indicators [19–21]. Utilising a combination of these cadherin complex

proteins as prognostic markers has also been suggested for cancers originating in other organs, such as colorectal [22] and bladder cancer [23]. However a contradictory report by Bryden *et al.* [24], suggested that E-cadherin may not be critically related to metastasis following investigations which revealed E-cadherin to be strongly expressed in bone metastases. Furthermore, a study by McWilliam *et al.* [25] found no relationship between E-cadherin expression and tumour progression to bone metastases and overall survival of patients. It should be noted that McWilliam *et al.* [25] did find that E-cadherin expression was linked with tumour grade and invasion in prostate cancer.

Further investigations have been undertaken to investigate the role of adhesion in cancer metastasis. *In vitro* studies of human cancer cells have been undertaken in order to assess the phenotype of highly invasive prostatic cell lines. PC-3 is human prostate adenocarcinoma cell line which was derived from bone metastases. PC-3 cells have been shown to be highly invasive and metastatic, and form loose cell-cell contacts when cultured in a monolayer [26, 27].

Analysis of the phenotype of PC-3 cells has shown inconsistent information regarding E-cadherin expression. Morton *et al.* showed down regulation of E-cadherin expression in PC-3 cells compared to normal prostate epithelial cells. Furthermore, it was reported that α -catenin was completely absent at the protein and RNA levels suggesting aberrant α -catenin is responsible for the loss of adhesion (RNA is a nucleic acid that carries coding information from the DNA and instructs the cell to produce the associated protein). In contrast, other studies have shown through immunohistochemistry that E-cadherin is not present in PC-3 cells [28, 29]. However in two consecutive studies, Lang *et al.* reported paradoxical findings. The first report [27] found that PC-3 did not express E-cadherin. Lang *et al.* subsequently reported [30] E-cadherin was expressed in PC-3 but was not found localised in regions of the cell that confer cell-cell adhesion.

Additionally, the role of the cadherin complex in the invasive potential of PC-3 cells has been demonstrated by numerous studies. Ewing *et al.* [31] transfected PC-3 cells with α -catenin and observed dramatic alterations in cell morphology and increased cell-cell contact. The report suggested that re-expression of α -

catenin restored E-cadherin function. In a recent 2009 study, Zhou *et al.* [32] demonstrated that up-regulation of E-cadherin could be induced through treatment with luteolin, a dietary flavanoid which reduced the invasiveness of PC-3 cells.

Overall, these findings from clinical studies and *in vitro* analysis of prostate adenocarcinoma cell lines suggest a clear link between the aberrant expression and functioning of the cadherin complex and more aggressive prostate cancers. However, further research into the mechanisms of adhesion is necessary in order to provide more conclusive identification of potential prognostic markers. Investigations into the localisation and expression levels of E-cadherin are key to understanding its role in prostate cancer. Hence a high-resolution study which compares the localisation and expression in different cell lines through immunofluorescence labelling of E-cadherin is necessary.

4.4 Fluorescent labelling of target proteins *in situ*

Immunocytochemistry, or fluorescent labelling, is routinely employed to identify and examine cellular components. The technique reveals valuable information regarding the molecular make-up of the structures under scrutiny by localising specific, constituent proteins.

Immunocytochemistry relies on antibodies that can recognise and bind to specific cellular components. Antibodies are generated by injecting the molecule of interest, called an antigen, into a host species. The host's immune system responds by producing antibodies, also called Immunoglobulin G (IgG), that are specific to the injected antigen. These antibodies are then extracted from the host and purified. Thus an antibody produced in a rabbit to target antigen X, would be called rabbit anti-X IgG antibody. These antibodies may be directly conjugated to an identification marker, such as a fluorophore or quantum dot and applied to tissue samples or cells to locate the antigen on the sample.

Alternatively, a more versatile approach is afforded by employing indirect

labelling. Primary antibodies are generated as described for the direct method and are then injected into a second host of different species. Antibodies are generated by the secondary host which specifically target the primary antibodies. These secondary antibodies are subsequently extracted and can be coupled to biomolecules such as biotin or fluorophores. Thus a secondary antibody produced in a goat to target a primary antibody produced in a rabbit, would be called goat anti-rabbit IgG secondary antibody. The process of indirectly labelling a sample with quantum dots is shown in Figure 4.6 via two mechanisms.

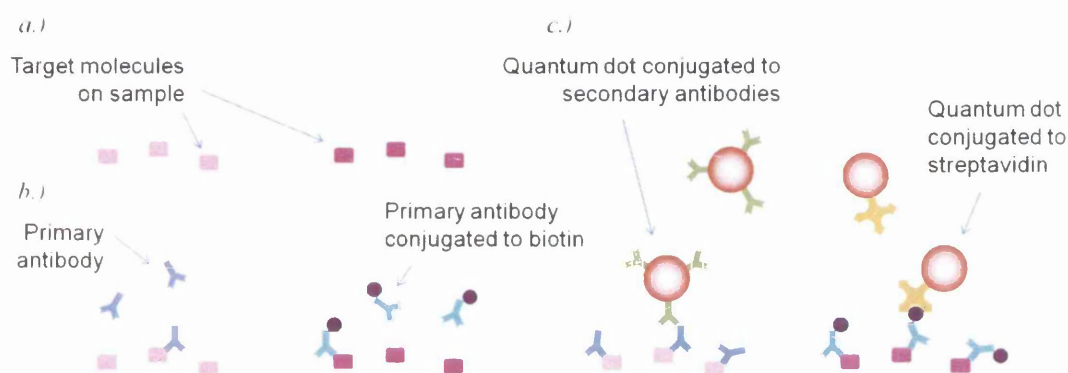


Figure 4.6: *Indirect method of immunofluorescent labelling. Target molecules (a) on cell membrane are first labelled by specific primary antibodies (b). Primary antibodies maybe conjugated to other molecules such as biotin. (c) Identification markers (for example quantum dots) maybe conjugated to secondary antibodies which seek out and attach to primary antibody. Alternatively, marker molecules can be conjugated to other biomolecules, such as streptavidin which have a high affinity to biotin.*

One demonstrates the use of primary and secondary antibodies, the other exploits the high affinity nature of biotin and streptavidin. The primary advantage of employing indirect labelling is that resulting fluorescent signals are enhanced. When using the direct method, only one fluorophore can bind to the primary antibody. In the indirect process, multiple secondary antibody conjugates can bind to the primary antibody which effectively amplifies the fluorescent response.

The use of antibodies in fluorescent labelling enables highly sensitive detection of biomolecules and proteins. Furthermore, multiple types of biomolecules on the same sample can be differentially labelled to allow simultaneous detection. This enables a more extensive investigation into the molecular make-up of a sample as

demonstrated by Figure 4.7. In this image (taken from [33]), three cellular targets are identified on the same cell and an overlay of the three colours is produced.

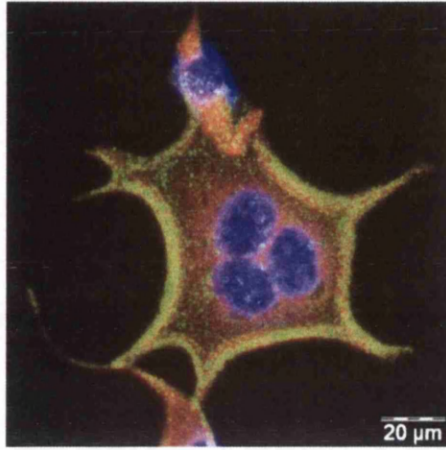


Figure 4.7: Multicoloured immunofluorescent image of human HeLa cells. Antibodies and labelling agents used to locate cadherin proteins (green), F-actin (red) and nucleus (blue) [33].

4.5 Summary

This chapter outlines the biological theories which provide the foundation for the studies contained in this thesis. Particular emphasis has been drawn to the roles that numerous cellular components play in establishing and maintaining cell-cell adhesion. The impact of abnormal cell-cell adhesion mediated by E-cadherin and its associated proteins has been discussed, specifically in relation to the progression and metastasis of prostate cancer.

A large body of research has been produced in order to develop a deeper understanding of the metastatic process. Numerous studies have shown E-cadherin to be lacking in both clinical specimens and cell lines deriving from prostate adenocarcinomas. Furthermore it has been demonstrated that the loss of E-cadherin expression or function is linked to increased invasiveness, metastatic potential and poorer patient prognosis. However, a small body of studies have argued against this consensus. These findings suggest additional investigations into the mechanisms involved in E-cadherin function are required before any conclusions

can be drawn about whether E-cadherin can be utilised effectively as a prognostic marker in prostate cancer.

This chapter has also introduced the principles behind fluorescence labelling techniques that are routinely used to study cell biology and the function of cellular components. The process of immunocytochemistry and the use of antibodies have been outlined as the method of choice for the sensitive detection of biomolecules and proteins.

Bibliography

- [1] <http://www.arthursclipart.org/medical/humanbody>.
- [2] <http://micro.magnet.fsu.edu/cells/animalcell.html>.
- [3] J. J. Jefferson, C. L. Leung, and R. K. H. Liem. Plakins: Goliaths that link cell junctions and the cytoskeleton. *Nature Reviews Molecular Cell Biology*, 5(7):542–553, 2004.
- [4] B. M Gumbiner. Cell adhesion: The molecular basis of tissue architecture and morphogenesis. *Cell*, 84(3):345–357, 1996.
- [5] B. Holthöfer, R. Windoffer, S. Troyanovsky, and R. E. Leube. Structure and function of desmosomes. In *Survey of Cell Biology*, volume 264 of *International Review of Cytology-A Survey of Cell Biology*, chapter 3, pages 65–163. Elsevier Academic Press INC, 2007.
- [6] D. Riveline, E. Zamir, N. Q. Balaban, U. S. Schwarz, T. Ishizaki, S. Narumiya, Z. Kam, B. Geiger, and A. D. Bershadsky. Focal contacts as mechanosensors: Externally applied local mechanical force induces growth of focal contacts by an mdial-dependent and rock-independent mechanism. *Journal of Cell Biology*, 153(6):1175–1185, 2001.
- [7] V. Vasioukhin, C. Bauer, M. Yin, and E. Fuchs. Directed actin polymerisation is the driving force for epithelial cell-cell adhesion. *Cell*, 100:209–219, 2000.
- [8] S. Yonemura, M. Itoh, A. Nagafuchi, and S. Tsukita. Cell-to-cell adherens junction formation and actin filament organisation: similarities and differences between non-polarized fibroblasts and polarized epithelial cells. *Journal of Cell Science*, 108(Part 1):127–142, 1995.
- [9] D. Hanahan and A. Weinberg. The hallmarks of cancer. *Cell*, 100:57–70, 2000.
- [10] U. H Frixen, J. Behrens, M. Sachs, G. Eberle, B. Voss, A. Warda, D. Ltehner, and W. Bircluneier. E-cadherin-mediated cell-cell adhesion prevents invasiveness of human carcinoma cells. *The Journal of Cell Biology*, 113(1):173–185, 1991.

-
- [11] K. Vleminckx, L. Vakaet, M. Mareel, F. Fiers, and F. Van Roy. Genetic manipulation of e-cadherin expression by epithelial tumor cells reveals an invasion suppressor role. *Cell*, 66(1):107–119, 1991.
- [12] M. J. G. Bussemakers, R. J. A. van Moorselaar, L. A. Girolodi, T. Ichitkawa, J. T. Isaacs, M. Takeichi, F. M. J. Debruyne, and J. A. Schalken. Decreased expression of e-cadherin in the progression of rat prostatic cancer. *Cancer Research*, 52(10):2916–2922, 1992.
- [13] R. Umbas, J. A. Schalken, T. W. Aalders, B. S. Carter, H. F. M. Karthaus, H. E. Schaafsma, F. M. J. Debruyne, and W. B. Isaacs. Expression of the cellular adhesion molecule e-cadherin is reduced or absent in high-grade prostate cancer. *Cancer Research*, 52(18):5104–5109, 1992.
- [14] R. Umbas, W. B. Isaacs, P. P. Bringuier, H. E. Schaafsma, H. F. M. Karthaus, G. O. N. Gosse, O. N. Oosterhof, F. M. J. Debruyne, and J. A. Schalken. Decreased e-cadherin expression is associated with poor prognosis in patients with prostate cancer. *Cancer Research*, 54(14):3929–3933, 1994.
- [15] L. Cheng, M. Nagabhushan, T. P. Pretlow, S. B. Amini, and T. G. Pretlow. Expression of e-cadherin in primary and metastatic prostate cancer. *American Journal of Pathology*, 148(5):1375–1380, 1996.
- [16] R. Umbas, W. B. Isaacs, P. P. Bringuier, Y. Xue, F. M. J. Debruyne, and J. A. Schalken. Relation between aberrant alpha-catenin expression and loss of e-cadherin function in prostate cancer. *International Journal of Cancer*, 74(7):374–377, 1997.
- [17] P. J. M. Richmond, A. J. Karayiannakis, A. Nagafuchi, A. V. Kaisary, and M. Pignatelli. Aberrant e-cadherin and alpha-catenin expression in prostate cancer: Correlation with patient survival. *Cancer Research*, 57(15):3189–3193, 1997.
- [18] S. Aaltomaa, P. Lipponen, M. Ala-Opas, M. Eskelinen, and V. M. Kosma. alpha-catenin expression has prognostic value in local and locally advanced prostate cancer. *British Journal of Cancer*, 80:477–482, 1999.
- [19] N. Morita, H. Uemura, K. Tsumatani, M. Cho, Y. Hirao, E. Okajima, N. Konishi, and Y. Hiasa. E-cadherin and alpha-, beta- and gamma-catenin expression in prostate cancers: correlation with tumour invasion. *British Journal of Cancer*, 79:1879–1883, 1999.
- [20] J. Z. Wang, D. Krill, M. Torbenson, Q. Wang, M. Bisceglia, J. Stoner, A. Thomas, P. DeFlavia, R. Dhir, and M. J. Becich. Expression of cadherins and catenins in paired tumor and non-neoplastic primary prostate cultures and corresponding prostatectomy specimens. *Urological Research*, 28(5):308–315, 2000.

- [21] I. M. van Oort, K. Tomita, A. van Bokhoven, M. J. G. Bussemakers, L. A. Kiemeney, H. F. M. Karthaus, J. A. Witjes, and J. A. Schalken. The prognostic value of e-cadherin and the cadherin-associated molecules alpha-, beta-, gamma-catenin and p120(ctn) in prostate cancer specific survival: A long-term follow-up study. *Prostate*, 67(13):1432–1438, 2007.
- [22] B. M. Ghadimi, J. Behrens, I. Hoffmann, W. Haensch, W. Birchmeier, and P. M. Schlag. Immunohistological analysis of e-cadherin, alpha-, beta- and gamma-catenin expression in colorectal cancer: Implications for cell adhesion and signaling. *European Journal of Cancer*, 35(1):60–65, 1999.
- [23] X. Garcia del Muro, A. Torregrosa, J. Muñoz, X. Castellsagué, E. Condom, F. Vigués, A. Arance, A. Fabra, and J. R. Germà. Prognostic value of the expression of e-cadherin and beta-catenin in bladder cancer. *European Journal of Cancer*, 36(3):357 – 362, 2000.
- [24] A. A. G. Bryden, A. J. Freemont, N. W. Clarke, and N. J. R. George. Paradoxical expression of e-cadherin in prostatic bone metastases. *British Journal of Urology International*, 84(9):1032–1034, 1999.
- [25] L. J. McWilliam, W. F. Knox, C. Hill, and N. J. R. George. E-cadherin expression fails to predict progression and survival in prostate cancer. *The Journal of Urology*, 155(Supplement 5):516A, 1996.
- [26] S. H. Lang, M. Stower, and N. J. Maitland. In vitro modelling of epithelial and stromal interactions in non-malignant and malignant prostates. *British Journal of Cancer*, 82(4):990–997, 2000.
- [27] S. H. Lang, R. M. Sharrard, M. Stark, J. M. Vilette, and N. J. Maitland. Prostate epithelial cell lines form spheroids with evidence of glandular differentiation in three-dimensional matrigel cultures. *British Journal of Cancer*, 85(4):590–599, 2001.
- [28] G. Davies, W. G. Jiang, and M. D. Mason. Cell-cell adhesion molecules and signaling intermediates and their role in the invasive potential of prostate cancer cells. *Journal of Urology*, 163(3):985–992, 2000.
- [29] P. M. Furbert-Harris, D. Parish-Gause, K. A. Hunter, T. R. Vaughn, C. Howland, J. Okomo-Awich, K. Forrest, I. Laniyan, A. Abdelnaby, and O. A. Oredipe. Activated eosinophils upregulate the metastasis suppressor molecule e-cadherin on prostate tumor cells. *Cellular and Molecular Biology*, 49(7):1009–1016, 2003.
- [30] S. H. Lang, C. Hyde, I. N. Reid, I. S. Hitchcock, C. A. Hart, A. A. G. Bryden, J. M. Vilette, M. J. Stower, and N. J. Maitland. Enhanced expression of vimentin in motile prostate cell lines and in poorly differentiated and metastatic prostate carcinoma. *Prostate*, 52(4):253–263, 2002.

- [31] C. M. Ewing, N. Ru, R. A. Morton, J. C. Robinson, M. J. Whccklock, K. R. Johnson, J. C. Barrett, and W. B. Isaacs. Chromosome-5 suppresses tumorigenicity of pc3 prostate-cancer cells - correlation with re-expression of alpha-catenin and restoration of e-cadherin function. *Cancer Research*, 55(21):4813–4817, 1995.
- [32] Q. Zhou, B. Yan, X. Hu, X.-B. Li, J. Zhang, and J. Fang. Luteolin inhibits invasion of prostate cancer pc3 cells through e-cadherin. *Molecular Cancer Therapeutics*, 8(6):1684–1691, 2009.
- [33] <http://www.abcam.com>.

Chapter 5

Experimental procedures

5.1 Introduction

This chapter describes the instrument developments required to facilitate the study of biological samples using scanning near-field optical microscopy (SNOM). Adaptations were made to standard sample handling configurations which enabled examination of samples using both fluorescence and SNOM techniques. Important aspects relating to the acquisition of SNOM images and subsequent image processing are also discussed.

Furthermore, this chapter contains full details of sample preparation methodologies and immunofluorescence labelling protocols that have been adapted for SNOM investigations. These protocols were optimised specifically to allow examination of samples with both the fluorescence microscope and the SNOM. The results and further optimisation of these protocols is detailed more fully in Chapter 7.

5.2 Equipment

5.2.1 Scanning near-field optical microscopy

Images were obtained primarily using an Aurora 3 scanning near-field optical microscope (Veeco Instruments), however some topographic imaging was carried

out using its predecessor, a Veeco Aurora 2. To illuminate samples, laser light was coupled to aluminium coated fibre optic probes. The fibre optic probes were purchased pre-mounted onto tuning forks with resonant frequency 80 – 110 kHz and the aperture of the SNOM probes were approximately 50 – 100 nm (Veeco Instruments). A 20 mW, 488 nm Ar^+ laser was used for these studies and a laser line filter was necessary to attenuate light at wavelengths not of this primary output wavelength. The instrument was operated in transmission mode and light was collected using a 40 \times , 0.65 numerical aperture collection objective. Collected light was directed out of the side of the SNOM unit and passed through a 488 nm Raman edge filter to remove laser light from the optical signal as illustrated in Figure 5.1.

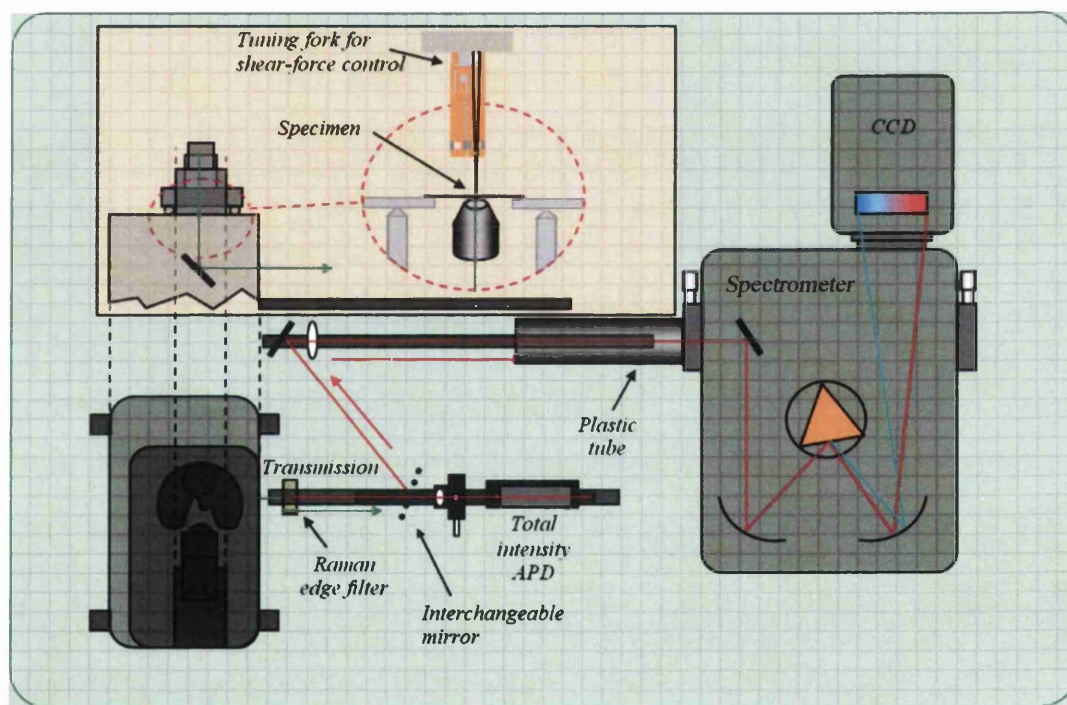


Figure 5.1: Graphic illustration of experimental arrangement used when examining biological samples with scanning near-field optical microscopy [1].

Additional filters can be inserted into the optical path immediately after the Raman edge filter if required. Band pass filters were utilised at this point in the optical path when studying samples which were labelled with two different colour quantum dots. This enabled fluorescence from each colour quantum dot

to be collected separately, identifying the location of two separate targets on the sample. Details of the filters used are given in Chapter 7.

Optical signals can be focussed onto an avalanche photodiode (APD) to count the total intensity. Alternatively, a 50 : 50 beamsplitter can be inserted into the optical path (location indicated by dotted line on Figure 5.1) to direct 50 % of the optical signal towards a spectrometer. The latter configuration allows collection of SNOM fluorescence images and enables the user to collect spectroscopic information from points of interest on the sample that are identified on the SNOM image.

The entire SNOM system and optical components shown in Figure 5.1 are fully enclosed to protect the APD from exposure to ambient light. This process also minimises background and ensures good signal-to-noise levels are achieved. The SNOM enclosure is mounted onto an anti-vibration table, reducing the risk of damage to the SNOM tip and subsequent aperture opening.

5.2.2 Fluorescence microscopy

The schematic illustration given in Figure 5.2 shows the standard configuration used in a fluorescence microscope. Typically a mercury lamp is used as the illumination source. White light from the lamp is passed through an excitation filter which allows only the desired wavelengths of light to pass through, and these are then directed onto the sample. A wide range of excitation filters are available, these are tailored towards the requirements of a specific fluorophore. For example a band pass filter centred on 482 nm with a band width of 18 nm would provide optimal excitation for Fluorescein (also known as FITC) or Alexa Fluor 488 fluorophores.

Light is collected from the sample and passed through an emission filter which eliminates background fluorescence and allows only the desired fluorescence to pass through. For example a band pass filter centred on 525 nm with a band width of 45 nm would be used to select fluorescence from Fluorescein or Alexa Fluor 488 fluorophores. Fluorescence can either be viewed through the eye piece or captured by the built-in camera. The resulting images generated are false

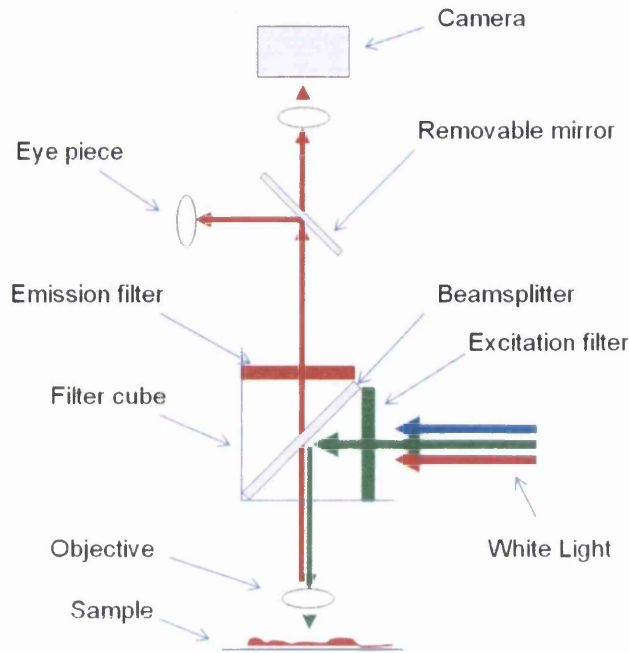


Figure 5.2: *Schematic illustration depicting configuration of a standard fluorescence microscope.*

colour and represent the intensity of the fluorescence detected.

It should be noted that the filter sets installed on the available fluorescence microscope were not optimal for the detection of quantum dot fluorescence. This is not important for the excitation filters since quantum dots have a broad absorption spectrum. However for the detection of fluorescence, the use of filters that are not tailored specifically to the emission wavelength of the fluorescent labelling agent can result in the loss of a proportion of the optical signals.

In this study, available filters sets which were the best match to quantum dot emission wavelength were utilised for all fluorescence microscopy. Specifications of the filters used are included in Appendix B.

5.2.3 Modifications to facilitate imaging of biological materials

A number of modifications were made to the SNOM arrangement to facilitate the study of biological specimens. In preparation for scanning a sample, the SNOM housing has a built-in light source that enables the user to view the sample

and SNOM tip on a monitor. This enables the user to select a suitable region on the sample to image and also to manually bring the tip into close proximity with the surface, while ensuring they do not make contact.

These initial stages require rather sensitive positioning of the tip and sample and therefore it is essential that the two are illuminated. However, this can become a problem when fluorescent samples are under investigation which are highly sensitive to light exposure and can become photobleached very rapidly. This can result in samples fading, or even becoming unusable before scanning has begun. For this reason light levels were kept to a minimum. Furthermore, the built-in white SNOM light was exchanged for a red light emitting diode (LED). This ensured that the incident light on the sample was largely non-bleaching to the fluorescent labels, which require light of higher energy/shorter wavelength to induce fluorescence.

The samples under investigation in this study were largely non-uniform. It was common to observe large areas of substrate where no cells were present, while in other regions the cells may be highly confluent. Where present, cells could be clearly visualised when samples were mounted on the SNOM sample stage and illuminated with the built-in SNOM light. Acquisition of SNOM images takes up to 3.5 hours depending on the scan size, thus a limited number of scans can be performed on a particular sample. It is important to ensure that the cells under examination are suitable in terms of their fluorescence labelling. While optimisation of the labelling methodology was carried out as fully as possible to ensure consistency, occasionally a proportion of the cells were poorly labelled or subject to high levels of localised non-specific labelling. It is important to rule out these regions for scanning with SNOM.

In order to achieve this, a far-field illumination configuration was devised which allowed examination of the samples using a similar principle to that of the fluorescence microscope. A schematic of this experimental arrangement is illustrated in Figure 5.3. The sample is placed on the SNOM scanner stage and is illuminated by laser light which is directed onto the sample using a fibre launch. The transmission objective is used to collect light and direct it towards

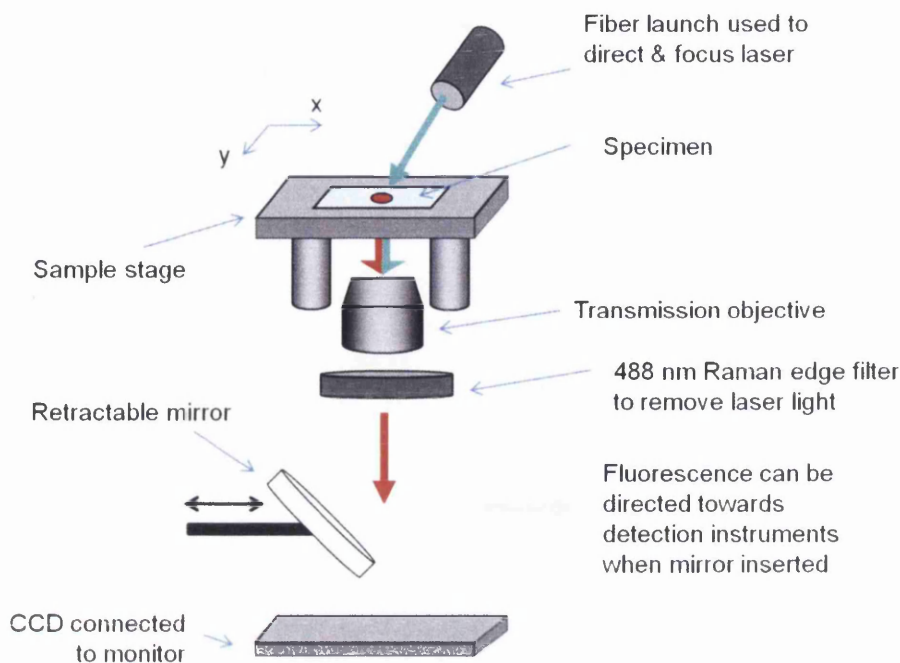


Figure 5.3: *Schematic illustration of far-field illumination set-up used to examine fluorescent samples by adapting SNOM instrumentation.*

the CCD, the resulting image can then be viewed on a monitor. By placing a Raman edge filter between the objective and CCD, laser light is removed and only the fluorescent signal is observed on the monitor. The sample stage can then be moved in the (xy) -direction to locate a region where labelling of cells is mostly specific. The fibre launch can then be removed, the SNOM head unit (which holds the SNOM tip) can be put in place and the exact region identified using this far-field set-up can be imaged.

Figure 5.4 shows photographs of a sample under far-field illumination. Figure 5.4(a) shows the sample as seen using the reflection objective to image the cells under standard illumination. A cluster of cells can clearly be observed in the centre of the screen. The photograph in Figure 5.4(b) shows the corresponding view as seen using the transmission objective and the far-field illumination configuration. Fluorescence can clearly be seen on the monitor, which aids the selection of suitable regions for scanning. The bright spot in the centre of the screen is due to a small amount of laser light bleeding through the Raman edge filter.

Although these adaptations allow exact regions to be selected based on their

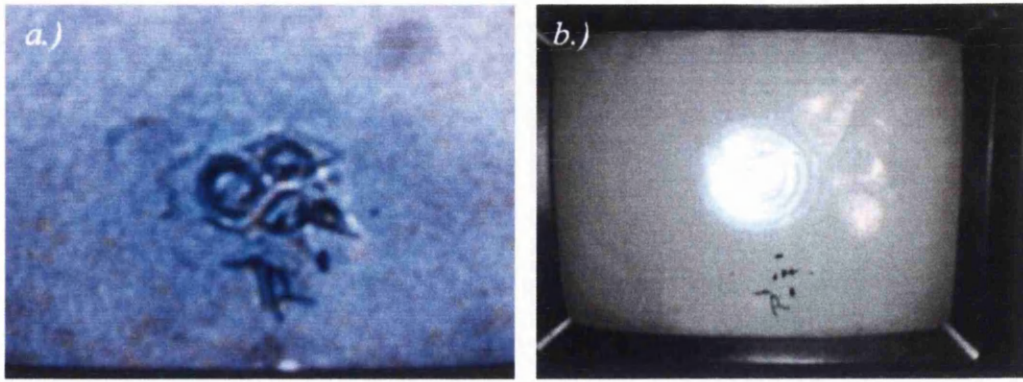


Figure 5.4: *Photographs demonstrating far-field illumination method to identify fluorescence from the sample. (a) Sample as seen by the reflection objective under standard illumination. A cluster of cells is present in the centre of the image. (b) Corresponding far-field illumination of the sample showing fluorescence.*

fluorescence labelling, the set-up must be dismantled in order to then subsequently image the sample using SNOM. The far-field configuration was re-installed each time a new region or sample is to be investigated, which was time consuming. In conjunction with long imaging times for SNOM, this made the overall acquisition of images a lengthy process.

A more versatile approach was afforded by the development of customised glass slides, as shown in Figure 5.5. This enabled all samples to be thoroughly examined using fluorescence microscopy prior to imaging with SNOM. For SNOM

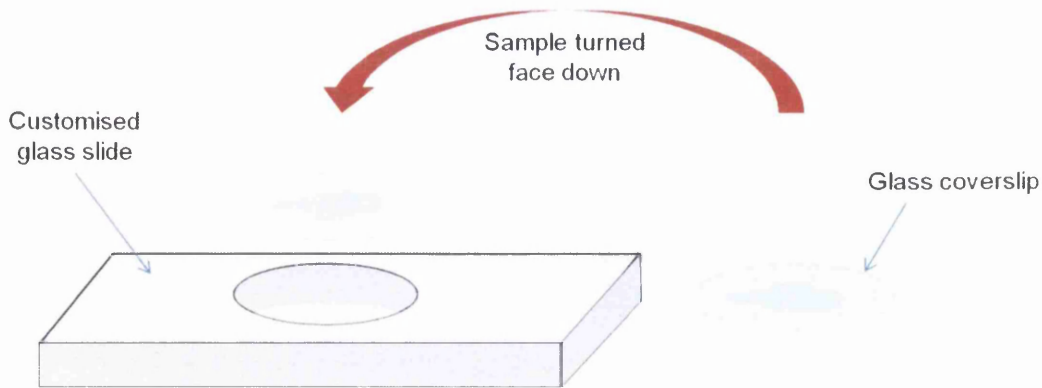


Figure 5.5: *Schematic illustration of customised glass slide which facilitates examination of samples with fluorescent microscopy prior to SNOM.*

imaging, samples were prepared on 25 mm diameter glass coverslips. Coverslips need to be mounted face-down onto glass slides in order to be examined using

the fluorescence microscope. Subsequent imaging of these samples using SNOM was not possible since the mounting of coverslips results in the surface becoming scratched and the topographic structure being damaged.

To facilitate examining samples with both techniques, glass slides were customised by drilling holes of approximately 20 mm in diameter as shown in Figure 5.5. This meant that any damage to the surface of samples due to mounting the coverslips face down would only occur around the outermost part of the sample. Each sample could then be imaged with both techniques. The use of these customised slides resulted in a much faster imaging of samples by ensuring only the most consistently labelled samples were examined with SNOM.

5.3 Image acquisition

5.3.1 Scanning parameters

The quality of the images acquired using SNOM largely depend on the scanning parameters set by the user and need to be determined experimentally for different sample types. When imaging biological specimens, which often have a large height range, slow scan rates must be used to ensure the SNOM tip has enough time to respond to any sudden changes in topography and avoid any contact between the tip and sample. The gain settings used to control the feedback mechanism which maintains the tip-sample distance, also greatly affect how the tip responds to these changes in height. A compromise must be found between ensuring the tip can respond rapidly to sudden changes in height while still being able to track finer topographic details.

This is exemplified in Figure 5.6 which shows SNOM acquisitions of human epithelial cells. The cells under scrutiny possess abrupt features which makes achieving high quality topography images using SNOM considerably difficult. Dramatic changes in height require very precise optimisation of scanning parameters. If the scan speed or gain settings are not fully optimised for the sample, the SNOM scanner cannot respond to such features as quickly as is required. This results in the tip being unable to track the surface accurately and tip crashes

become more likely.

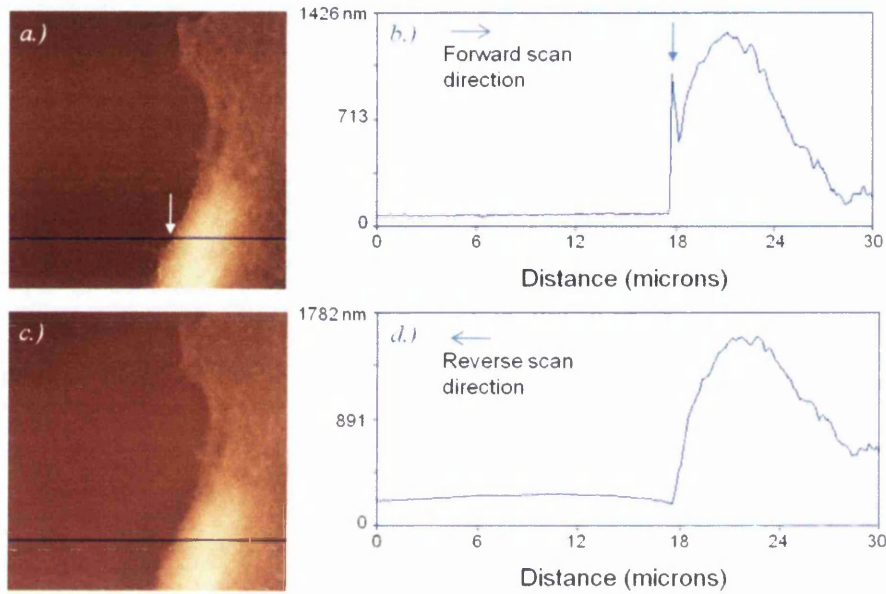


Figure 5.6: *High features often cause the tip to overcompensate for sudden changes in height. (a) $30\mu\text{m} \times 30\mu\text{m}$ SNOM topography image in the forward direction. Blue line in (a) corresponds to the cross-section shown in image (b) which shows tip overshoot (indicated by arrow) in response to abrupt topography change. (c) Reverse direction topography image and (d) corresponding cross-section showing no such overshoot.*

Figure 5.6 shows two SNOM topography acquisitions of the same region, one in the forward direction (a) and one in the reverse direction (c). The cross-sections shown in (b) and (d) correspond to the lines identified on the respective topography images (a) and (c). As can be seen in the images, increases in sample height occur much more rapidly in the forward direction while a more gentle gradient occurs due to increases in height in the reverse direction. The sudden increase in height in the forward direction has resulted in the tip overcompensating and retracting from the surface further than is necessary. This is identified by arrows in both Figures 5.6(a) and (b) but is more prominent in the cross-section data given in (b). As a result of the tip overshooting, an artefact is present in the topography image shown in (a) and appears as a bright line along the majority of the cell edge.

Examination of the reverse direction in Figure 5.6(d) reveals no spike and no such artefact can be seen along the cell edge in topography image (c). This

confirms that the feature is in fact an artefact and not a real topographic feature. In this case, scanning parameters would require further adjustment.

The number of pixels that each image is composed of is defined by the user. This can have a great influence on the quality of the images, which is of particular importance on large scans and this can determine the resolutions which are achieved. Typically, a resolution of 300×300 pixels was selected. Furthermore, when acquiring optical images with SNOM, the user must define the integration time for the APD. This is the length of time light is collected by the APD from each image pixel. A compromise must be reached in defining this parameter. Too short an integration time will result in poor fluorescence images, while too long an integration time will result in increased scan times since this setting will override the pre-defined scan rate. In this study, an integration time of 20 ms was selected when acquiring SNOM fluorescence images and scan rates were typically set at around $3 \mu\text{ms}^{-1}$.

5.3.2 Image processing

Minimal image processing was carried out following acquisition of images using SNOM. Most topography images required levelling adjustment to account for sample tilt. Performing levelling on an image allowed accurate measurements of height. The effect of levelling an image is demonstrated in the cross-sections in Figure 5.7. The cross-section in (a) shows height information prior to any levelling. Significant sample tilt can be seen in this cross-section and height information is uninterpretable. 3-point levelling was then performed on the entire image by selecting three known flat regions on the sample, i.e. where the sample substrate is visible. The software applies the levelling to the image with respect to the user defined points. The same line is examined in both cross-sections (a) and (b) shown in Figure 5.7. Height information can be interpreted and individual features are more clearly defined in cross-section (b) which derives from an image that has been levelled.

Removal of system background was then typically applied to topography images to eliminate anomalous curvature that is introduced to an image due to

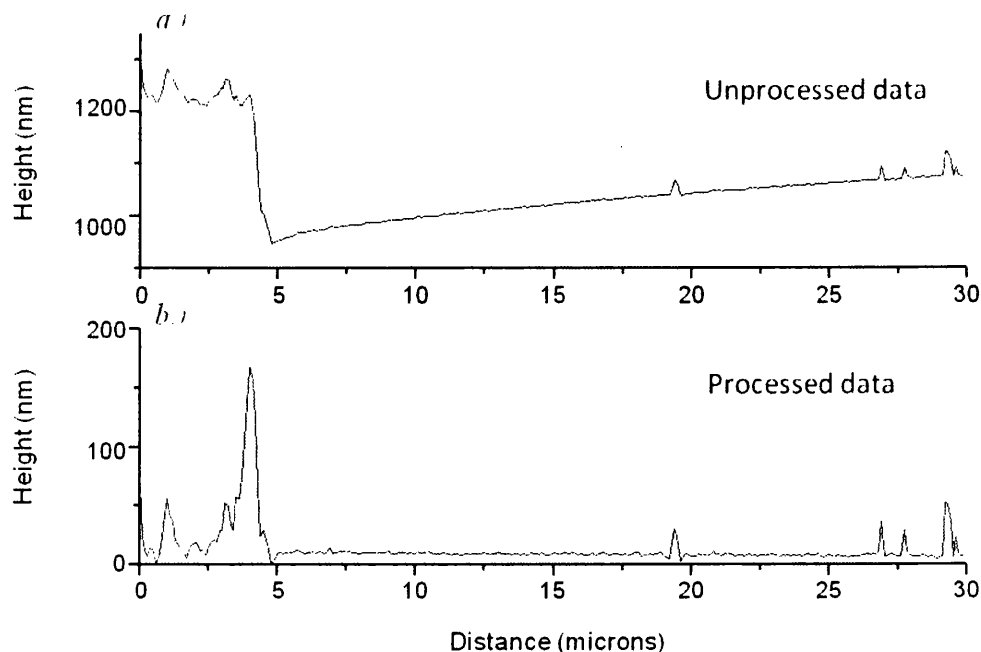


Figure 5.7: (a) A cross-section obtained from an image prior to correcting for sample tilt. (b) Cross-section obtained following levelling the image. The same lines are examined in both cross-sections (a) and (b).

scanner error. In order to further enhance the definition of the image, the contrast was adjusted using the software's histogram function. This enables the user to control the colour distribution over the height range of interest in the image and resolve finer features that may otherwise be masked due to a large height range. To enhance SNOM fluorescence images, the only function that was performed was adjustment of the image contrast using the histogram function.

5.4 Preparation of biological samples

5.4.1 Sample preparations

This section fully outlines the sample preparation methodologies employed during this study. The methods used to grow and sustain cells *in vitro* are described, as are the fixation procedures.

All steps of the immunofluorescence labelling protocols were optimised from the basic procedures described by the manufacturers; including permeabilisation

conditions, blocking steps, concentrations of reagents, incubation conditions and washing steps. The optimisation was completed for each cell line used within this study.

Cell Culture

Prostate epithelial cells, PNT2, and prostate adenocarcinoma cells, PC-3, were obtained from the European Collection of Cell Cultures. The cells were maintained in RPMI 1640 media supplemented with 10% fetal bovine serum, 1% L-Glutamine, 60 units/mL penicillin, and 60 $\mu\text{g}/\text{mL}$ streptomycin at 37 °C/5% CO_2 . Growth media was refreshed every other day, and the cells were sub-cultured when they reached approximately 80 % confluency.

Growth of cells on slides/coverslips and cell fixation

For optimisation purposes, cells were grown on sterile glass slides. For imaging, cells were grown on sterile 25 mm circular glass coverslips. The confluency of the cells was difficult to control. This can be altered by changing the concentration at which the cells are seeded or by changing the length of time that the cells are allowed to grow before fixing. To study adhesion mechanisms, cells need to be confluent enough such that cell-cell contact has occurred and mature contact sites have had time to form. Moreover, to study the role filopodia play in initiating adherens junction formation, their molecular make-up should be examined at various stages of cell-cell contact, including samples where initial cell-cell contact has yet to be established. The cells were fixed at room temperature using 3.7 – 4% ultra-pure methanol-free formaldehyde in PBS for 15 minutes, followed by three 5 minute washes in PBS/100 mM glycine and dehydrated through an ethanol series. Coverslips were stored at 4 °C until required for immunolabelling. Optimally, samples were imaged within 48 hours of preparation. Signs of degradation were often observed around a week after fixation/ labelling. Samples were subsequently discarded when degradation was observed during imaging.

5.4.2 Permeabilisation, fluorescent labelling and washing

For fluorescence labelling of fixed cells, the coverslips were rinsed with PBS to resuscitate the cells. All subsequent incubation periods utilised a simple, home-made humidity chamber at room temperature, unless otherwise stated. The humidity chamber minimises evaporation of labelling reagents and prevents subsequent concentration changes during incubations. Each incubation period was followed by three 5 minute washes in phosphate buffered saline (PBS) solution at room temperature, to remove unbound reagents unless otherwise stated. Concentrations were optimised for all labelling protocols. Protocols are summarised in the flowchart shown in Figure 5.8 which shows the general method for immunofluorescence labelling carried out in this thesis. Dual labelling is summarised in Figure 5.9.

Organic dyes for labelling E-cadherin in PNT2 cells

Cells were permeabilised with 0.1 % Triton-X for 10 minutes, rinsed three times for 5 minutes each in PBS and then incubated with signal enhancer (Image-iT FX signal enhancer, Invitrogen) for 30 minutes which helps to reduce background fluorescence that can arise due to nonspecific binding of secondary antibodies. Cells were rinsed three times in PBS for 2 minutes each time. E-cadherin primary antibody was then applied at a concentration of 18 $\mu\text{g}/\text{ml}$, diluted in 1 % BSA/PBS (rabbit polyclonal anti E-cadherin antibody) for 1 hour [2]. Coverslips were rinsed three times for 5 minutes in PBS. To label E-cadherin with Alexa Fluor 488 goat anti-rabbit secondary antibody conjugate, the coverslips were incubated with 2 $\mu\text{g}/\text{ml}$ for 2 hours [3]. The coverslips were rinsed three times for 5 minutes in PBS to remove excess unbound Alexa Fluor 488. To facilitate SNOM imaging, samples were additionally rinsed three times in water, dehydrated through an ethanol series and air-dried. Samples were stored at 4 °C.

General protocol for the immunofluorescence labelling of cells

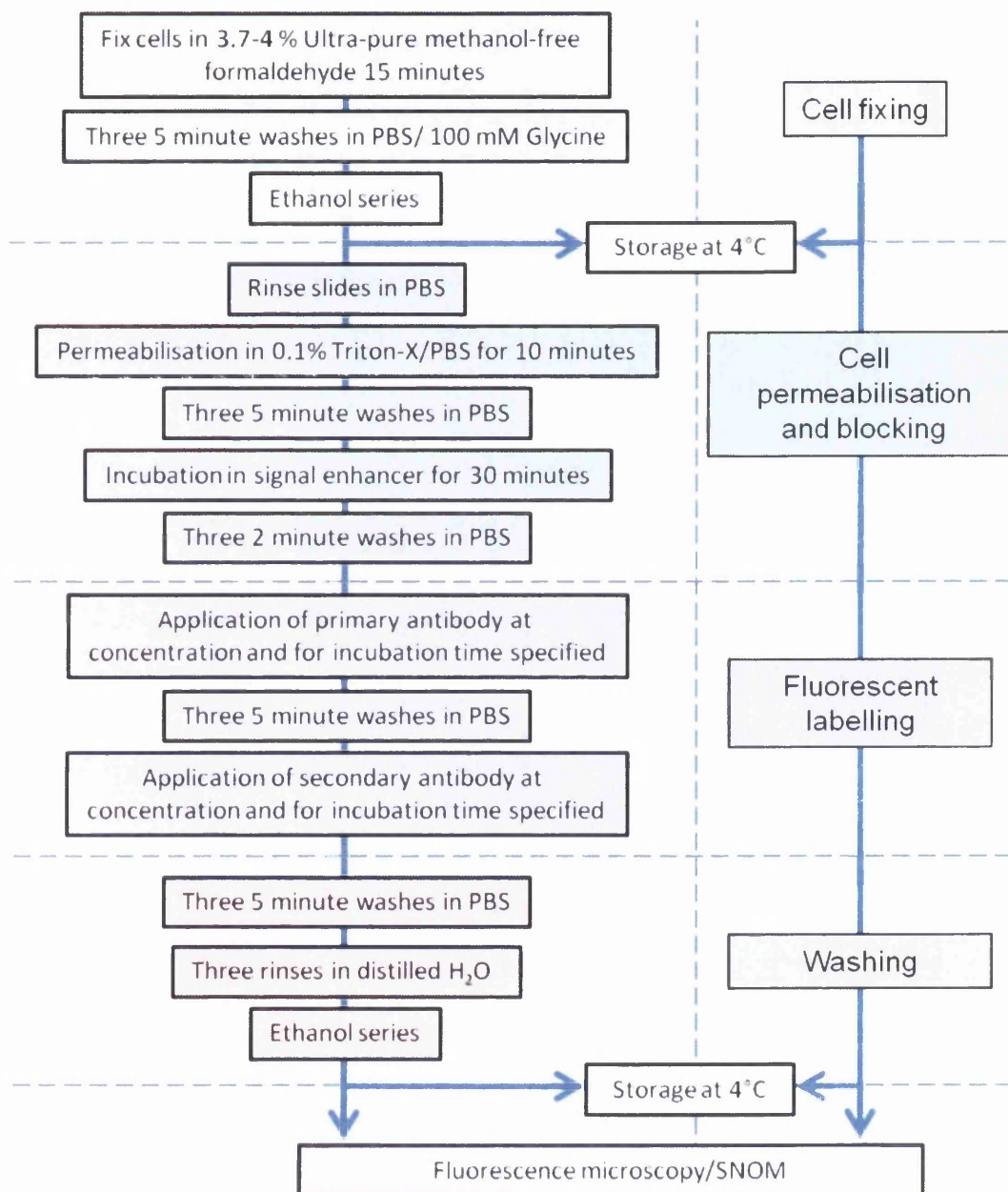


Figure 5.8: Schematic illustration showing general experimental protocol followed for fixing and immunofluorescent labelling of cells.

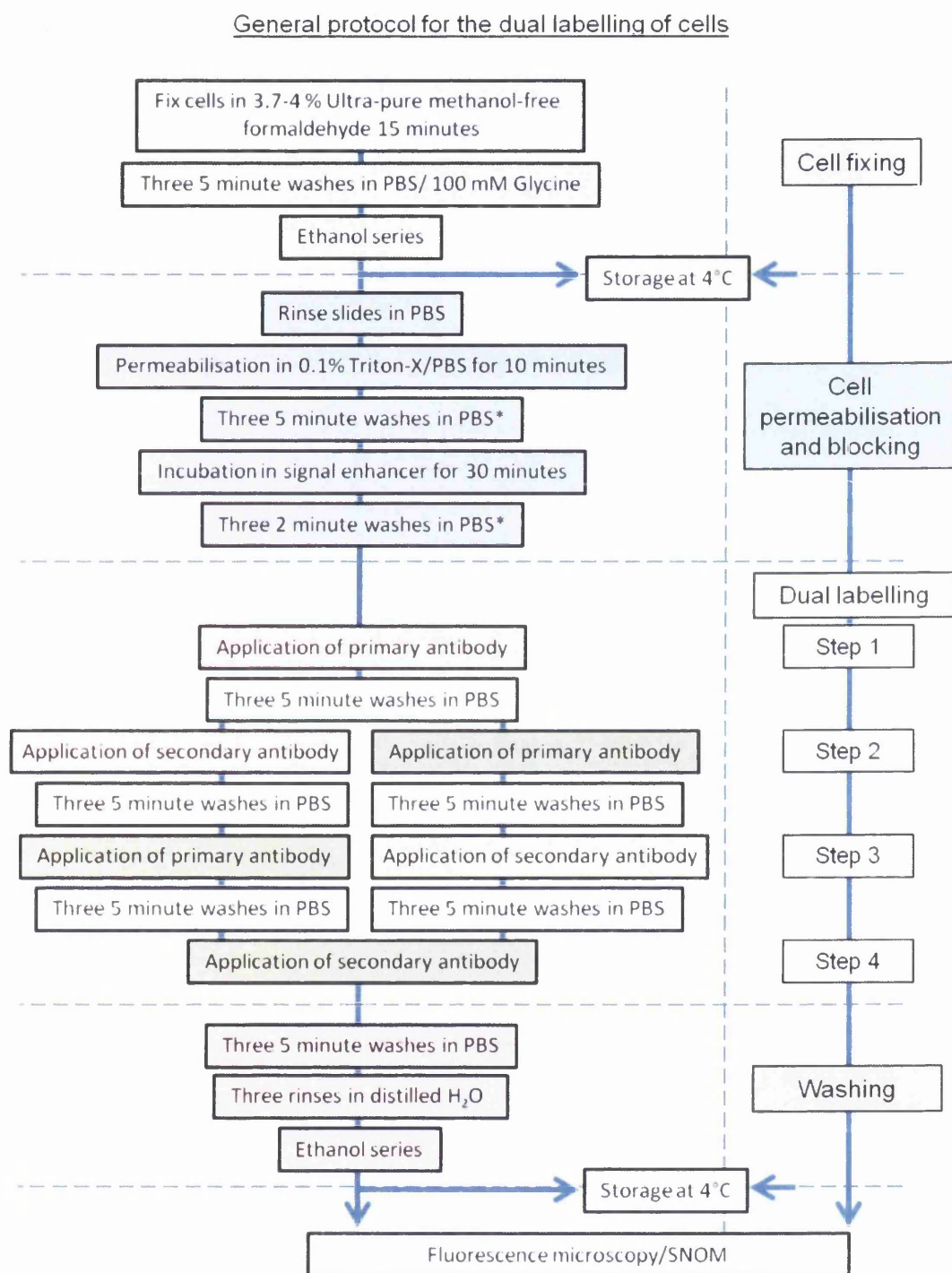


Figure 5.9: Schematic illustration showing generalised experimental protocol followed for the dual labelling of cells with quantum dots. * for PC-3 cells this stage is changed to three 5 minute PBS/100 mM glycine washes.

Quantum Dot labelling of cytoskeletal proteins in PNT2 cells

The protocol for labelling cytoskeletal proteins was optimised and provided by Doak *et al.* [4]. Following the fixation procedure coverslips were rinsed in PBS and permeabilised in 0.1 % Triton-X for 5 minutes. Three 5 minute washes in PBS were carried out then endogenous biotin was blocked using a Biotin blocking kit in accordance with the manufacturers' guidelines (Invitrogen). Cells were incubated in signal enhancer (Image-iT FX signal enhancer, Invitrogen) for 30 minutes and rinsed three times in PBS for 2 minutes each time. Cells were subsequently incubated with 2 μ M biotinylated phalloidin for 20 minutes [3], washed three times for 5 minutes in PBS and then incubated with 20 nM Qdot 655-Streptavidin conjugate for 30 minutes [3]. Excess unbound quantum dots were rinsed by three 5 minute washes in PBS and samples were dehydrated through an ethanol series before left to air dry. Samples were stored at 4 °C until required for imaging.

Quantum Dot labelling of Membrane proteins in PNT2 cells

This labelling procedure applies for the labelling of E-cadherin proteins OR ZO-1 proteins separately. The dual labelling protocol which labels both proteins on the same sample is described later in this chapter.

Coverslips were rinsed with PBS to resuscitate cells following fixation and subsequent storage. Cells were permeabilised with 0.1 % Triton-X for 10 minutes, washed three times for 5 minutes in PBS and then incubated with signal enhancer for 30 minutes. Cells were rinsed three times in PBS for 2 minutes each time.

This step is applicable only for quantum dot labelling of E-cadherin: Primary antibodies were applied at a concentration of 18 μ g/ml diluted in 1 % BSA/PBS (rabbit polyclonal anti E-cadherin antibody) [2]. Cells were incubated for 1 hour then rinsed three times for 5 minutes in PBS. Quantum dot conjugate (Qdot 605 goat F(ab')₂ anti-rabbit IgG or Qdot 525 goat F(ab')₂ anti-rabbit IgG) was applied to the coverslips at a concentration of 20 nM which were subsequently incubated for 1 hour [3].

This step is applicable only for quantum dot labelling of ZO-1: Primary antibodies were applied at a concentration of 19 μ g/ml diluted in PBS (ZO-1 mouse

monoclonal antibody) [3]. Cells were incubated for 2 hours at 37 °C then rinsed three times for 5 minutes in PBS. Quantum dot conjugate (Qdot 525 goat F(ab')₂ anti-mouse IgG conjugate or Qdot 655 goat F(ab')₂ anti-mouse IgG conjugate) was applied to the coverslips at a concentration of 20 nM which were subsequently incubated for 1 hour [3].

This step is applicable for the labelling of E-cadherin or ZO-1: Coverslips were rinsed three times for 5 minutes in PBS to remove excess unbound quantum dots. To facilitate SNOM imaging, samples were additionally rinsed three times in water, dehydrated through an ethanol series and air-dried. Samples were stored at 4 °C.

Quantum Dots for Multiplexing

Full details of the optimisation work carried out on the multiplexing protocols used to label PNT2 and PC-3 cells are provided in Chapter 7. This section gives details of the protocols which were successful for each cell line.

Multiplexing in PNT2 cells: Coverslips were rinsed with PBS to resuscitate cells following fixation and subsequent storage. Cells were permeabilised with 0.1 % Triton-X for 10 minutes, washed three times for 5 minutes in PBS and then incubated with signal enhancer for 30 minutes. Cells were rinsed three times in PBS for 2 minutes each time.

ZO-1 primary antibodies were applied at a concentration of 31 µg/ml diluted in PBS (ZO-1 mouse monoclonal antibody) [3]. Cells were incubated for 2 hours at 37 °C then rinsed three times for 5 minutes in PBS. Quantum dot conjugate (Qdot 525 goat F(ab')₂ anti-mouse IgG conjugate) was applied to the coverslips at a concentration of 30 nM which were subsequently incubated for 1 hour [3]. Coverslips were rinsed three times in PBS for 5 minutes each then E-cadherin primary antibodies were applied at a concentration of 18 µg/ml diluted in 1 % BSA/PBS (rabbit polyclonal anti E-cadherin antibody) [2]. Cells were incubated for 2 hours at 37 °C then rinsed three times for 5 minutes in PBS. Quantum dot conjugate (Qdot 605 goat F(ab')₂ anti-rabbit IgG) was applied to the coverslips

at a concentration of 20 nM which were subsequently incubated for 1 hour [3].

Coverslips were rinsed three times for 5 minutes in PBS to remove excess unbound quantum dots. To facilitate SNOM imaging, samples were additionally rinsed three times in water, dehydrated through an ethanol series and air-dried. Samples were stored at 4 °C.

Multiplexing in PC-3 cells: Coverslips were rinsed with PBS to resuscitate cells following fixation and subsequent storage. Cells were permeabilised with 0.1 % Triton-X for 10 minutes, washed three times for 5 minutes in PBS/100 mM glycine and then incubated with signal enhancer for 30 minutes. Cells were rinsed three times in PBS/100 mM glycine for 2 minutes each time.

E-cadherin primary antibodies were applied at a concentration of 18 µg/ml diluted in 1 % BSA/PBS (rabbit polyclonal anti E-cadherin antibody) [2]. Cells were incubated for 2 hours at 37 °C then rinsed three times for 5 minutes in PBS. Quantum dot conjugate (Qdot 605 goat F(ab')₂ anti-rabbit IgG) was applied to the coverslips at a concentration of 20 nM which were subsequently incubated for 1 hour [3]. Coverslips were rinsed three times in PBS for 5 minutes each then ZO-1 primary antibodies were applied at a concentration of 31 µg/ml diluted in PBS (ZO-1 mouse monoclonal antibody) [3]. Cells were incubated for 2 hours at 37 °C then rinsed three times for 5 minutes in PBS. Quantum dot conjugate (Qdot 525 goat F(ab')₂ anti-mouse IgG conjugate) was applied to the coverslips at a concentration of 20 nM which were subsequently incubated for 1 hour [3].

Coverslips were rinsed three times for 5 minutes in PBS to remove excess unbound quantum dots. To facilitate SNOM imaging, samples were additionally rinsed three times in water, dehydrated through an ethanol series and air-dried. Samples were stored at 4 °C.

5.5 Summary

This chapter has described the instrumental set-ups required to examine immunofluorescently labelled cells with fluorescence microscopy, SNOM and im-

portant developments required when using both techniques to study the same sample. Methodologies are provided which detail the preparation of samples to facilitate both microscopy techniques. Furthermore, a dual labelling protocol which utilises quantum dots is described. These protocols are in themselves complete but provide a platform for other researchers to adapt and develop such that other proteins or cells may be studied through labelling with quantum dots. In particular, the protocols have addressed important preparation aspects which may be relevant to other SPM techniques. The reader is referred to Chapter 7, which discusses various aspects of sample preparation that require attention when developing dual labelling protocols.

Bibliography

- [1] M. D. Holton. *Near-field spectroscopy of colloidal quantum dots and vertical cavity surface emitting lasers*. PhD thesis, Swansea University, 2007.
- [2] Abcam Plc. Immunocytochemistry general procedures. <http://www.abcam.com/>.
- [3] Invitrogen. Immunocytochemistry general procedures. <http://www.invitrogen.com>.
- [4] S. H. Doak, D. Rogers, B. Jones, L. Francis, R. S. Conlan, and C. Wright. High-resolution imaging using a novel atomic force microscope and confocal laser scanning microscope hybrid instrument: essential sample preparation aspects. *Histochem. Cell. Biol.*, 130(5):909–916, 2008.

Chapter 6

Results: SNOM imaging of biological materials

6.1 Introduction

In conventional optical techniques much information is lost because of the limitations in spatial resolution. SNOM has the ability to overcome the diffraction limit by exploiting the properties of evanescent waves and utilising a nanoscale light source to achieve nanoscale resolution.

In this study, SNOM has been applied to simultaneously acquire high-resolution fluorescence and shear-force atomic microscopy images of biological samples. The acquisition of both topographic and fluorescent images yields vital information about the molecular make-up of cellular components.

In order to achieve high-resolution imaging, sample preparation is vital. This chapter is focussed on the development of a standardised methodology to provide reproducible and robust samples with well preserved structural detail and low background fluorescence.

The prostate epithelial cell line PNT2 has been used as the basis for all sample preparations. Fluorescent labelling of two protein systems has been explored: The targeting of membrane proteins and cytoskeletal proteins has been carried out. Furthermore, two fluorescent labelling agents have been tested. Comparison of Alexa Fluor 488 and semiconductor quantum dots for use in immunofluores-

cence labelling revealed quantum dots demonstrate significantly enhanced photostability and higher quantum yield. Ultimately quantum dots proved to be the preferred choice of fluorescent tag for biological investigations using SNOM.

6.2 Development of fluorescent biological samples

6.2.1 Sample requirements

The overall objective of this work was to take advantage of the benefits SNOM has over conventional microscopy techniques when applied to the study of biological materials. Concurrent high resolution topography and fluorescence images can be obtained (the latter of which is not restricted by the diffraction limit) to facilitate functional analysis of specific cellular components. Initial feasibility tests were completed to assess samples for SNOM investigation. Topography images of the prostate epithelial cell line PNT2 were obtained to determine the suitability of the cell line.

As demonstrated by the typical SNOM topography images shown in Figure 6.1, numerous cellular components can be resolved including the nuclear region (circled in Figure 6.1(a) and (c)) and lamellipodia (labelled L in Figure 6.1(b)), which are actin-based protrusions commonly observed at the leading edge of motile cells [1]. The lamellipodia observed in Figure 6.1(b) are present in the intercellular region between two cells initiating contact, with numerous nano-sized filopodia (indicated by arrows) extending beyond the lamellipodia periphery. Individual filopodia with diameters ranging between approximately 300 – 500 nm, can be seen to extend up to 10 μm across the intercellular area and are highly directed towards the opposing cell. Furthermore, filopodia from two cells in close proximity appear to form a network across the cell-cell boundary and interact with each other as seen in Figures 6.1(c) - (e). The filopodia are examined in closer detail in Figure 6.1(f), which shows a 3-dimensional representation. As first reported by Doak *et al.* [2], multiple dimples along their surface are detected,

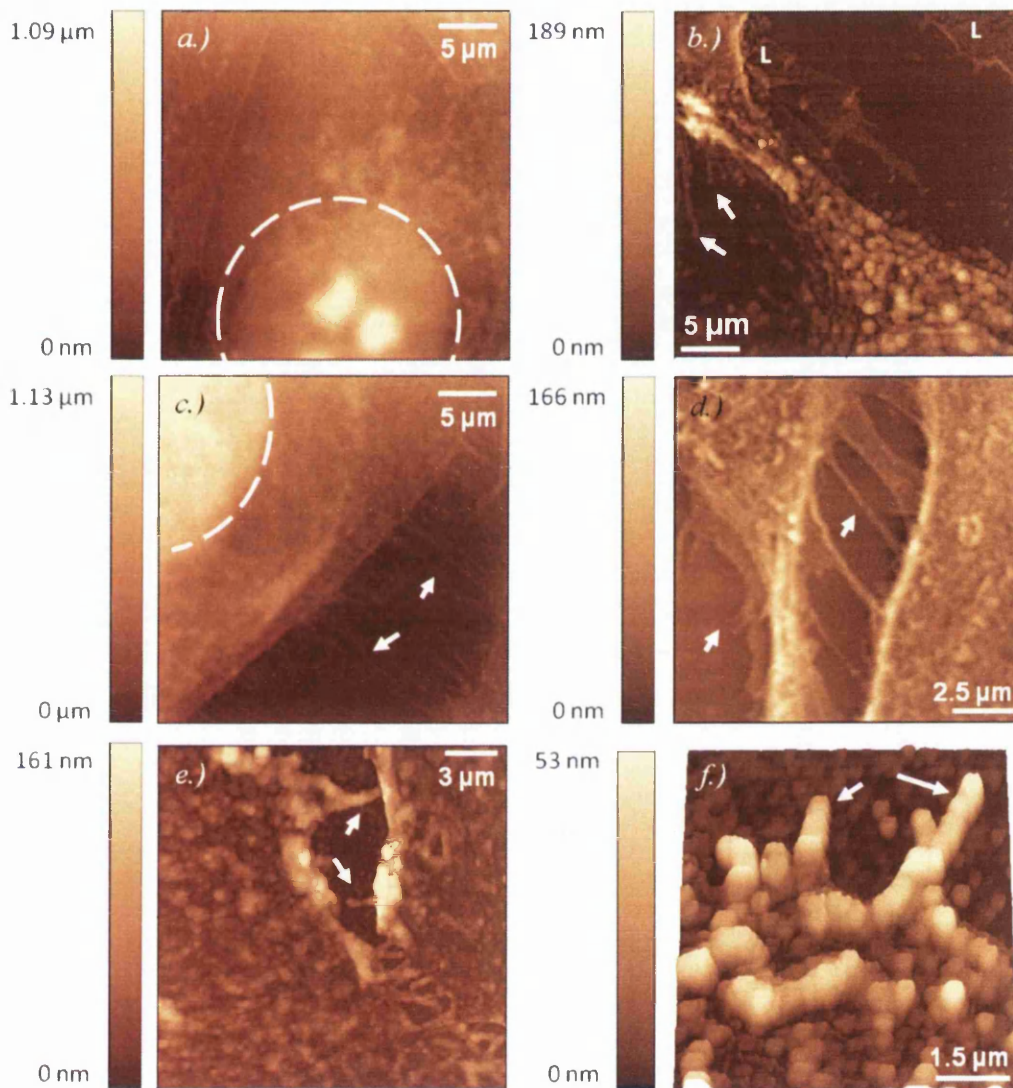


Figure 6.1: Typical SNOM topography images of the cell line PNT2. Various features can be resolved including the nucleus (circled in (a) and (c)), lamellipodia (indicated by L in (b)) and numerous filopodia (indicated by arrows in (b) - (f)). 3 dimensional representation (f) of filopodia reveals “quilted” appearance. Scale bars to the left of each image represent height of topographical features. Scans (a), (b) and (c) are $(30 \mu\text{m})^2$, (d) is $(14 \mu\text{m})^2$, (e) is $(20 \mu\text{m})^2$ and (d) $(7 \mu\text{m})^2$.

which result in a “quilted” appearance.

Narrow topographic ridges can be seen near the outer region of the cells in Figures 6.1(a) and (d), which most likely represent cytoskeletal microfilaments present beneath the surface [2]. These become visible as the membrane collapses down onto the underlying structures, after the cells are dried through desiccation. The highest point of the cells was observed over the nucleus and measurements gave a wide range of values, from approximately $0.5 - 2.7 \mu\text{m}$. This is likely to be due to the extent of confluency that the cells had achieved at the time of imaging. The overall size of the cells exceed the maximum scan range permitted by the SNOM scanning stage ($30 \mu\text{m}$)², thus it was possible to obtain only partial images of any cell each time a scan was executed. Although multiple scans were obtained sequentially for more a complete picture to be built up, it was common to observe only part of the nucleus in a particular scan (as in Figure 6.1(c)). Or if the nucleus was fully imaged, then the cell of interest would often span the entire area of the image with no substrate visible for use as a zero-point when measuring the overall height (as in Figure 6.1(a)). Consequently, there were a limited number of suitable topography images to determine the height of these cells.

This preliminary data confirms that PNT2 cells are a suitable system for further investigations with SNOM. As will be discussed in the following section, fluorescent labelling of proteins present in this cell line will be studied.

6.2.2 Organic labelling of membrane proteins

Further work on developing biological samples involved labelling the adhesion protein E-cadherin in prostate epithelial PNT2 cells with the organic fluorophore Alexa Fluor 488. Optimisation of the protocol was completed with the use of a fluorescence microscope. However, the fragility of the SNOM tip and the dependence of optical resolution on aperture size warranted additional washes to ensure the complete removal of any salt residues remaining on the surface following the labelling procedure. This eliminated any surface debris that may otherwise have come into contact with the tip during scanning. These additional washes also

help to ensure thorough rinsing of any unbound labelling agents and thus help improve the signal-to-noise image contrast. However, it is important to ensure that they do not affect hybridisation and inadvertently remove specifically bound labels. Consequently, before imaging with SNOM all samples were observed with a fluorescence microscope to verify successful labelling and to ensure the fluorescent probes had hybridised specifically to the target protein. Figure 6.2 shows a typical fluorescence microscopy image of PNT2 cells labelled against E-cadherin with Alexa Fluor 488. Specific filters are used to select the required excitation wavelength from a mercury lamp and to illuminate the sample. The resulting signal is passed through an emission filter to separate the fluorescence from the illumination source. The image is false colour and uses a black to green scale, such that the brightest green pixels represent regions where the highest intensity fluorescence was recorded.

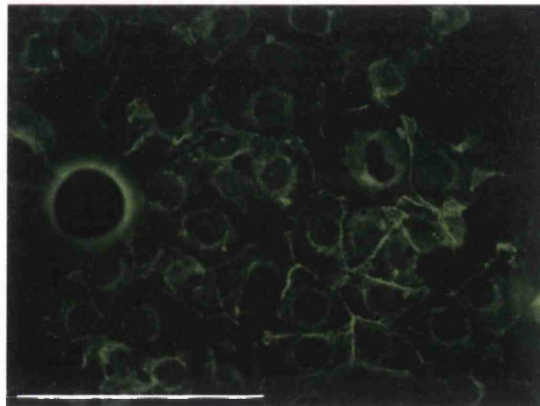


Figure 6.2: *Fluorescence microscopy image of the adhesion protein E-cadherin labelled with Alexa Fluor 488 in PNT2 cells. Scale bar represents approximately 100 μm .*

Samples were imaged with SNOM using an integration time of 20 ms per pixel. Figure 6.3 shows a typical SNOM acquisition of two cells at the initial stages of cell-cell contact. The vertical scale bars shown in (a) and (b) are representative of the height of features, and the intensity of the fluorescence recorded by the APD detector respectively.

The topographic structure is shown in Figure 6.3(a), with two prostate epithelial cells in close proximity. The structure is well preserved and filopodia

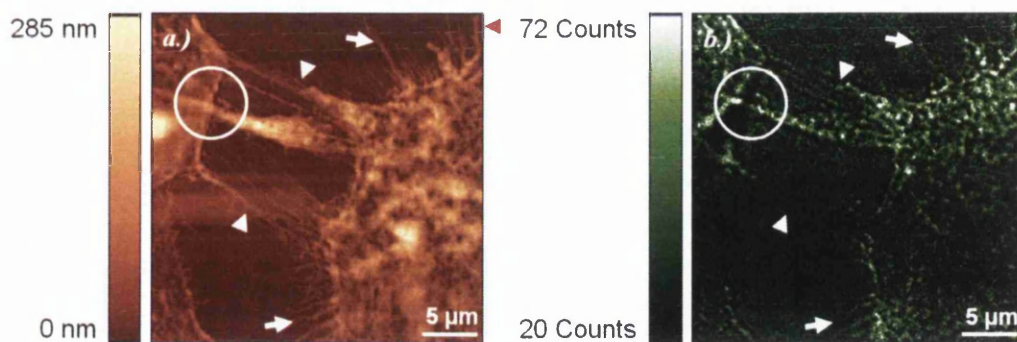


Figure 6.3: *Simultaneously acquired $(30 \mu\text{m})^2$ topographic (a) and fluorescent (b) SNOM images of two PNT2 cells initiating cell-cell contact. Cells are labelled with Alexa Fluor 488 to identify E-cadherin along cell boundaries and extending throughout filopodia. Circled region identifies a punctate E-cadherin cluster. Filopodia are clearly seen (arrows), some of which are observed interacting (arrowheads).*

from each cell can clearly be seen to extend across the intercellular region (as indicated by arrows). Figure 6.4 shows an example of cross section data from line measurements performed on the image shown in Figure 6.3(a). The line analysed is indicated by a red arrowhead on the right of the figure and analysis was carried out following minimal image processing, as discussed in Chapter 5. Measurements show that dimensions of individual filopodia vary widely but typically possess diameters ranging from approximately 110 – 270 nm, with heights up to 40 nm. Furthermore, these nano-structures were generally found to extend approximately 4 – 5 μm from their originating lamellipodium, while some are observed to protrude over 10 μm into the intercellular space. These observations concur with data published by Doak [2] where very fine filopodia (100 – 150 nm in diameter) were found in the intercellular region between two closely positioned PNT2 cells. Figure 6.3(a) also indicates opposing filopodia making contact which appear to interdigitate (arrowheads) and eventually adhere to the neighbouring cell (circled region). This initial adherence provides an anchorage which is likely to support and encourage the establishment of further contact sites.

The simultaneously acquired fluorescence image shown in Figure 6.3(b) is presented with a scale bar which displays the data such that the average signal-to-background noise is clear. Thus the signal-to-noise ratio of Figure 6.3(b) is

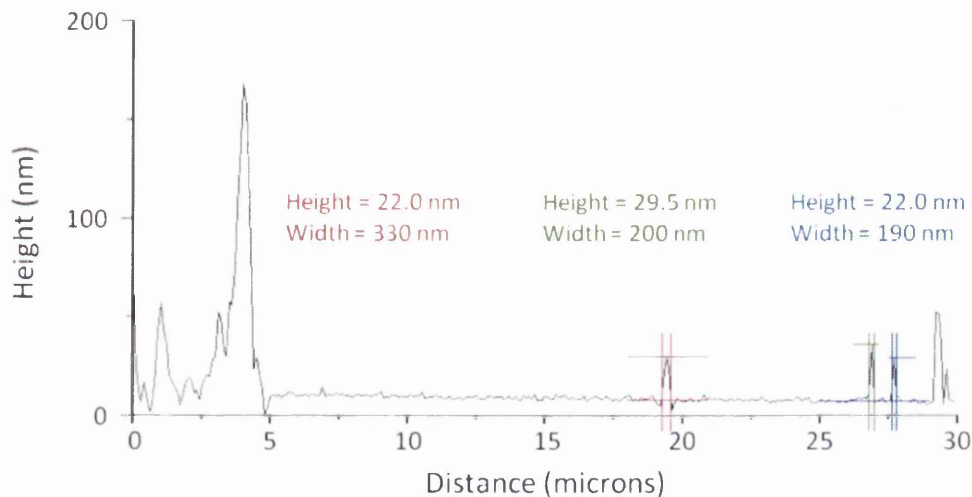


Figure 6.4: Measurements of height and diameter of filopodia. Cross-section taken from line indicated by red arrow on Figure 6.3(a).

~ 3.6. Comparison of the topography (Figure 6.3(a)) with the simultaneously acquired fluorescence image (Figure 6.3(b)) reveals the presence of Alexa Fluor 488 along the cell boundaries and extending throughout the filopodia. Due to the targeted labelling employed, one can conclude that the Alexa Fluor 488 signal is indicating the presence of E-cadherin in these two regions. A punctate E-cadherin cluster is highlighted within the circled region and corresponds to filopodia that have adhered to the neighbouring cell.

Current literature suggests filopodia have a functional role not only in motility and guidance during cell migration [3] but also in cell-cell adhesion [4]. In a study of epidermal keratinocytes, Vasioukhin *et al.* [4] reported that filopodia embed into opposing cells. E-cadherin was found to cluster at the tips of embedded filopodia forming a row of puncta. It was reported that this anchorage promotes the establishment of additional functional contact sites and filopodia physically pull the two cells together. The result presented in Figure 6.3 supports these previous articles via a high resolution SNOM image clearly showing the targeted immunofluorescence signals from E-cadherin present at these cell-cell contact sites and also within the filopodia.

Figure 6.5 shows a further SNOM acquisition of PNT2 cells. As before the

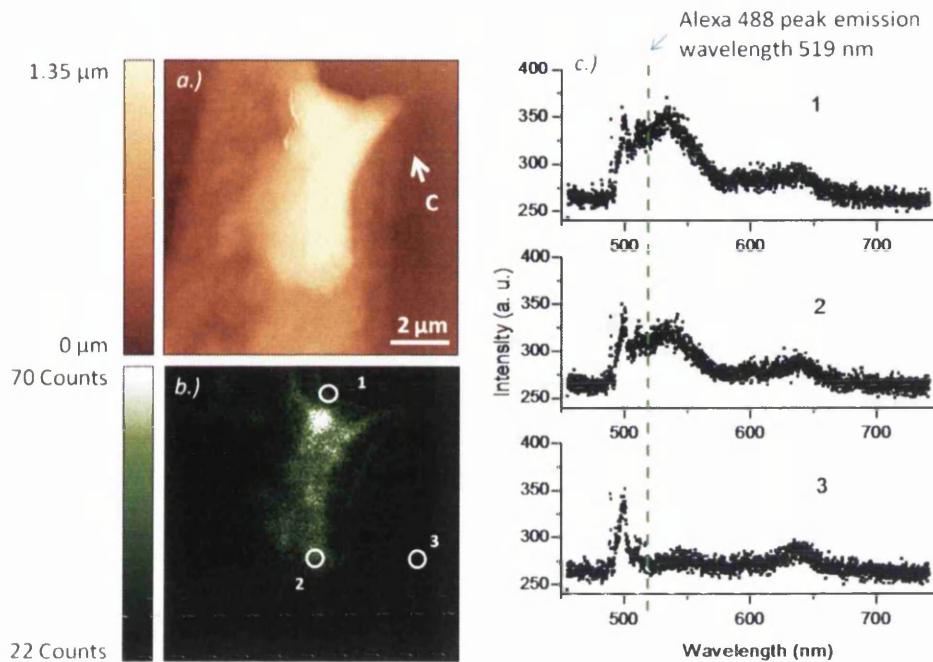


Figure 6.5: $(30 \mu\text{m})^2$ SNOM acquisitions of a PNT2 cell showing (a) topography and (b) optical images. Optical image shows E-cadherin location, revealed by immunofluorescence labelling with Alexa Fluor 488. (c) Point spectroscopy corresponding to regions highlighted in image (b).

location of E-cadherin is revealed via specific immunofluorescence labelling using Alexa Fluor 488. Although the quality of the topography image shown in Figure 6.5(a) is inferior to that in Figure 6.3, the cell boundary can clearly be observed (indicated by C). The complimentary optical image shown in Figure 6.5(b), indicates E-cadherin is found along the cell boundary as previously observed.

High counts are also recorded over the higher topographic regions. Point spectroscopy was carried out to determine the origin of these counts and eliminate the possibility that they are an artefact of the high features. Point spectroscopy was executed once SNOM imaging was complete. The tip was positioned above the sample at user specified points and the resulting spectra were collected.

Figure 6.5(c) shows three spectra collected at the points highlighted (within circled regions on Figure 6.5(b)). The collection time used for all spectra was 5 minutes. All three spectra reveal sharp peaks at around 500 nm, these are due to the laser light bleeding through the high pass filter. The peak emission of

Alexa Fluor 488 is indicated by the dashed line at 519 nm on Figure 6.5(c) as specified by the manufacturers [5]. A broad peak at the slightly higher wavelength of 537 nm can be seen on spectra 1 and 2 which is attributed to fluorescence from bound Alexa Fluor 488 fluorophores. The spectra confirm the presence of Alexa Fluor 488 at region 2 (indicated on Figure 6.5(b)). This verifies that the large number of counts recorded over the high topographic feature are real signals originating from bound (albeit non-specifically) Alexa Fluor 488 to the cell membrane. Furthermore, examination of spectra 3 reveals no such peak is observed at 537 nm indicating no Alexa Fluor 488 fluorophores are present in this region of the sample. This is as expected since spectra 3 was collected above a region adjacent to the cell (in the intercellular space).

The success of obtaining high-resolution, concurrent topography and optical images obtained using SNOM has enabled a functional analysis of nanometer-sized, sub-cellular components. However, rapid photobleaching of the already low fluorescence levels inhibited prolonged examination of regions of interest. Thus, to facilitate more extensive SNOM studies it was desirable to employ a brighter and more robust fluorescent label that could withstand greater exposure to illumination.

6.2.3 Quantum dot labelling of cytoskeletal proteins

The low levels of fluorescence observed when examining samples labelled with the organic dye Alexa Fluor 488, coupled with the rapid bleaching when successive images were obtained of the same sample, prompted investigations into the use of semi-conductor quantum dots as an alternative fluorescent tag.

In recent years, quantum dots have been increasingly utilised in biological applications. Their many benefits over conventional fluorophores has been discussed in detail in section (2.5.4). Quantum dots are notably more photostable and substantially brighter owing to their high quantum yield [6, 7]. Therefore they afford a far more robust sample system which, in turn, facilitates the repeated scanning of regions of particular interest.

F-actin filaments collectively form the cytoskeleton which acts as the cell's

structural support network and are abundant in nearly all eukaryotic cells. Thus these cellular components were chosen as the target for labelling with quantum dots due to their relatively high abundance which ultimately facilitates the detection of fluorescent signals. Quantum dot-streptavidin conjugates were used to indirectly target F-actin microfilaments of PNT2 cells and investigate their distribution within the cytoplasm. The toxin phalloidin has a high affinity to F-actin: This was exploited in the labelling process by using phalloidin-biotin conjugates to specifically target F-actin filaments. In turn, the biotin molecules have a high affinity to streptavidin. Thus to complete the labelling process, quantum dot-streptavidin conjugates were utilised to specifically target the biotin molecules. The phalloidin-biotin-streptavidin labelling mechanism is routinely used in the fluorescent labelling of F-actin. Furthermore, this mechanism has been utilised by other researchers to label F-actin filaments of other cell lines with quantum dots [6, 8].

Figure 6.6 shows a PNT2 cell labelled with quantum dots of emission wavelength 655 nm to reveal the presence of F-actin within the cytoplasm of cells. The integration time of the SNOM optical images is 20 ms. A single cell can almost fully be visualised in topography image (a). The nucleus can clearly be distinguished (indicated by N) and was found to cover an area which measured approximately $200 \mu\text{m}^2$. The simultaneously acquired fluorescent image is shown in (b). The scale bar presented with Figure 6.6(b) reveals a signal-to-noise ratio of ~ 11 , far superior to the signal-to-noise levels achieved through fluorescent labelling with Alexa Fluor 488.

An example of labelled F-actin taken from Wu *et al.* [6] is shown in Figure 6.7. Wu *et al.* examined mouse fibroblast cells which were labelled with 535 nm (green) emitting quantum dots to show F-actin filaments. The epifluorescence image clearly shows the filamentous nature of F-actin (green), while cells were counter-stained with Hoechst 33342 dye to show nuclei (blue).

Although the study by Wu and co-workers [6] was carried out on different cells to those examined in this investigation, F-actin filaments are inherent to most eukaryotic cells. However the results shown in Figure 6.6 do not correlate with

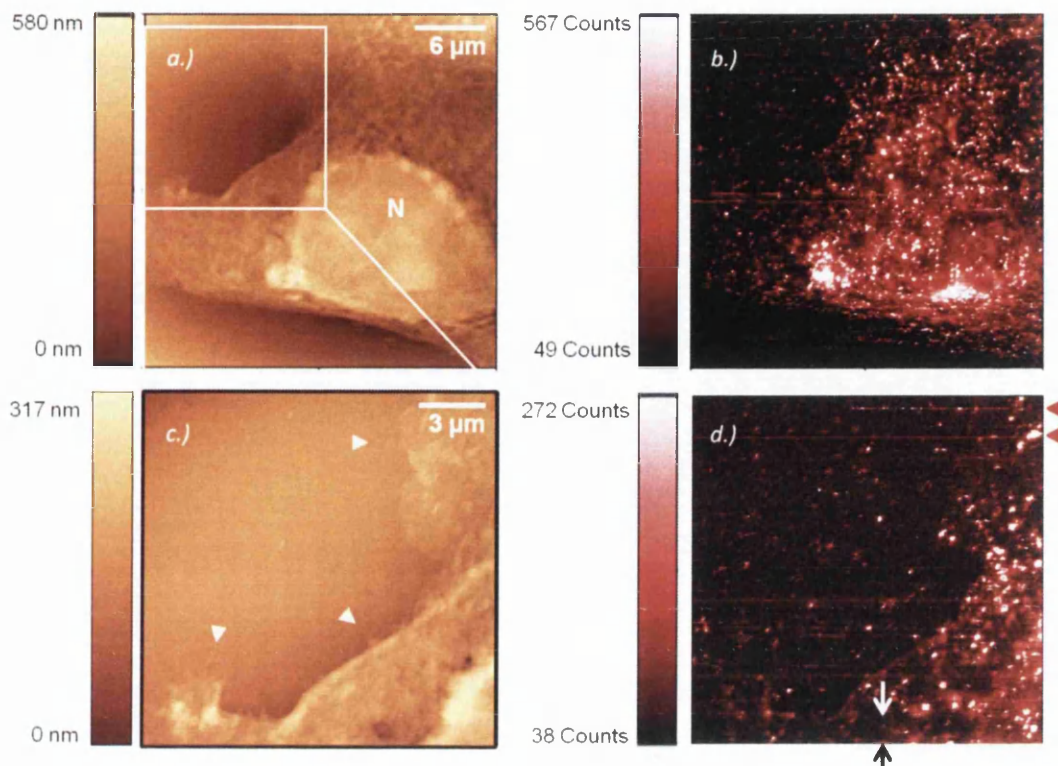


Figure 6.6: SNOM acquisitions of PNT2 cells fluorescently labelled with red quantum dots to show the distribution of F-actin within the cytoplasm. $(30 \mu\text{m})^2$ topography (a) and corresponding fluorescent images (b). Boxed region in (a) analysed at higher resolution to generate $(16 \mu\text{m})^2$ topography (c) and fluorescent images (d). N represents nucleus, white arrowheads indicate filopodia and red arrowheads indicate lines of high intensity fluorescence corresponding to active quantum dot attached to SNOM tip.

those observed by Wu *et al.* [6]. While there is some fluorescence corresponding to the cytoplasmic region of the cell, high counts are recorded over the nuclear region which is likely to correspond to heavy non-specific staining.

The boxed region in Figure 6.6(a) was sequentially scanned to reveal the structure at higher resolution and generate image (c). A small number of filopodia are resolved and are observed to protrude from the lamellipodia and the cell edge (indicated by white arrowheads on Figure 6.6(c)). These filopodia were measured to extend up to $1.4 \mu\text{m}$ into the intercellular space. Although this extension is not as far as that observed in Figure 6.3, this is most likely explained by the time at which fixation was carried out during the formation of filopodia.

The signal-to-noise ratio of the complimentary fluorescence image shown in

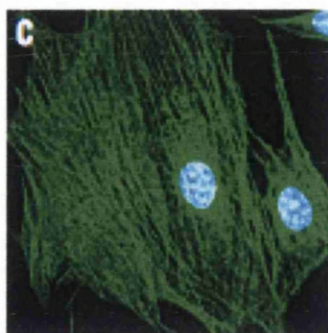


Figure 6.7: *Epifluorescence image of mouse fibroblast cells stained with quantum dots to reveal F-actin filaments within the cytoplasm (green). Nuclei counter-stained with Hoechst 33342 blue dye (blue). Adapted from [6].*

Figure 6.6(d) is ~ 7 . Examination of this image reveals multiple horizontal stripes of increased fluorescence intensity (indicated by red arrowheads in Figure 6.6(d)). However, there is no artefact in the corresponding topography image. The intermittency of these features are indicative that an individual quantum dot has become attached to the apex of the tip during scanning. This blinking phenomena is a characteristic signature of single quantum dots. This streaking effect due to the blinking of a single dot was observed by Sonnefraud *et al.* [9] during SNOM investigations of quantum dots embedded in a polymer matrix. These are also observed in Figure 6.6(b), but to a lesser extent.

Figure 6.8 demonstrates the high optical resolutions achievable when SNOM is employed to examine samples. The cross sections shown indicate the smallest fluorescent features are approximately 60 ± 1 nm in diameter. The feature is indicated by arrows on Figure 6.6(d) and was analysed in the vertical and horizontal directions (cross sections (a) and (b) respectively). The ability to resolve these nano-scale optical features is indicative of a high quality SNOM probe with a small aperture size. Thus, the larger fluorescent features observed in Figures 6.6(b) and (d) are most likely to be due to a cluster of quantum dots and not because of poor optical resolution.

The advantages afforded by quantum dot labelling are exemplified by the results shown in Figure 6.6. The quality of the fluorescence signals are significantly

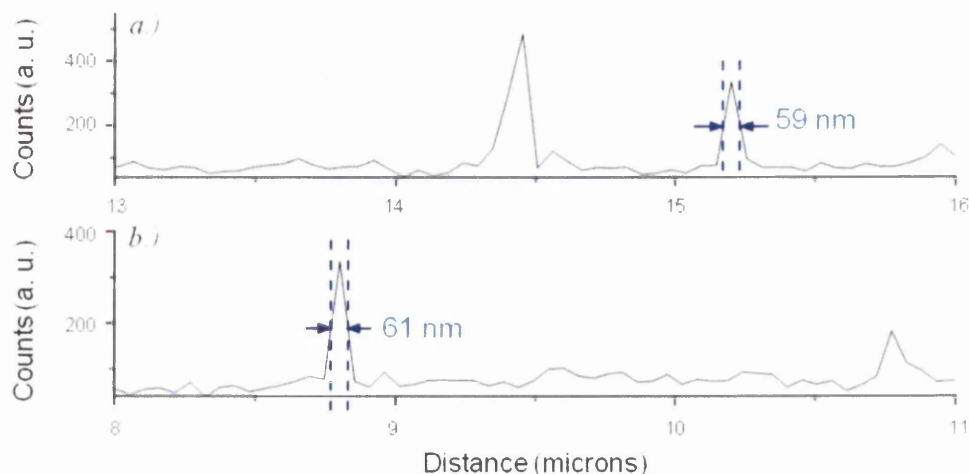


Figure 6.8: Cross sections showing optical resolution of 60 ± 1 nm from a single fluorescent feature measured (a) vertically and (b) horizontally across the feature.

enhanced when quantum dot labels are employed in place of Alexa Fluor 488 fluorophores. Superior signal-to-noise levels are achieved and quantum dots display enhanced photostability when regions are repeatedly examined (See Appendix 8.4 for data demonstrating inferior Alexa Fluor 488 photostability). Their use has provided samples that can be examined more thoroughly via repeated scanning before significant fading occurs.

However, the results of fluorescent labelling and subsequent imaging of F-actin distribution were not as expected and high levels of non-specific labelling over the nuclear region were observed. In order to realise the high-resolution optical imaging capabilities of SNOM, an optical fibre with sub-wavelength aperture is required to illuminate the sample. A consequence of using such a small light source however is that the illumination depth is limited and fluorescence originating from the surface of the sample will be recorded with higher resolution than fluorescence from within a sample. Thus it is possible that labelling of F-actin was specific, but that this was masked by the heavy non-specific labelling on the cell's surface.

For this reason, it was decided to pursue quantum dot labelling of the membrane protein E-cadherin. Examination of E-cadherin using SNOM was demonstrated in Figure 6.3: As such investigations involving E-cadherin have the pote-

nial to be extended to other cell lines and answer questions of biological importance.

6.3 Quantum dot labelling of E-cadherin

Following the investigations discussed in the previous section, the decision was made to proceed by labelling PNT2 cells with quantum dots to study the expression and function of the adhesion protein E-cadherin in further detail. This was achieved by looking at the interactions of filopodia and E-cadherin and their role in establishing adherens junctions. By studying the dynamics of filopodia and the location of E-cadherin at various stages of cell-cell contact, a deeper understanding of the mechanics of cell adhesion can be developed.

6.3.1 Development of methodology

Prior to imaging with SNOM all samples were examined with a fluorescent microscope to confirm staining had been successful. Thus, the staining methodology had to be developed to facilitate both imaging techniques.

High levels of background fluorescence were often observed due to quantum dots binding non-specifically on, or within the cell, and to the substrate. In an attempt to reduce the level of background signal, a series of PBS/Glycine washes were introduced after fixation of the cells. Aldehyde based fixatives work by reacting with and cross-linking proteins in order to preserve the cellular structure. However, this generates many tissue-bound free aldehyde groups which combine with any amino groups, including those present in antibodies used for fluorescent staining [10]. This results in antibodies that are highly specific to the antigen of interest, binding to other sites on the surface. The purpose of introducing the glycine was to block these free aldehyde groups by reduction of -CHO groups to -OH. The extent of fixative derived background fluorescence was further reduced by employing ultra-pure, methanol-free formaldehyde instead of paraformaldehyde. This is demonstrated in Figure 6.9 where samples fixed with ultra-pure methanol-free formaldehyde (Figure 6.9(a)) are compared with paraformaldehyde

hyde fixed samples (Figure 6.9(b)). The quality of the fluorescent labelling is enhanced when the ultra-pure methanol-free formaldehyde was used as the fixative. Paraformaldehyde contains methanol which causes protein clumping. This can affect structural preservation and the quality of the fluorescent signals observed from samples fixed with paraformaldehyde.

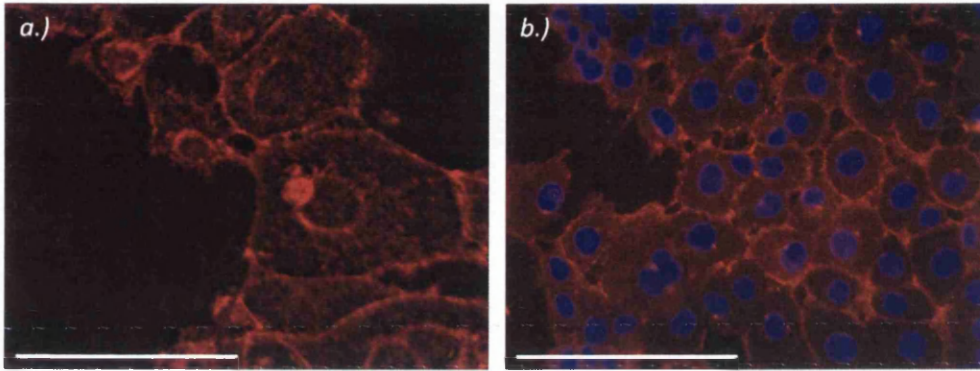


Figure 6.9: *Fluorescence microscopy images of PNT2 cells, labelled with red quantum dots. Comparison of fixatives show (a) reduced levels of non-specific staining over the cell membrane on samples fixed with ultra-pure methanol-free formaldehyde, compared with (b) where cells were fixed with paraformaldehyde fixed cells. Note; sample (b) counter-stained with DAPI (blue overlay) to reveal nucleus. Scale bars represent approximately 100 μm .*

6.3.2 Functional analysis of E-cadherin in confluent PNT2 samples

E-cadherin molecules in PNT2 cells were targeted using quantum dot conjugates with emission wavelength 605 nm. Core-shell CdSe/ZnS quantum dots coupled to a secondary antibody were utilised, which in turn bind specifically to E-cadherin via an intermediate primary antibody. The result of this process can be seen in the fluorescence microscopy image (Figure 6.10) which was acquired prior to analysis using SNOM. Fluorescence microscopy imaging revealed that cells are highly compact. Through targeted immunofluorescence labelling, E-cadherin is consistently observed at sites of cell-cell contact and in the perinuclear region.

The subsequent SNOM acquisitions can be seen in Figure 6.11. The integra-

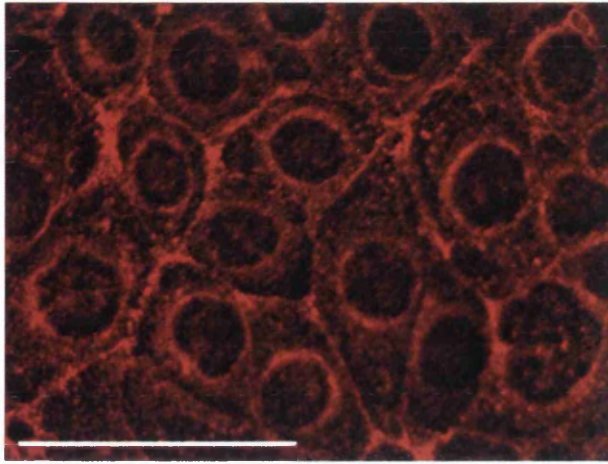


Figure 6.10: *Confluent PNT2 cells specifically labelled with red quantum dots to reveal E-cadherin presence at sites of cell-cell contact and also around the nucleus. Scale bar represents approximately 100 μm .*

tion time used for the SNOM fluorescence images (b) and (d) was 20 ms, which yields signal-to-noise ratios of ~ 8 and 10 respectively. As can be seen in the topography images (a) and (c), the cells are far more confluent than was observed in (Figure 6.3). Cell-cell contact has been fully established and the cells are much more densely packed and compact. Individual filopodia now cannot be differentiated and the architecture at the cell boundaries (indicated by C) is dissimilar to that observed in Figure 6.3. Multiple distinctive ridges can be seen to run along the site of contact. Furthermore the nucleus can clearly be distinguished in both images (indicated by N).

Vasioukhin *et al.* [4] demonstrated that upon establishing contact, filopodia from opposing cells physically draw them together. As the seal between opposing cells is established, filopodia regress via actin depolymerisation and the double row of E-cadherin puncta at the tips of adhered filopodia closes to form a single row.

The simultaneously acquired fluorescent response from quantum dot labelled cells (Figures 6.11(b) and (d)) demonstrates direct agreement with this study. The scans show a row of fluorescence, revealing E-cadherin is localised in areas corresponding to cell-cell contact (indicated by C on Figures 6.11(b) and (d)). E-cadherin is also present in the perinuclear region (nucleus indicated by N).

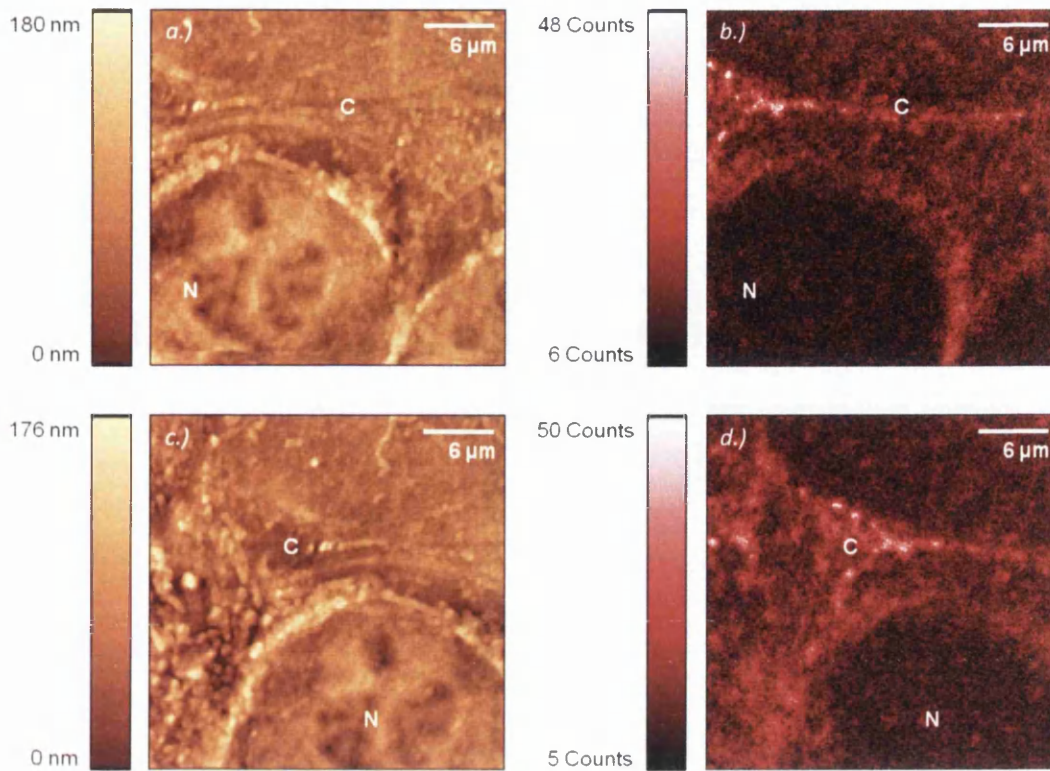


Figure 6.11: *SNOM topography (a) and (c) and optical (b) and (d) acquisitions of confluent PNT2 cells labelled with red quantum dots to reveal E-cadherin localisation. Cell-cell contact region and nucleus indicated by C and N respectively. All scans are $30 \mu\text{m} \times 30 \mu\text{m}$.*

A further image illustrating the change in topography at a cell-cell boundary of highly compact cells is shown in Figure 6.12. Again marked ridges which appear to run parallel to the cell-cell boundary (indicated by C on Figure 6.12) are seen. The multiple corrugations observed in Figure 6.12(a), were measured to span widths ranging approximately $7 - 8.7 \mu\text{m}$. Meanwhile, analysis of the cell-cell boundary in Figure 6.12(b) showed a single ridge running parallel to the boundary between the two cells. Measurements revealed the ridge diameter to range between approximately $400 - 850 \text{ nm}$ along its length.

It is interesting to speculate on the origin of these features. It is possible that these structures are an artefact of the highly confluent nature of the sample. Such that cells have become so compact they have begun to lift off the surface subsequently forming this ruffled appearance around their periphery. It is also possible that we are observing the underlying structure of the cytoskeleton. In

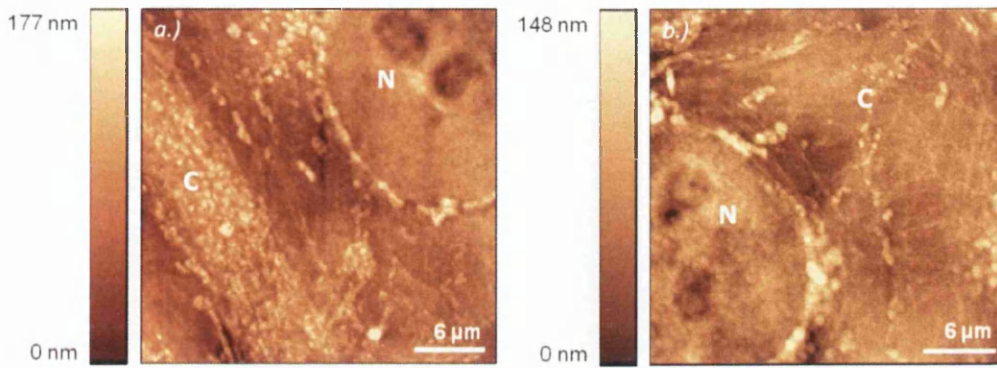


Figure 6.12: *SNOM topography image of confluent PNT2 cells. Cell-cell contact region and nucleus indicated by C and N respectively. Scans are $30\ \mu\text{m} \times 30\ \mu\text{m}$.*

which case, these structures may well be actin filaments that have reorganised to align parallel to the boundary following cell-cell contact as described by Yonemura *et al.* [11].

To investigate the origin of these features, further analysis of their molecular constituents is required. This could be achieved by examining confluent samples that are differentially labelled. Thus the location of actin, E-cadherin and other molecules involved in the formation of adherens junction could be analysed.

6.3.3 E-cadherin in non-confluent PNT2 samples

Fluorescence microscopy of non-confluent samples was carried out prior to SNOM imaging (Figure 6.9(a)). Figure 6.13 shows SNOM scans representative of when no cell-cell contact is established. The topographic and fluorescence scans shown in Figure 6.13(a) and (b) respectively reveal regions of interest that were subsequently scanned with higher resolution to generate Figures 6.13(c) and (d). As can be seen from the topographic images (a) and (c), the filopodia appear bunched and randomly orientated. This is in contrast to Figure 6.3, where the direction of filopodia appears to be far more driven towards the opposing cell. This is most likely due the cells in Figure 6.13 being fixed at a slightly earlier stage of confluency. The filopodia in Figure 6.13 are just starting to develop and initiate their sensing role that has been previously reported [3, 12]. Filopodia are often observed to extend into the intercellular matrix by up to $5 - 35\ \mu\text{m}$,

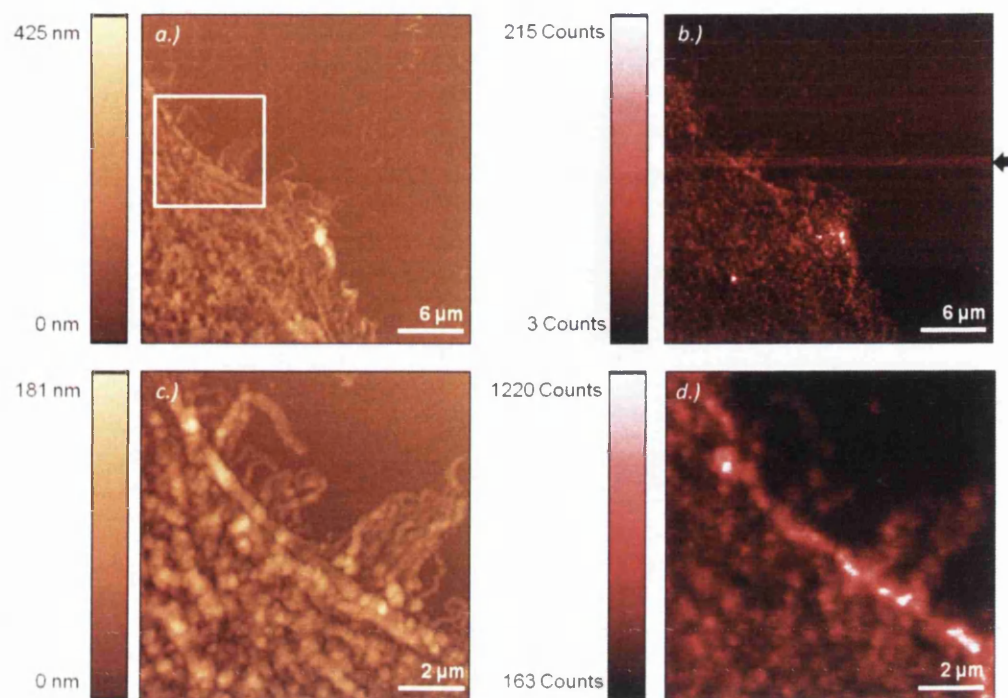


Figure 6.13: *SNOM topography (a) and optical (b) acquisitions of non-confluent PNT2 cells labelled with quantum dots to reveal E-cadherin is localised at the base of filopodia and to extend through their length. Boxed region indicated in (a) was subsequently imaged at higher resolution to generate (c) and (d). Scans (a) and (b) are $30\ \mu\text{m} \times 30\ \mu\text{m}$, (c) and (d) are $10\ \mu\text{m} \times 10\ \mu\text{m}$.*

sweeping from side to side and sensing for a particular substrate or cell. Although fixed, the filopodia in Figure 6.13 appear to be a snapshot of them exploring the local environment, possibly searching for other cells. Typically, when fixation was carried out such that cells had yet to establish any contact, filopodia were observed to extend up to approximately $5\ \mu\text{m}$ into the intercellular matrix.

Examination of the fluorescence images (Figures 6.13(b) and (d)) show E-cadherin is predominantly located at the membrane boundary at the base of the filopodia and much weaker signals in the filopodia themselves. Additionally, intermittent stripes of increased fluorescence intensity are discernable in Figure 6.13(b) (indicated by arrow). Similar features were observed in Figure 6.6 and are attributed to a single quantum dot that has become attached to the apex of the SNOM tip during scanning.

Furthermore, a significant difference in the number of counts recorded in Figures 6.13(b) and (d) is observed. This is attributed to slight changes in the

aperture of the SNOM tip as a result of repeated scanning. The quality of the optical response in Figure 6.13(d) is affected such that both the background and signal levels are higher in (d) than (b). However, superior signal-to-noise levels are evident in both images compared to those achieved through fluorescence labelling with Alexa Fluor 488. The observed change in the counts recorded by the APD is accompanied by a slight change in the resolution although this is difficult to quantify due to the accompanying changes in image scan step size. For the larger image (Figure (b)), the optical resolution is limited by the size of the image and the pixel resolution used during acquisition. Therefore one would expect an improvement on the optical resolution when imaging a smaller region. However, the sensitivity of the SNOM probe to interactions with the sample and tip aperture opening is one of the challenges of using SNOM to interrogate biological specimens.

6.4 Conclusion

Assessment of the prostate epithelial cell line PNT2 as a suitable model for SNOM studies proved successful, with topographic analysis resolving large micrometer sized features such as the nucleus and those of nanometer dimensions such as filopodia, revealing their “quilted” topology as observed by Doak *et al.* and shown in Figure 6.14 [2].

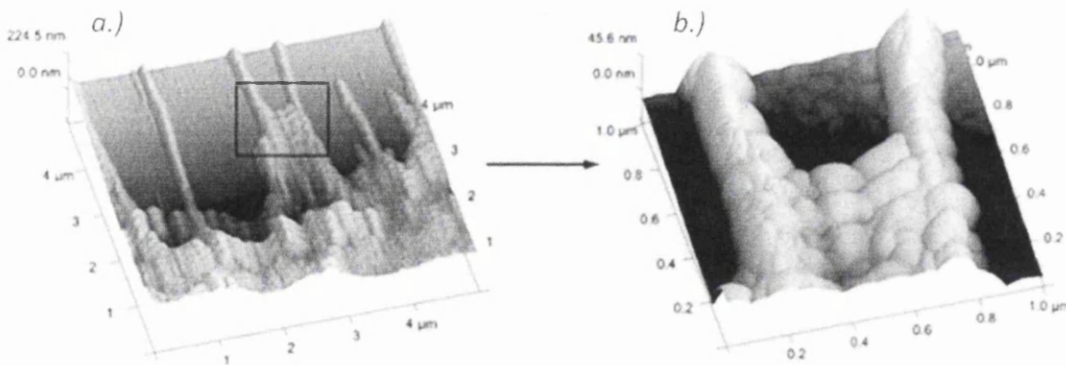


Figure 6.14: Atomic force microscopy images of a PNT2 cell, the boxed region in (a) was further resolved to show quilted appearance of filopodia surface (b). Adapted from [2].

Moreover, ridges were observed over the apical cell surface which are most likely cytoskeletal proteins that become visible as the membrane collapses following drying of the sample. Further assessment of PNT2 involved labelling the adhesion molecule E-cadherin with Alexa Fluor 488, in order to study its location within the cell. The early stages of cell-cell contact was observed and E-cadherin was found to be at sites of cell-cell contact mediated by filopodia interactions and within the filopodia themselves. A punctate cluster of E-cadherin was observed where filopodia had adhered to the opposing cell. Despite these initial promising results, a more robust and reliable labelling technique was required to facilitate repeated imaging of single samples.

This led to the development of quantum dot labelled samples, which proved partially successful in that substantially brighter and more resilient samples were produced. Furthermore, an optical feature of nano-dimensions was observed with a diameter measuring 60 ± 1 nm. This result is a direct realisation of the resolution capabilities afforded by SNOM that are not dictated by the diffraction limit.

It was also demonstrated that the high resolution imaging capacity of SNOM is better suited to detecting fluorescent signals which originate from the surface of a sample. Although it was not possible to detect specific signals from within the cell, it was nevertheless established that the use of quantum dots in future studies is favoured over organic fluorophores.

Thus, further analysis of adhesion mechanisms in PNT2 cells was completed using quantum dots. This SNOM study required optimisation of standard sample methodologies with particular attention paid to preserving the ultra-structural components in order to achieve high resolution topographic images and ensuring low background fluorescence levels. This enabled detection of small fluorescent signals arising from the specific labelling of molecular targets together with high quality imaging.

Analysis was undertaken at two stages of sample confluency. When cells were highly compact E-cadherin was predominantly found along the cell periphery but also to localise in the perinuclear region. Examination of the topology of

these samples revealed numerous corrugations running parallel to the cell-cell boundary. The origin of these structures needs further investigation, however it is proposed that these are circumferential F-actin filaments as described by Yonemura *et al.* [11]. When samples were prepared such that contact had yet to be established, E-cadherin was found to concentrate at the base of filopodia with some extension through their length. Filopodia appeared randomly oriented and seemed to be sensing the local environment.

This preliminary study provides a platform for further analysis of the mechanistic roles E-cadherin, accompanying adhesion molecules and filopodia play in establishing cell-cell adhesion. Moreover, the use of quantum dots as fluorescent labels has proved successful and superior signal-to-noise level were consistently observed for samples labelled with quantum dots compared to those labelled with Alexa Fluor 488. Signal-to-noise levels remained high (≥ 7) even when repeated scanning was undertaken on quantum dot labelled samples. Quantum dot labelling in conjunction with SNOM will play a continued role in developing a deeper understanding of how aberrations influence the behaviour of diseased cells and the impact of such abnormalities on cancer progression and metastasis. In particular, extending this study to examine different cancerous cell lines where E-cadherin expression levels are reported to vary and are associated with increased invasive capacity would enable the development of a more comprehensive understanding of the processes involved.

Bibliography

- [1] J. V. Small, T. Stradal, E. Vignal, and K. Rottner. The lamellipodium: where motility begins. *Trends in Cell Biology*, 12(3):112–120, 2002.
- [2] S. H. Doak, D. Rogers, B. Jones, L. Francis, R. S. Conlan, and C. Wright. High-resolution imaging using a novel atomic force microscope and confocal laser scanning microscope hybrid instrument: essential sample preparation aspects. *Histochem. Cell. Biol.*, 130(5):909–916, 2008.
- [3] B. Borm, R. Born, B. Merkel, and B. Hoffmann. Role of filopodia in adhesion formation during migration of epithelial cells. *Publication Series of the John von Neumann Institute for Computing*, 36:159–163, 2007.
- [4] V. Vasioukhin, C. Bauer, M. Yin, and E. Fuchs. Directed actin polymerisation is the driving force for epithelial cell-cell adhesion. *Cell*, 100:209–219, 2000.
- [5] <http://www.invitrogen.com/site/us/cn/home.html>.
- [6] X. Wu, H. Liu, Q. Liu, K. N. Hayley, J. A. Treadway, J. P. Larson, N. Ge, F. Peale, and M. P. Bruchez. Immunofluorescent labelling of cancer marking her2 and other cellular targets with semiconductor quantum dots. *Nature Biotechnology*, 21(1):41–46, 2003.
- [7] W. C. W. Chan and S. M. Nie. Quantum dot bioconjugates for ultrasensitive nonisotopic detection. *Science*, 281(5385):2016–2018, 1998.
- [8] M. Bruchez, M. Moronne, P. Gin, S. Weiss, and A. P. Alivisatos. Semiconductor nanocrystals as fluorescent biological labels. *Science*, 281(5385):2013–2016, 1998.
- [9] Y. Sonnefraud, N. Chevalier, J.-F. Motte, S. Huant, P. Reiss, J. Bleuse, F. Chandezon, M. T. Burnett, W. Ding, and S. A. Maier. Near-field optical imaging with a cdse single nanocrystal-based active tip. *Optics Express*, 14(22):10596, 2006.
- [10] Toronto Western Research Institute Wright Cell Imaging Facility. Autofluorescence: Causes and cures. <http://www.uhnresearch.ca/facilities/wcif/PDF/Autofluorescence.pdf>.

- [11] S. Yonemura, M. Itoh, A. Nagafuchi, and S. Tsukita. Cell-to-cell adherens junction formation and actin filament organisation: similarities and differences between non-polarized fibroblasts and polarized epithelial cells. *Journal of Cell Science*, 108(Part 1):127–142, 1995.
- [12] W. Wood and P. Martin. Structures in focus-filopodia. *The International Journal of Biochemistry & Cell Biology*, 34(7):726–730, 2002.

Chapter 7

Results: Multiplexing with semiconductor quantum dots

7.1 Motivation for multiplexing

Investigations into adhesion mechanisms in the normal prostatic epithelial cell line PNT2 discussed in Chapter 6 have laid the foundations for studies involving carcinoma cells. A comparative study of the prostate adenocarcinoma cell line PC-3, was undertaken to determine further functional information. Current research suggests E-cadherin expression is at reduced levels in PC-3 cells compared to that which is observed in normal epithelial tissues [1–4]. E-cadherin has been reported to play a significant role in suppressing tumour invasion of numerous cancers [5–7]. Furthermore, studies have shown that by chemically stimulating the expression of E-cadherin in PC-3 cells, their invasive potential is reduced [8]. Although such studies have improved our understanding of the role E-cadherin plays in cancer progression, many gaps in our knowledge remain. To this end, high-resolution SNOM imaging of cells has been undertaken to assess the extent of functional E-cadherin present in PC-3 cells. This has been determined through immunofluorescence labelling of E-cadherin.

As described previously in Chapter 6, investigations of E-cadherin expression have used immunofluorescent labelling in cells derived from normal prostate epithelial tissue. In anticipation of observing reduced E-cadherin levels in PC-3

cells and concomitant diminished fluorescence response, it was decided a suitable control would be needed to facilitate imaging.

When imaging with SNOM, very weak fluorescence signals are produced. Correct alignment of these weak signals onto the detector is crucial to ensure that maximum levels of fluorescence is recorded. Thus, observations of weak-to-non-existent signals, can be the result of signal misalignment rather than a true reflection of the samples properties. It was therefore vital to develop a reliable control method to deduce that a decrease in fluorescence signals is due to reduced levels of fluorophore, and not due to misalignment of the signal path onto the detector.

To this end, dual labelling of samples allows a control signal to be established. Samples were dually stained against E-cadherin and an additional protein, ZO-1, which is involved in the formation of tight junctions. Gene expression levels of both E-cadherin and ZO-1 have been quantified using a technique called real-time RT-PCR (reverse transcription polymerase chain reaction) [4]. Results from this study indicate that E-cadherin gene expression is down-regulated in PC-3 cells compared to that observed in healthy prostate epithelial cells. Whilst the genes which encode for ZO-1 proteins were found to be expressed to approximately the same extent in both PNT2 and PC-3 cell lines. Labelling of an additional protein provides a means to ensure that optical detection in our instrument is fully optimised.

7.2 Development of multiplexed samples

Development of a protocol that dual labelled the proteins E-cadherin and ZO-1 was primarily undertaken using PNT2 cells. Both proteins are positively expressed in this cell line which therefore facilitated the initial optimisation of the protocol. E-cadherin and ZO-1 expression in PNT2 cells was first demonstrated individually as shown by the fluorescent microscopy images in Figure 7.1.

Immunofluorescent labelling of E-cadherin was carried out using red (605 nm) emitting quantum dots as shown in Figure 7.1(a). This image shows E-cadherin to be present in areas where cell-to-cell contact occurs as observed in Chapter 6.

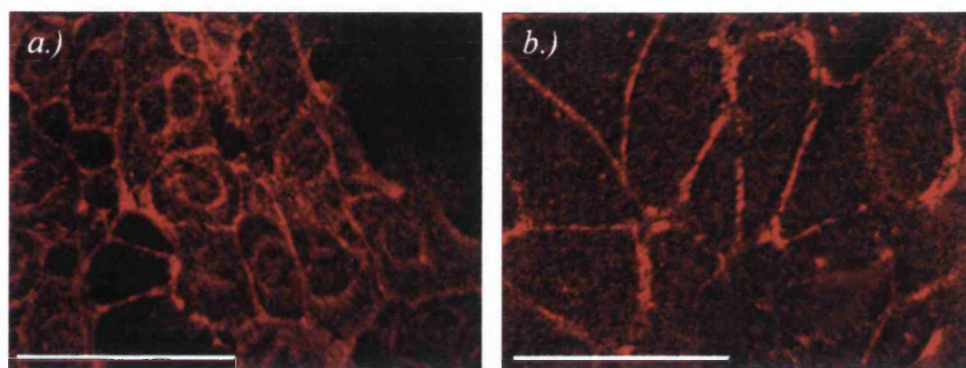


Figure 7.1: *Fluorescence microscopy images of PNT2 cells immunolabelled with semiconductor quantum dots to show (a) E-cadherin and (b) ZO-1. Scale bars represent approximately 100 μm .*

The location of ZO-1 is identified in Figure 7.1(b) where red (655 nm) emitting quantum dots were used to label ZO-1 proteins. As discussed in Chapter 4, ZO-1 proteins are involved in the formation of tight junctions, which play important roles in cell adhesion and regulating tissue permeability. In order to perform this function, ZO-1 proteins are localised around the circumference of cells. The fluorescence microscopy image shows that ZO-1 is present around the periphery of cells, in regions of cell-to-cell contact as expected.

To achieve fairly straightforward filter separation of the fluorescence signals produced by the dual stained samples, it was important to utilise quantum dots which emit at separate wavelengths. For this reason quantum dots with emission wavelengths of 655 nm and 525 nm were selected to label PNT2 cells as illustrated in Figure 7.2.

There are many advantages to using quantum dots over conventional fluorophores in fluorescent techniques. The multiplexing capabilities of quantum dots are widely acknowledged and are credited to such optical properties as large Stokes shift and broad absorption spectra [9–12]. These characteristics make quantum dots attractive for use in applications where more than one bio-molecule of interest can be detected simultaneously. However in practise, there are many difficulties that must be addressed when optimising a protocol which utilises multiplexing. Although very few of these have been reported by other research groups, significant difficulties were encountered in this study when attempting to

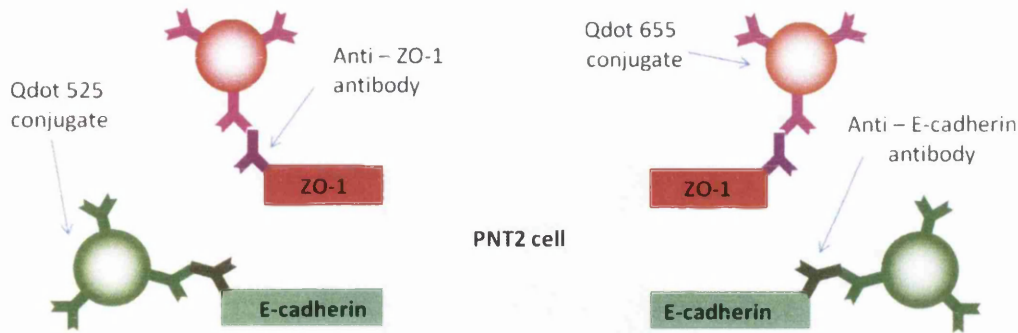


Figure 7.2: Graphic illustration of dual labelling in PNT2 cells to localise E-cadherin and ZO-1 simultaneously.

label the proteins E-cadherin and ZO-1 simultaneously. Initial attempts to optimise the dual labelling methodology proved problematic. A significant decrease in the quality of the fluorescent signals was observed following dual labelling, compared to that which was achieved when each protein was targetted separately.

There are various factors which may have affected the quality of the signals observed from dual labelled samples:

1. Application sequence

The sequence that quantum dots are applied to the sample may be an important factor that requires consideration during optimisation of sample preparations that incorporate dual labelling. Sweeney *et al.* [13] noted that the order of application affected the brightness of the dots when multiplexing. Their findings suggested that when applied sequentially in a multiplexing protocol, quantum dots with lowest quantum yield should be applied last. This is to ensure that they are subject to the least amount of PBS washes, minimising any removal once specifically hybridised. Furthermore in a recent study by Huang *et al.* [14], multiplexing was performed on formalin-fixed, paraffin embedded tissue samples. Their findings also suggest that the brightest quantum dots should be applied first to offset any reduction in signal intensity due to additional washing. Therefore the effect of the multiple washing steps should be considered in this work because of the more extensive rinsing the samples undergo in preparation for SNOM

imaging.

Sweeney *et al.* also reported that the order of application also affected the results through non-specific binding. Each secondary antibody was paired with a specific primary antibody. However, secondary antibodies were found to bind to residual empty sites of other primary antibodies. In the present study, the possibility that significant quantities of the quantum dots were non-specifically binding to the wrong primary antibodies was considered. This theory was rejected since the quantum dot conjugates utilised were highly cross-adsorbed and any cross-reactivity should be minimal.

2. Steric effects

Another issue that was taken into account is that of steric hindrance. This occurs when the size of one molecule applied inhibits the hybridisation of further molecules. Although the majority of studies by other research groups do not observe any hindrance to quantum dot binding during multiplexing [11, 13–15], this was initially considered to be the most probable explanation for the observed results in this work due to the physical proximity of the proteins on the cell membrane. A study by Newman *et al.* [16] involving colloidal gold conjugates found that the binding efficiency decreased with increasing conjugate size. The findings reported by Newman *et al.* may also be relevant to multiplexing studies involving quantum dots.

7.2.1 Protocol tests

In order to assess whether the processes discussed in the previous section were affecting hybridisation of the quantum dot conjugates, the effect of changing the order of quantum dot application was examined. The numerous protocols that were tested are illustrated in Figure 7.3 for clarity. In this figure, only the interchangeable steps have been included and labelled 1 – 4 to identify where these steps slot into the overall labelling procedure given in Figure 5.9, in Chapter 5. A key is provided at the bottom of Figure 7.3 which reveals the name and concentration of the reagents used during each step.

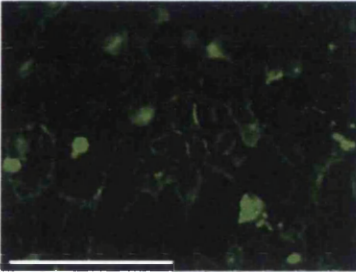
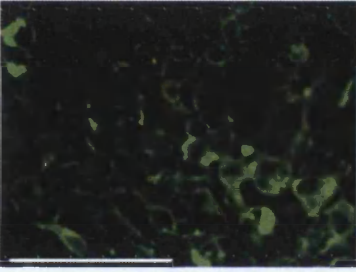
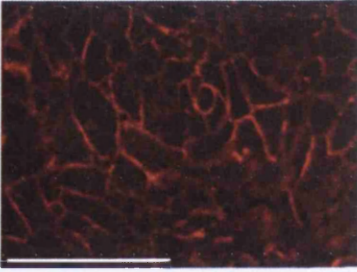
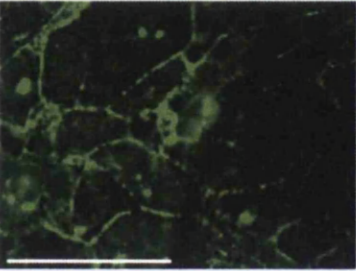
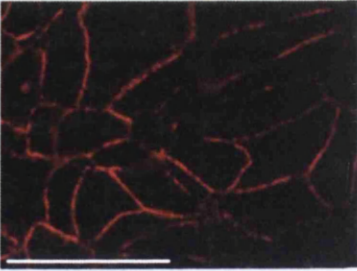
	Protocol	E-cadherin	ZO-1	
A.	<ol style="list-style-type: none"> 1. ZO-1 1° 1:25 2. E-cad 1° 1:10 3. ZO-1 2° 2:100 4. E-cad 2° 2:98 	Very little specific labelling observed. No images acquired.		
B.	<ol style="list-style-type: none"> 1. ZO-1 1° 1:25 2. E-cad 1° 1:5 3. ZO-1 2° 2:100 4. E-cad 2° 3:97 <p>Generally, E-cadherin specific labelling was weak and ZO-1 labelling inconsistent.</p>			
C.	<ol style="list-style-type: none"> 1. E-cad 1° 1:10 2. ZO-1 1° 1:25 3. E-cad 2° 2:98 4. ZO-1 2° 2:100 <p>E-cadherin labelling was better than that achieved through B. ZO-1 labelling looked OK.</p>			
D.	<ol style="list-style-type: none"> 1. ZO-1 1° 1:25 2. ZO-1 2° 2:100 3. E-cad 1° 1:10 4. E-cad 2° 2:98 <p>Best results: E-cadherin labelling most consistent. ZO-1 labelling also good.</p>			
Key	Step	Reagent name	Concentration	1° = Primary antibody
e.g.	1.	E-cad 1°	1:10 (Reagent: Buffer)	2° = Secondary antibody

Figure 7.3: Table summarising protocols tested during initial optimisation of dual labelling and synopsis of the quality of samples produced by each. Example fluorescence microscopy images showing ZO-1 (red) and E-cadherin (green) labelling for each protocol. Scale bars represent approximately 100 μ m.

Corresponding fluorescence microscopy images of dual labelled PNT2 cells are also provided where possible. E-cadherin location is indicated by fluorescence from green emitting quantum dots and the location of ZO-1 is revealed by the presence of fluorescence from red emitting quantum dots. The protocol steps have been colour coded appropriately to reflect this. Red and green fluorescence microscopy images portray the same region of the sample but different filter sets were utilised to separately capture the fluorescence from each colour quantum dot. It should be noted that the fluorescence microscopy images represent regions of the sample where immunolabelling has been most successful, in terms of strong specific and low background labelling. However the labelling protocols have been evaluated on how successful the labelling procedure was over the whole of the sample, which is summarised in Figure 7.3.

Protocol (A) resulted in very little specific labelling and as such no fluorescence images could be acquired. In an attempt to improve the fluorescence labelling, the concentration of reagents used to label E-cadherin were increased as given in protocol (B). However this gave little improvement on the results. The specific labelling of E-cadherin remained weak and ZO-1 labelling was inconsistent. Additionally, high levels of non-specific staining was observed on samples prepared with protocol (B). Therefore E-cadherin primary and secondary antibody dilutions were reverted back to their original values for subsequent protocols, to avoid such high levels of non-specific labelling.

It was anticipated that steric effects maybe taking place during protocols (A) and (B). In which case the application of ZO-1 primary antibodies in step 1 would inhibit the subsequent binding of E-cadherin primary antibodies in step 2. Similarly, step 3 would hinder step 4. This cumulative effect would result in a strong fluorescent response from ZO-1 bound quantum dots and a weak response from E-cadherin.

In order to test whether E-cadherin hybridisation was being hindered by ZO-1 antibodies, protocol (C) was carried out. It was expected that by revising the order of steps such that E-cadherin reagents are applied before ZO-1, steric interference of E-cadherin would be minimised. Protocol (C) was expected to

produce samples with stronger E-cadherin fluorescence which would likely result in weaker signals from ZO-1 due to steric hindrance effects.

However, protocol (C) gave improved labelling of E-cadherin and ZO-1 proteins. This suggests steric hindrance may have been responsible for the poor E-cadherin fluorescence labelling from protocols (A) and (B). Furthermore, the improved ZO-1 labelling observed when protocol (C) was used, may be explained by steric hindrance of ZO-1 secondary antibodies due to the presence of E-cadherin primary antibodies in (A) and (B).

Protocol (D) was carried out to further test the possibilities of steric hindrance. Additionally, protocol (D) would test whether repeated washing was affecting the fluorescence signals. The protocol was amended such that the green emitting quantum dots with lowest quantum yield, were applied last making them subject to less washing steps.

Comparison of samples produced by protocols (C) and (D) revealed that protocol (D) provided slightly more consistent labelling for both E-cadherin and ZO-1 proteins. This is reflected in the fluorescence microscopy images. This may be in part due to the E-cadherin quantum dots being subject to less washing steps. These results suggest that steric hindrance of E-cadherin reagents is not the primary reason for the poor fluorescence signals observed.

However, there was not a great difference in the quality of fluorescence labelling arising from each of these methods. The quality of the fluorescence labelling from dual labelled E-cadherin and ZO-1 was poorer compared to the fluorescence labelling of E-cadherin and ZO-1 independently. These findings suggested that there may be other processes occurring which had not been considered previously.

It is vital that fluorescence signals which enable identification of E-cadherin are fully optimised. This is to ensure that immunolabelling accurately reflects the presence of E-cadherin. For this reason the decision was made to attempt labelling of E-cadherin with longer wavelength quantum dots and ZO-1 with the shorter wavelength, as illustrated by Figure 7.4. This appeared to be the most practical resolution since ZO-1 labelling is required to act as a detection control.

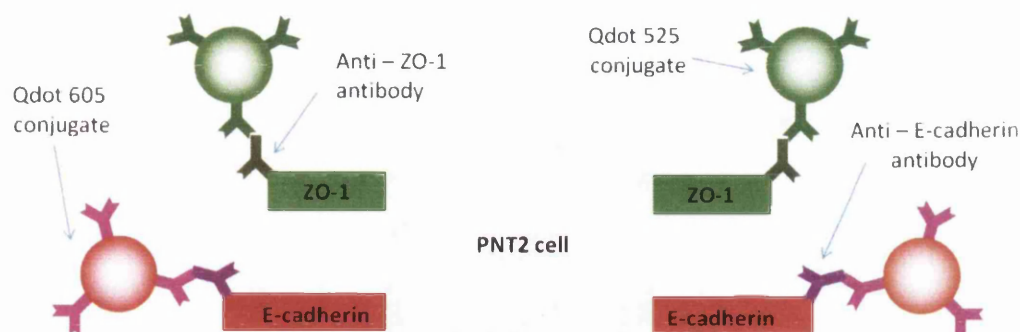


Figure 7.4: *Graphic illustration of dual labelling in PNT2 cells to localise E-cadherin and ZO-1 simultaneously.*

7.2.2 Further optimisation

As illustrated in Figure 7.4 the quantum dots used to label E-cadherin and ZO-1 were revised such that E-cadherin proteins were labelled with the brighter, red quantum dots. It is important to emphasise again that labelling of ZO-1 proteins is purely to ensure that detection equipment is fully aligned. Thus detection of ZO-1 is only necessary when E-cadherin levels are reduced or not detectable.

Numerous protocols were tested using this new arrangement and the effect of altering the concentration of reagents and reversing the order of application of reagents were examined. For clarity, these protocols are summarised in Figure 7.5 and a key is provided to explain each step. The steps are again labelled 1 – 4 to indicate where they slot into the complete protocol which is provided in full in Figure 5.9, in Chapter 5. Where it was possible to obtain fluorescent microscopy images these are provided and a synopsis of the effectiveness of the labelling is given. E-cadherin is identified by red fluorescence and ZO-1 by green. The fluorescent dye DAPI was used as a positive control to isolate nuclei (blue fluorescence), this step was taken to aid detection of the desired targets by making it easier to identify cells. It was also found that imaging the samples through triple channel filters provided superior quality images of the samples, most likely due to the filters being a more suitable match to the fluorescence emission wavelength of the quantum dots. As with previous protocol tests, the fluorescence microscopy

7.2. DEVELOPMENT OF MULTIPLEXED SAMPLES

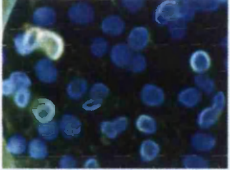
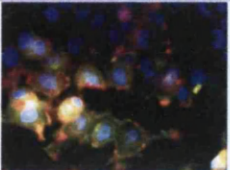
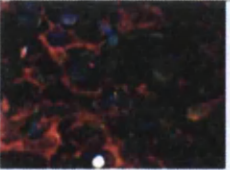
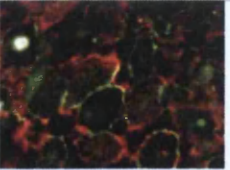
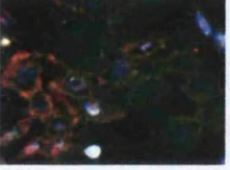
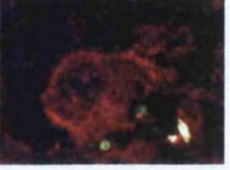
Protocol				
A.	<ol style="list-style-type: none"> ZO-1 1° 1:15 ZO-1 2° 3:100 E-cad 1° 1:10 E-cad 2° 2:98 		E-cadherin and ZO-1 labelling OK.	
B.	<ol style="list-style-type: none"> ZO-1 1° 1:15 ZO-1 2° 2:100 E-cad 1° 1:10 E-cad 2° 2:98 	No images obtained. Poor labelling.		
C.	<ol style="list-style-type: none"> ZO-1 1° 1:25 ZO-1 2° 3:100 E-cad 1° 1:10 E-cad 2° 2:98 		E-cadherin specific labelling was very inconsistent and little specific ZO-1 labelling.	
D.	<ol style="list-style-type: none"> E-cad 1° 1:10 ZO-1 1° 1:15 E-cad 2° 2:98 ZO-1 2° 3:100 	No images obtained. E-cadherin and ZO-1 specific labelling was weak but consistent.		
E.	<ol style="list-style-type: none"> E-cad 1° 1:10 ZO-1 1° 1:15 E-cad 2° 2:98 ZO-1 2° 2:100 	E-cadherin labelling was good. ZO-1 labelling was not as good as D.		
F.	<ol style="list-style-type: none"> E-cad 1° 1:10 ZO-1 1° 1:25 E-cad 2° 2:98 ZO-1 2° 3:100 	Very little ZO-1 specific labelling. E-cadherin appeared mostly around nucleus, little labelling at cell-cell contacts (this has been seen previously and was most likely a true reflection of E-cadherin location rather than non-specific E-cadherin labelling).		
A.	<ol style="list-style-type: none"> ZO-1 1° 1:15 ZO-1 2° 3:100 E-cad 1° 1:10 E-cad 2° 2:98 			Very consistent and specific labelling, albeit weak in the case of ZO-1
G.	<ol style="list-style-type: none"> E-cad 1° 1:10 E-cad 2° 2:98 ZO-1 1° 1:15 ZO-1 2° 3:100 			E-cadherin labelling is strong although not as consistent as A. Weak ZO-1 labelling.
Key	Step	Reagent name	Concentration	1° = Primary antibody 2° = Secondary antibody
	1.	E-cad 1°	1:10 (Reagent: Buffer)	

Figure 7.5: Table summarising protocols tested during final optimisation of dual labelling of PNT2 cells and synopsis of the quality of samples produced by each. Example fluorescence microscopy images showing ZO-1 (green) and E-cadherin (red) labelling for each protocol.

images represent regions of the sample where labelling was most successful. However, the protocols were evaluated on how effective labelling was over the entire sample.

Initially, protocols (A)-(F) were carried out and it was found that using the higher concentration of ZO-1 primary and secondary antibodies (1:15 and 3:100 respectively) gave superior and more consistent labelling of ZO-1 with green quantum dots. Protocols (A) and (G) were then carried out in parallel to ensure that the order of application chosen did provide the best possible result for both E-cadherin and ZO-1 labelling. These final tests confirmed that protocol (A) produced the most specific and consistent labelling of both proteins when targeted simultaneously. Thus protocol (A) was selected for subsequent sample preparations for further investigation using SNOM.

7.3 Results of multiplexing in PNT2 cells

7.3.1 Spectral analysis

In order to distinguish between red and green fluorescence when examining dual labelled samples with SNOM, a selection of band pass filters were tested to assess their efficiency at spectrally separating the two signals. Using data provided by the manufacturers, the transmission spectra of numerous filters were compared and plotted against emission spectra for the quantum dots. The spectra shown in Figure 7.6 shows the results for a 525 nm band pass filter and a 609 nm band pass filter. These filters were selected because their transmission properties and spectral bandwidth ensures they can adequately separate fluorescence originating from the two different colour quantum dots, while allowing a large proportion of the required colour to pass through.

Experimentally acquired data to validate the performance of the optical filters when used with different colour quantum dots is shown in Figure 7.7. Two solutions were prepared by diluting 525 nm or 605 nm quantum dots in a 6% BSA/PBS buffer. The solution containing red emitting, 605 nm quantum dots was examined by depositing a small amount onto a clean, glass coverslip and

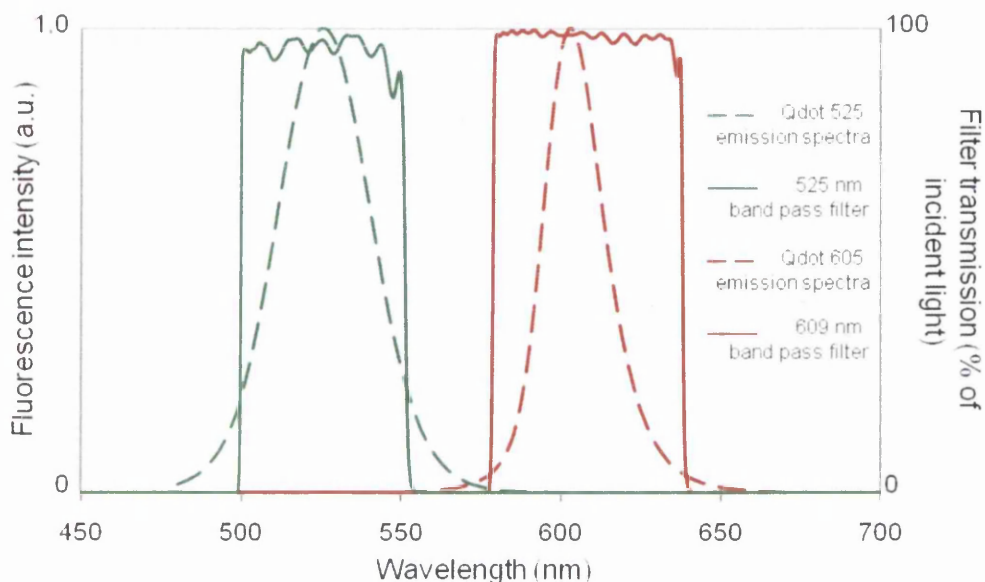


Figure 7.6: Spectra showing emission of green and red quantum dots (dashed lines) [17] and transmission properties of optical band pass filters (solid lines).

illuminating with a 488 nm Ar^+ laser. The resulting fluorescence was collected, passed through a 488 nm Raman edge filter to remove light from the laser and directed into a spectrometer.

The spectrum shown in Figure 7.7(a) is the result of a 10 minute acquisition. The spectrum reveals a narrow, Gaussian peak which is centred at approximately 605 nm, corresponding to the fluorescence originating from the red quantum dots. The 609 nm band pass filter was then introduced into the optical path and the collection was repeated generating spectra (b). The filter allows the fluorescence to pass through with little reduction in intensity. The optical filter was then exchanged for a 525 nm band pass filter which is suited towards the collection of fluorescence from green quantum dots. As can be seen in the resulting spectra (c), none of the fluorescence from the red quantum dots passes through this filter. This demonstrates the effectiveness of the 525 nm band pass filter at eliminating red light from the total signal collected when only green fluorescence is required. A small amount of laser light bleed-through is present in all of the spectra, this can be seen as a sharp peak at around 488 nm, as identified on spectra (c).

The sample was then removed and the process repeated for green emitting,

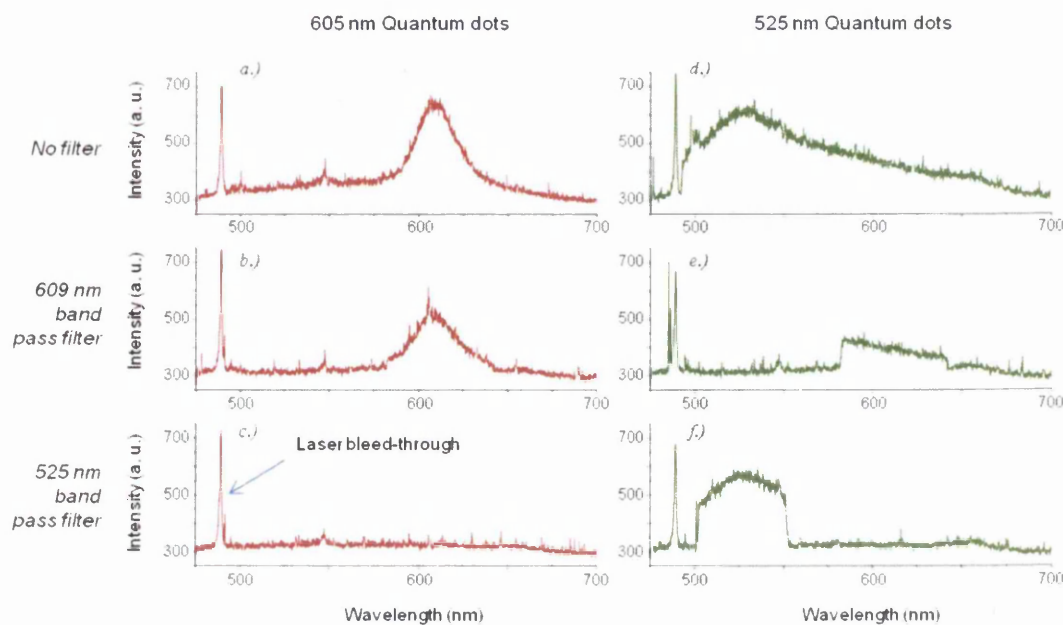


Figure 7.7: Fluorescence spectra of quantum dots with 605 nm (a) and 525 nm (d) emission. Spectra repeated with 609 nm optical band pass filter (b) and (e) and 525 nm optical band pass filter in place (c) and (f) for each colour quantum dot.

525 nm quantum dots. The resulting spectrum is shown in Figure 7.7(d). The spectrum reveals an asymmetric peak which is centred at approximately 525 nm, corresponding to the fluorescence originating from the green quantum dots, which tails off into the red end of the spectrum. The 609 nm band pass filter was then introduced into the optical path and the collection was repeated generating spectra (e). The filter allows a small amount of the red-tail of the fluorescence to pass through. The optical filter was then exchanged for a 525 nm band pass filter and as can be seen in the resulting spectra (f), this filter allows a large proportion of the green fluorescence to be collected.

7.3.2 Multiplexing in PNT2

Upon completion of optimisation work, dual labelled samples were observed using a fluorescence microscope. The images shown in Figure 7.8 represent the same region but viewed with different filter sets to allow separate examination of (a) ZO-1 and (b) E-cadherin localisation. Image (c) represents an overlay of

images (a) and (b). The fluorescence microscopy images demonstrate successful labelling of both E-cadherin (red) and ZO-1 (green) simultaneously and both proteins are predominantly found at regions of cell-cell contact.

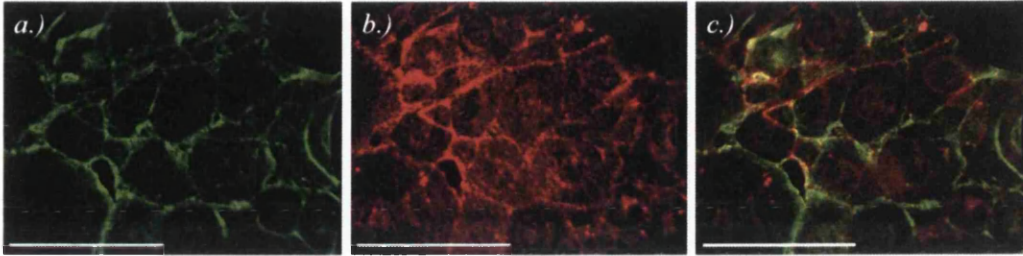


Figure 7.8: *Result of dual labelling PNT2 cells to simultaneously examine the location of ZO-1 (a) and E-cadherin (b). Images were obtained by fluorescence microscopy. (c) represents an overlay of the images shown in (a) and (b). Scale bars represent approximately $100\mu\text{m}$.*

Samples were subsequently examined using SNOM and the images presented in Figure 7.9 were generated. Topography information can be seen in Figures 7.9(a) and (b), which were acquired to demonstrate that the extensive dual labelling protocol does not result in changes to the structure of the sample. As can be seen in image (a), the cellular structure remains well preserved and features previously observed in topography images of individually labelled PNT2 samples (Figures 6.3 and 6.13 in Chapter 6) can clearly be distinguished. Numerous filopodia can be seen to extend across the intercellular region between two neighbouring cells (indicated by arrows), and many can be seen interacting with opposing filopodia. Although most cellular features are difficult to distinguish in image (b), the cell boundaries can clearly be seen.

Corresponding optical images were acquired for the topography image shown in Figure 7.9(b) which reveal the location of E-cadherin and ZO-1. ZO-1 locality is revealed by fluorescence from green emitting quantum dots as shown in Figure 7.9(c). Green fluorescence was selectively filtered using a 525 nm band pass filter and recorded by an APD using a collection time of 20 ms per pixel. Although the signal-to-noise attained in this image does not result in great contrast, signals can be seen predominantly in regions which correspond to the cell edge. Imaging of ZO-1 was purely to provide confirmation that signals were correctly aligned so

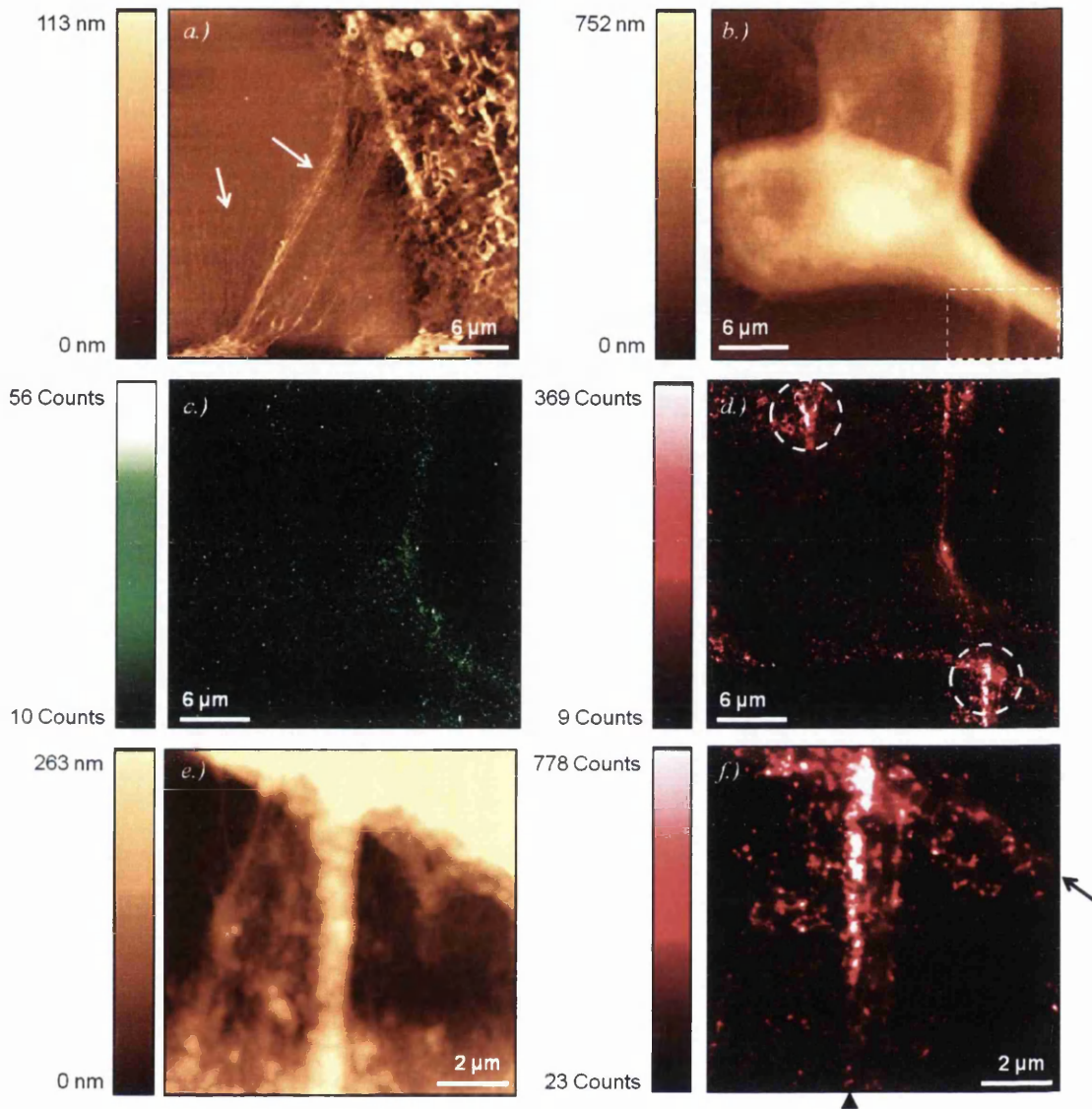


Figure 7.9: SNOM acquisitions of dual labelled PNT2 cells. (a) Topography image, filopodia indicated by arrows. (b) Topography acquisition and corresponding optical images (c) and (d) obtained with different filters to spectrally distinguish green and red fluorescence, identifying ZO-1 and E-cadherin locations respectively. Boxed region in (b) subsequently scanned with higher resolution to generate (e) topography and (f) optical images. Circled regions in (d) and arrows in (f) highlight E-cadherin clusters. (a)-(d) measure $(30 \mu\text{m})^2$, (e) and (f) are $(10 \mu\text{m})^2$.

for this purpose, achieving the highest possible quality images of ZO-1 was not a priority.

To examine E-cadherin, the 525 nm band pass filter was removed and replaced with a 609 nm band pass filter to allow detection of red emitting quantum dots. The ensuing fluorescence image obtained is shown in Figure 7.9(d). Considerably enhanced signal-to-noise is achieved when examining red fluorescence. This is likely to be in part due to the brighter nature of the red quantum dots compared to green. E-cadherin location is identified by fluorescence from specifically hybridised red quantum dots. Examining Figure 7.9(d) reveals E-cadherin is primarily found along the cell boundaries. Furthermore, particularly high levels of fluorescence are recorded in two regions on the sample (circled in Figure 7.9(d)). This observation is consistent with results from single labelled PNT2 samples, where E-cadherin was predominantly found to concentrate along the cell periphery. Punctate clusters of E-cadherin were also observed in regions where cell-cell contact had been established.

In order to examine regions with high fluorescent activity in closer detail, the boxed region in Figure 7.9(b) was subsequently scanned with higher-resolution. The resulting topography image is presented in Figure 7.9(e). The colour scale which represents height has been set to exclude the highest features which are masked by the gold coloured region in the top right of the image. This process enables flatter structures to be observed more clearly and as such a series of ridges can be seen running vertically in the image. This likely represents a network of filopodia from neighbouring cells that have established contact and are responsible for pulling the cells together, forming a tight seal

This is further demonstrated in the simultaneously acquired optical image (Figure 7.9(f)). A row of fluorescence corresponding to E-cadherin location can be seen running parallel to the edge of one cell and perpendicular to this network of filopodia (see arrow on image (f)). Additional rows of fluorescence are also present along the length of the large filopodium in the centre of the image (identified by arrowhead). These results confirm that the localisation of E-cadherin can be successfully examined in samples that have been dual stained.

7.4 Structural analysis of PC-3 cells

The morphology of PC-3 cells has been reported in studies by other research groups to differ from that of healthy epithelial cells [8, 18]. When cultured in monolayers, healthy epithelial cells tend to be regular in shape and exhibit a rounded morphology, becoming more cuboidal or cobble stone-like in appearance when cells are more densely packed. Furthermore, healthy cells form tight cell-cell associations with their neighbours. Healthy cells also typically tend to be quite flattened [18]. These features are characteristic of the normal epithelial cells, PNT2, that were examined during earlier investigations in this study, as shown in Figures 7.8 and 7.9. This is further demonstrated by the bright field microscopy image of confluent PNT2 cells shown in Figure 7.10(a). PC-3 cells display a markedly different appearance as exemplified in Figure 7.10(b) which shows PC-3 cells examined by bright field microscopy.

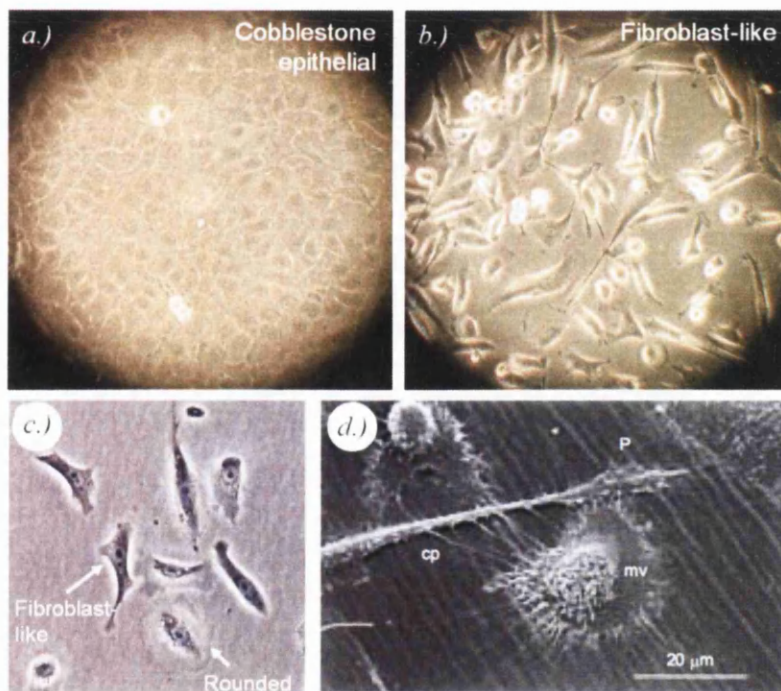


Figure 7.10: Morphology of (a) PNT2 cells and (b) PC-3 cells examined by bright field microscopy. PC-3 cells as seen by (c) phase contrast microscopy and (d) scanning electron microscopy. *mv* indicates microvilli on the cell surface, *cp* indicates cell projection and *P* indicates elongated pseudopodia-like projection. Images (c) and (d) taken from Lang et al. [18].

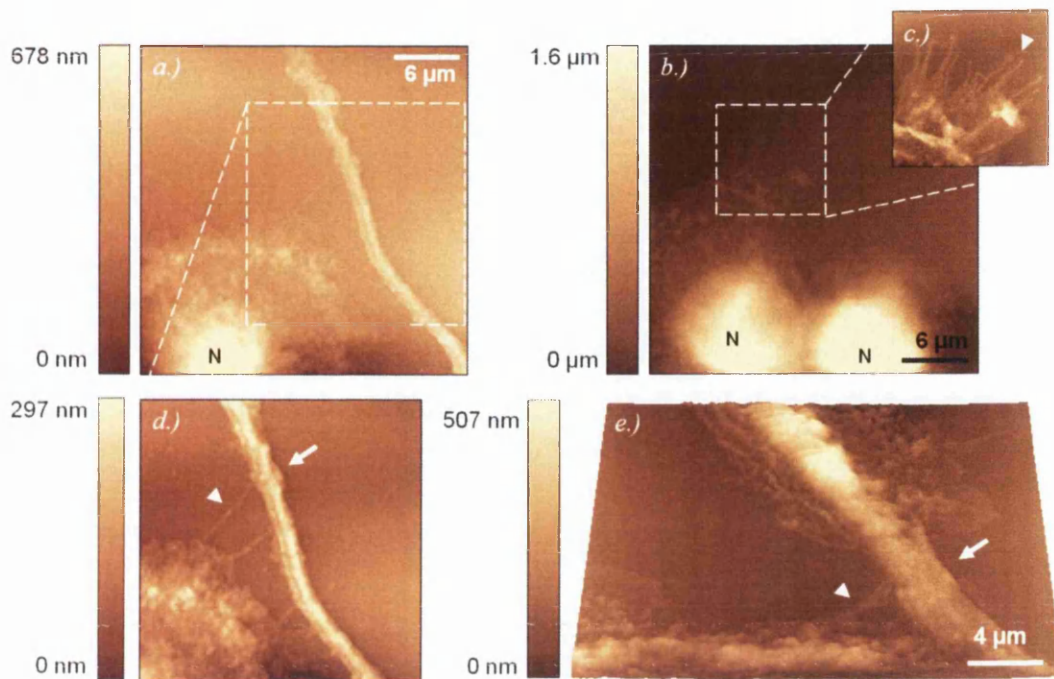


Figure 7.11: Typical SNOM topography acquisitions of non-confluent PC-3 cells. Some cells display a rounded morphology (as in (a) and (b)), while others appear more fibroblast-like (as in (e)). N denotes the nucleus and filopodia are indicated by arrowheads. Arrows indicate elongated lamellipodia. Boxed regions in (a) and (b) correspond to software zooms shown in (d) and (c) respectively. (a), (b) and (e) are $(30 \mu\text{m})^2$, (c) is $(10 \mu\text{m})^2$ and (d) is $(20 \mu\text{m})^2$.

Also included in Figure 7.10 are images of PC-3 cells obtained by Lang *et al.* [18] using phase microscopy (c) and scanning electron microscopy (d). As indicated in Figure 7.10(c), the studies by Lang *et al.* showed that although some PC-3 cells display a rounded morphology, others appeared more elongated and fibroblast-like. Their studies found PC-3 cells were not as flat as the healthy epithelial cells they examined and assumed a more 3-dimensional appearance. Lang *et al.* also noted that PC-3 cells often possess elongated lamellipodia (identified as pseudopodia by Lang *et al.* [18], indicated by P on Figure 7.10(d)) and numerous filopodia. In contrast to healthy cells, they also found that the cancerous PC-3 cells form loose cell-cell contacts when confluent. The fibroblast-like appearance typical of PC-3 cells is also evident in Figure 7.10(b).

Prior to immunolabelling of PC-3 cells, their morphology was examined using SNOM topography acquisitions. The images shown in Figure 7.11 directly

confirm the observations reported by Lang *et al.* discussed above. Some cells appear spherically shaped as demonstrated in Figures 7.11(a) and (b) while others exhibit a more fibroblast-like morphology with long, branching cytoplasmic protrusions (as indicated by arrows in Figures 7.11(d) and (e)). These protrusions are significantly longer than the filopodia typically observed on healthy cells and were often found to extend to lengths greater than $25 - 30 \mu\text{m}$, the size of the topography scans. Additionally, measurements show their diameter to be much wider than the finer filopodia, some of which can be distinguished protruding from the lamellipodia as indicated by arrowheads in Figure 7.11. These larger protrusions tend to taper as their length increases however, at their widest point they were found to measure up to $2.1 \mu\text{m}$ and to reach heights of up to approximately 300 nm . Measurements on the finer protrusions observed in these images revealed widths ranging between $120 - 340 \text{ nm}$, which are consistent with the filopodia observed on healthy PNT2 cells as discussed in Chapter 6 and reported by Doak *et al.* [19].

The cells' nuclei (indicated by N) can clearly be distinguished in Figures 7.11(a) and (b). The maximum height of the cells occurred over the nuclear region and measurements indicate the maximum height of PC-3 cells was in the range $(1.65 - 1.96) \mu\text{m}$. Doak *et al.* reported that the height of healthy PNT2 cells were generally in the range $1.22 - 1.55 \mu\text{m}$, however they noted that the height of the cells depended on the fixative used [19]. Thus, for a true comparison between the healthy PNT2 and cancerous PC-3 cells, samples prepared under the same fixing conditions should be used. However, analysis of PNT2 cells in Chapter 6 gave a wide range of values for the height of PNT2 cells, even though the samples were subject to the same fixing conditions and desiccation prior to imaging. The maximum height of PNT2 samples ranged from approximately $0.5 - 2.7 \mu\text{m}$, and is possibly due in part to the degree of confluency of the cells. As such it is difficult to compare between the two cell lines. However it was noted that increases in height across PNT2 cells usually occurred gradually and over relatively large distances. Whereas PC-3 cells were often found to possess high features that were abrupt. These steep aspects of their structure made it considerably more difficult

to achieve high quality topography images when scanning with SNOM. Dramatic changes in height required very precise optimisation of scanning parameters. The difficulties experienced during scanning of high features is discussed more fully in Chapter 5.

The morphology of confluent PC-3 cells is also noticeably different to healthy PNT2 cells. Figure 7.12 shows typical SNOM topography acquisitions of PC-3 cells which were fixed at a later stage such that cells have become densely packed. The boxed regions in Figures 7.12(a) and (b) represent areas that were subsequently zoomed in. This enabled superior contrast between features of similar height and exposed much more detail.

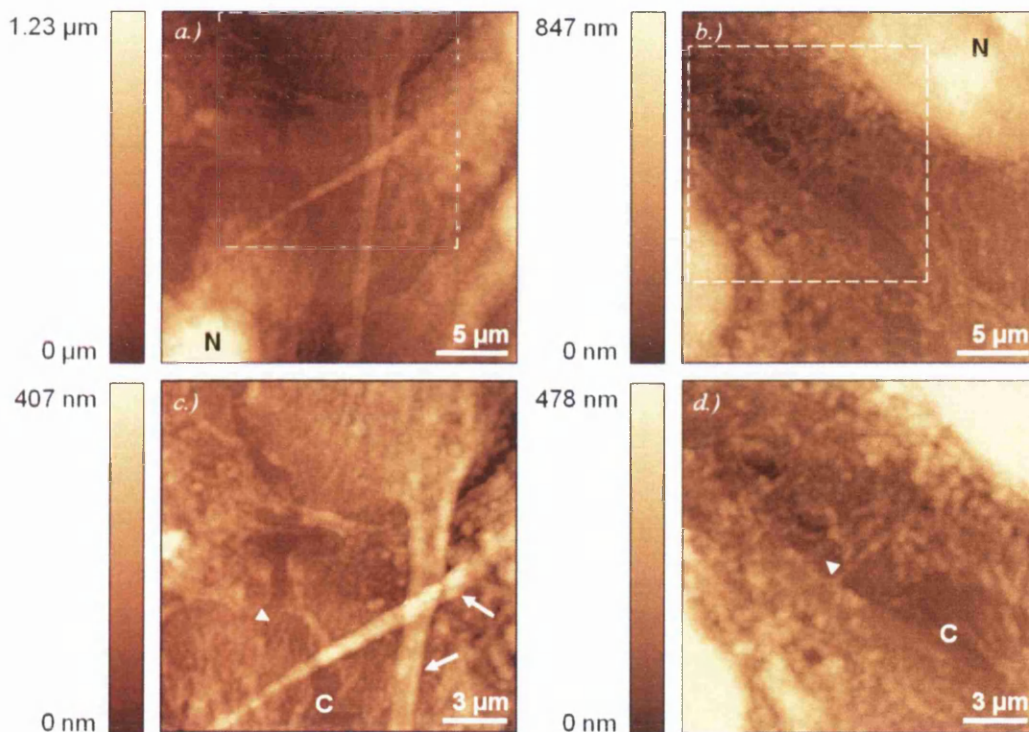


Figure 7.12: *Confluent PC-3 cells show loose cell-cell associations along the boundary between cells, as indicated by C. Fine filopodia are denoted by arrowheads while elongated lamellipodia are indicated by arrows. N indicates nuclei. Topographic SNOM acquisitions (a) and (b) and respective software zooms (c) and (d). (a) and (b) are $(25 \mu\text{m})^2$, (c) and (d) are $(16.7 \mu\text{m})^2$.*

In contrast to confluent PNT2 cells, PC-3 cells do not appear to form very close associations with neighbouring cells. This is exemplified by the images shown in Figure 7.12 but is particularly clear in image (c). Gaps of up to $2.1 \mu\text{m}$

around the periphery of the cells are observed and no seal along the boundary between adjacent cells has been established (cell-cell boundary is indicated by C). This observation is consistent with reports by Lang *et al.* who noted similar morphological differences between healthy and cancerous prostate epithelial cell lines [18].

Numerous fine filopodial extensions can also be seen to protrude across these gaps, however few appear to interact with those from opposing cells. This is remarkably different to PNT2 cells where filopodia from adjacent cells were observed to interdigitate across the intercellular region. When PNT2 cells achieved the high confluency as is reached by the PC-3 cells in Figure 7.12, the PNT2 cells were fully sealed together and no gaps could be distinguished, as was shown in Figure 6.11 in Chapter 6. The lack of contact between the PC-3 cells observed in Figure 7.12 is possibly due to a lack of functional E-cadherin proteins. As discussed in Chapter 4, previous studies that have assessed E-cadherin expression and localisation in PC-3 cells have not reached a consensus [1–3, 8, 18, 20]. This study aims to determine whether E-cadherin is functionally expressed in PC-3 cells and found in regions which confer cell-cell adhesion using the high-resolution fluorescence capabilities of SNOM.

7.5 Optimisation of dual labelling in PC-3

Following extensive optimisation of the dual labelling protocol using PNT2 cells as discussed in Section 7.2, samples consisting of PC-3 cells were prepared and treated in the same way. Initial results showed extremely high levels of non-specific labelling with quantum dots present within the cytoplasm of cells and attached arbitrarily to the slide surface. Furthermore, PC-3 cells often appeared to become completely removed from the surface following application of the labelling protocol. Very few cells were typically observed when the samples were examined by fluorescent microscopy, even though when viewed prior to and after fixation, the same samples appeared highly confluent.

Significant work was completed in an attempt to optimise the dual labelling

procedure for PC-3 cells. The following measures were taken in an attempt to improve the quality of the samples:

- Introducing additional PBS/Glycine washes to the protocol in an effort to reduce non-specific binding of antibodies to the surface by blocking free aldehyde groups.
- Coverslips were coated with poly-l-lysine before deposition of cells. This coating is commonly used to improve cell adherence to surfaces and was used here in an effort to reduce the number of cells that were detaching during the extensive labelling procedure.
- Changing the concentration of labelling reagents
- Changing the order of application of labelling reagents

These measures varied in their effectiveness: Coating the coverslips to improve cell adherence unexpectedly had the most detrimental effect and actually resulted in fewer cells remaining at the end of the protocol. The protocol was eventually optimised by finding a compromise between the concentration of reagents that consistently produced the highest levels of specific labelling and minimising non-specific binding through additional blocking washes.

7.6 Results of multiplexing in PC-3

Dual labelled PC-3 cells were imaged with a fluorescence microscope, results obtained were typical of those shown in Figure 7.13. The image shown in Figure 7.13(a) identifies ZO-1 proteins around the circumference of the cells as observed for the healthy PNT2 cells. E-cadherin proteins were targeted by red emitting quantum dots, however as seen in Figure 7.13(b) very little fluorescence can be seen in regions which correspond to the cell-cell boundaries. The image shown in Figure 7.13(c) represents both red and green fluorescent images overlaid.

The poor quality of the fluorescence microscopy images obtained however made it difficult to correlate fluorescence and cellular regions, making a strong case for a detailed SNOM study.

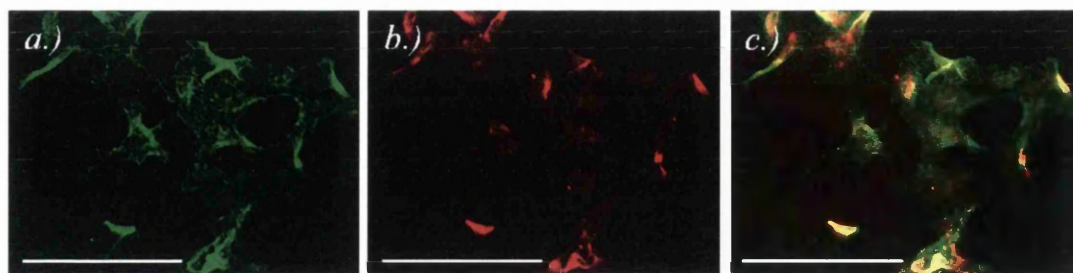


Figure 7.13: *Fluorescence microscopy images of PC-3 cells. (a) ZO-1 proteins are identified by green fluorescence. (b) E-cadherin identified by red fluorescence. (c) Composite image showing relative position of proteins. Scale bar approximately $100\mu\text{m}$.*

Samples were then examined using SNOM to acquire the topography and optical images. Typical SNOM acquisitions of dual labelled PC-3 cells are shown in Figure 7.14. The topographic image is shown in Figure 7.14(a) and reveals a single cell whose nucleus (labelled by N) is clearly distinguished. Measurements show that the maximum height of this cell is reached over the nuclear region which equates to approximately 890 nm. The lamellipodium (labelled by L) can be seen and was found to span an area of approximately $90\mu\text{m}^2$. A large cellular protrusion is visible on the cell and is identified by the label *L* on the image. Large branch-like structures were also present in other scans of PC-3 cells (Figure 7.11). Measurements indicate a width of $6.2 \pm 0.1\mu\text{m}$ at its point of origin.

Corresponding SNOM fluorescence acquisitions are shown in Figures 7.14(b) and (d). These images were obtained using the optical band pass filters to spectrally separate the fluorescence originating from each colour quantum dot and distinguish between E-cadherin and ZO-1. Subsequent zooms were generated by the software to enable regions of interest to be resolved in more detail as seen in Figures 7.14(c) and (e).

To image the location of E-cadherin proteins, which were labelled by red emitting quantum dots, the total signal was collected and passed through a Raman edge filter to eliminate the light from the laser. The remaining light was subsequently passed through a 609 nm band pass filter to remove any unwanted green fluorescence and directed towards an APD. An APD collection time of 20 ms per pixel was used to obtain the resulting image of E-cadherin which is shown in

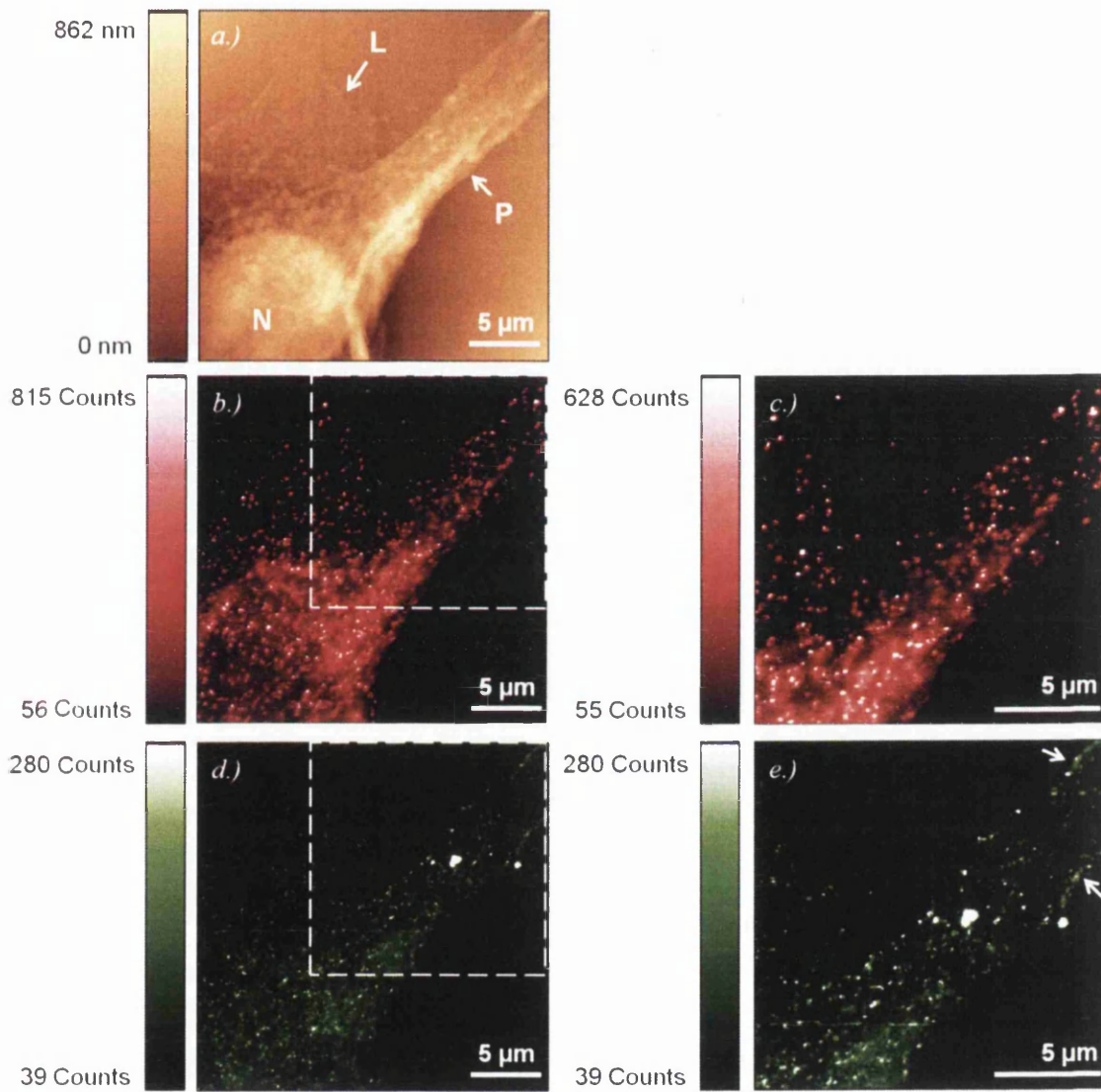


Figure 7.14: (a), (b) and (d) $(25 \mu\text{m})^2$ SNOM acquisitions of dual labelled PC-3 cells. (a) Topography image showing nucleus (labelled by N), lamellipodium (labelled by L) and cellular protrusion (labelled by P). Corresponding fluorescence images showing (b) E-cadherin and (d) ZO-1 localisation. Boxed regions in (b) and (d) zoomed in to produce images (c) and (e) respectively. ZO-1 clearly present along edge of cellular protrusion (identified by arrows). (a), (b) and (d) are $(25 \mu\text{m})^2$, (c) and (e) are $(16.7 \mu\text{m})^2$.

Figure 7.14(b). The image shows a strong fluorescence response from the sample with good signal-to-noise levels. This demonstrates the efficiency of the chosen filter at eliminating unwanted background without affecting the quality of the desired fluorescence signals.

Strong fluorescence signals are evident predominantly around the perimeter of the nucleus but are also found to extend some way along the length of the protrusion. This can be seen more clearly in Figure 7.14(c) which represents a zoom of the boxed region in Figure 7.14(b). This fluorescence represents the specific labelling of E-cadherin. Although present in this cell, the correct functioning of E-cadherin requires that it be located in regions where cell-cell contact will occur. However there appears to be no obvious E-cadherin labelling pattern around the boundary of the cell. During the study of the healthy epithelial cell line PNT2, although E-cadherin was observed to some degree around the nucleus, it was primarily found along the cell boundaries and to extend throughout the length of their numerous filopodia. This was typically observed even when contact between neighbouring cells had yet to be established.

A further SNOM acquisition was obtained to examine the localisation of ZO-1 proteins which were immunolabelled by green emitting quantum dots. Thus the 609 nm band pass filter was exchanged for a 525 nm band pass filter in order to eliminate unwanted red fluorescence from the optical signal. The APD collection time remained at 20 ms per pixel and the resulting image of ZO-1 is shown in Figure 7.14(d). The signal-to-noise levels achieved with the green quantum dots are noticeably reduced compared to that achieved by red quantum dots. This is likely to be due to the green quantum dots having a slightly lower quantum yield.

Comparison of the ZO-1 fluorescence image (Figure 7.14(d)) with the topography (Figure 7.14(a)) reveals large amounts of non-specific labelling, particularly over the region of the cell that corresponds to the nucleus. Closer inspection of the boxed region in (d) was facilitated by generating the software zoom shown in image (c). This region corresponds to the large cellular protrusion that was identified in the associated topographic image. Fluorescence can now more clearly be identified along both edges of the structure and is identified by arrows in the

image. This fluorescence along the edge of the cellular protrusion reveals the localisation of ZO-1 on the cell membrane.

7.7 Conclusion

Following investigations of adhesion mechanisms in the healthy epithelial cell line PNT2 in Chapter 6, a dual labelling methodology has been developed to facilitate the study of adhesion molecules in other cell lines. Although publications by numerous other groups have successfully applied quantum dots to multiplexing studies [11, 13–15], significant difficulties were encountered in this work. Extensive optimisation of this protocol was necessary in order to generate high-quality fluorescent samples and many preparation aspects were taken into consideration during this procedure.

For the purpose of this study, labelling of ZO-1 was carried out purely to ensure optical detection in our SNOM instrument was optimal in the event E-cadherin was not detected. Thus to address the difficulties encountered during dual labelling, E-cadherin proteins were immunolabelled with brighter red emitting quantum dots.

Dual labelling was subsequently achieved and used to study the localisation of E-cadherin and ZO-1 proteins in two prostate epithelial cell lines. Analysis of dual labelled PNT2 cells revealed E-cadherin to be localised predominantly along the cell periphery which appeared enhanced in regions where cell-cell contact had been established (Figure 7.9). This was consistent with studies discussed in the previous chapter, where only E-cadherin proteins were immunolabelled. Furthermore, ZO-1 proteins were found to be localised along the edge of the cell. This was clearly observed despite the quality of the ZO-1 fluorescent images being poorer than that observed for E-cadherin.

The study was extended to examine cancerous PC-3 cells. Initially the morphology of these metastatic cells was analysed through the acquisition of SNOM topography images. PC-3 cells were found to differ in structure to healthy epithelial cells in numerous ways. Firstly, their overall shape was found to be more

irregular with some cells assuming a fibroblast-like morphology in comparison to the more rounded appearance of healthy cells. Secondly, PC-3 cells were often difficult to image due to their abrupt features. The PC-3 cells commonly possessed long cytoplasmic protrusions in addition to the filopodia routinely observed on healthy cells. Finally, examination of more confluent samples revealed that PC-3 form loose associations with neighbouring cells with few opposing filopodia interacting. Gaps were frequently observed around the periphery of the cells, in contrast to the tight seals that were observed during examination of PNT2 cells.

Dual labelling was further optimised to allow examination of E-cadherin in PC-3 cells. Current literature suggests that E-cadherin is down-regulated in PC-3 cells. However reports on the extent of this down-regulation are inconsistent. Furthermore, analysis of gene expression levels does not reveal information about the localisation of the protein for which it encodes. To this end high-resolution topography imaging of PC-3 cells was achieved in parallel to SNOM optical imaging to reveal dual labelled E-cadherin and ZO-1 proteins (Figure 7.14).

E-cadherin proteins were predominantly observed in the perinuclear region. In contrast to healthy cells, no clear fluorescence pattern was observed around the circumference of PC-3 cells in regions where E-cadherin may properly function as a mediator of cell-cell adhesion. Fluorescence corresponding to ZO-1 localisation was clearly identified along both edges of the large, cellular protrusion.

Bibliography

- [1] R. A. Morton, C. M. Ewing, A. NAGAFUCHI, S. TSUKITA, and W. B. ISAACS. Reduction of e-cadherin levels and deletion of the a-catenin gene in human prostate cancer cells. *Cancer Research*, 53(15):3585–3590, 1993.
- [2] G. Davies, W. G. Jiang, and M. D. Mason. Cell-cell adhesion molecules and signaling intermediates and their role in the invasive potential of prostate cancer cells. *Journal of Urology*, 163(3):985–992, 2000.
- [3] P. M. Furbert-Harris, D. Parish-Gause, K. A. Hunter, T. R. Vaughn, C. Howland, J. Okomo-Awich, K. Forrest, I. Laniyan, A. Abdelnaby, and O. A. Oredipe. Activated eosinophils upregulate the metastasis suppressor molecule e-cadherin on prostate tumor cells. *Cellular and Molecular Biology*, 49(7):1009–1016, 2003.
- [4] S. H. Doak. Gene expression analysis of prostatic epithelial cell lines. Private communication.
- [5] U. H. Frixen, J. Behrens, M. Sachs, G. Eberle, B. Voss, A. Warda, D. Ltehrner, and W. Birchmeier. E-cadherin-mediated cell-cell adhesion prevents invasiveness of human carcinoma cells. *The Journal of Cell Biology*, 113(1):173–185, 1991.
- [6] K. Vleminckx, L. Vakaet, M. Mareel, F. Fiers, and F. Van Roy. Genetic manipulation of c-cadherin expression by epithelial tumor cells reveals an invasion suppressor role. *Cell*, 66(1):107–119, 1991.
- [7] M. J. G. Bussemakers, R. J. A. van Moorselaar, L. A. Girolodi, T. Ichitkawa, J. T. Isaacs, M. Takeichi, F. M. J. Debruyne, and J. A. Schalken. Decreased expression of e-cadherin in the progression of rat prostatic cancer. *Cancer Research*, 52(10):2916–2922, 1992.
- [8] Q. Zhou, B. Yan, X. Hu, X.-B. Li, J. Zhang, and J. Fang. Luteolin inhibits invasion of prostate cancer pc3 cells through e-cadherin. *Molecular Cancer Therapeutics*, 8(6):1684–1691, 2009.
- [9] K. E. Sapsford, T. Pons, I. L. Medintz, and H. Mattoussi. Biosensing with luminescent semiconductor quantum dots. *Sensors*, 6:925–953, 2006.
- [10] X. Michalet, F. F. Pinaud, L. A. Bentolila, J. M. Tsay, S. Doose, J. J. Li, G. Sundaresan, A. M. Wu, S. S. Gambhir, and S. Weiss. Quantum dots for live cells, in vivo imaging and diagnostics. *Science*, 307(5709):538–544, 2005.

-
- [11] X. Wu, H. Liu, Q. Liu, K. N. Hayley, J. A. Treadway, J. P. Larson, N. Ge, F. Peale, and M. P. Bruchez. Immunofluorescent labelling of cancer marking her2 and other cellular targets with semiconductor quantum dots. *Nature Biotechnology*, 21(1):41–46, 2003.
- [12] B. O. Dabbousi, J. Rodriguez-Viejo, F. V. Mikulec, J. R. Hines, H. Mattoussi, R. Ober, K. F. Jensen, and M. G. Bawendi. (cdse)zns core-shell quantum dots: Synthesis and characterization of a size series of highly luminescent nanocrystallites. *Journal of Physical Chemistry*, 101(46):9463–9475, 1997.
- [13] E. Sweeney, T. H. Ward, N. Gray, C. Womack, G. Jayson, A. Hughes, C. Dive, and R. Byers. Quantitative multiplexed quantum dot immunohistochemistry. *Biochemical and Biophysical Research Communications*, 374(2):181–186, 2008.
- [14] D. H. Huang, X. H. Peng, L. Su, D. S. Wang, F. R. Khuri, D. M. Shin, and Z. Chen. Comparison and optimization of multiplexed quantum dot-based immunohistofluorescence. *Nano Research*, 3(1):61–68, 2010.
- [15] J. Liu, S. K. Lau, V. A. Varma, R. A. Moffitt, M. Caldwell, T. Liu, A. N. Young, J. A. Petros, A. O. Osunkoya, T. Krogstad, B. Leyland-Jones, M. D. Wang, and S. M. Nie. Molecular mapping of tumor heterogeneity on clinical tissue specimens with multiplexed quantum dots. *ACS Nano*, 4(5):2755–2765, 2010.
- [16] R. Newman, G. W. Butcher, B. Bullard, and K. R. Leonard. A method for determining the periodicity of a troponin component in isolated insect flight muscle thin filaments by gold/fab labelling. *Journal of Cell Science*, 101(3):503–508, 1992.
- [17] <http://www.invitrogen.com/site/us/en/home.html>.
- [18] S. H. Lang, R. M. Sharrard, M. Stark, J. M. Vilette, and N. J. Maitland. Prostate epithelial cell lines form spheroids with evidence of glandular differentiation in three-dimensional matrigel cultures. *British Journal of Cancer*, 85(4):590–599, 2001.
- [19] S. H. Doak, D. Rogers, B. Jones, L. Francis, R. S. Conlan, and C. Wright. High-resolution imaging using a novel atomic force microscope and confocal laser scanning microscope hybrid instrument: essential sample preparation aspects. *Histochem. Cell. Biol.*, 130(5):909–916, 2008.
- [20] S. H. Lang, C. Hyde, I. N. Reid, I. S. Hitchcock, C. A. Hart, A. A. G. Bryden, J. M. Vilette, M. J. Stower, and N. J. Maitland. Enhanced expression of vimentin in motile prostate cell lines and in poorly differentiated and metastatic prostate carcinoma. *Prostate*, 52(4):253–263, 2002.

Chapter 8

Conclusions

8.1 Comparison of E-cadherin distribution in prostate epithelial cells.

Cellular adhesion plays an important role in maintaining the architecture of tissues and organs and is vital for their correct functioning. Abnormal cell-cell adhesion has implications in the onset of many illnesses and diseases. A concerted effort has been made by many researchers to determine the relationship between cellular adhesion and the metastatic capacity of many cancers [1].

E-cadherin is one of the principle mediators of cell-cell adhesion in epithelial tissues and has been extensively examined to determine its role in cancer progression and metastasis [2–4]. This relationship may be particularly relevant to prostate cancers which have a propensity to metastasise and form additional tumours in the bones and lymph nodes, resulting in a poor patient prognosis. As such E-cadherin has been proposed as a potential histological marker to help evaluate the prognosis of patients affected by prostate cancer and determine the most appropriate course of treatment [3–6]. Additionally, a more detailed understanding of adhesion mechanisms could lead to the development of novel cancer treatments as indicated by the preliminary studies carried out by Zhou *et al.* [7]

Although significant efforts have been made towards understanding the role of E-cadherin in the progression of prostate cancer, researchers have not reached

a consensus [8, 9]. Additional studies are required to develop a deeper understanding of the mechanisms involved in E-cadherin mediated adhesion.

To this endeavour, this investigation has examined and compared the localisation of E-cadherin in two prostate epithelial cell lines using high resolution SNOM. Antibodies against the adhesion protein E-cadherin were utilised to indirectly label cells.

Analysis of healthy epithelial PNT2 cells at various stages of epithelial sheet formation revealed that E-cadherin is predominantly located along the cell periphery. During the early stages of cell-cell adhesion E-cadherin was found to concentrate at the base of filopodia and with some extension through their length that appeared enhanced when cell-cell contact was established. This was further demonstrated by the punctate clusters of E-cadherin which were observed when filopodia established contact and appeared to embed into the neighbouring cell, initiating cell-cell adhesion. These results support the observations of Vasioukhin *et al.* [10] during investigations of actin and E-cadherin dynamics during epithelial sheet formation in epidermal cells.

High-resolution topographic analysis of PNT2 cells revealed the “quilted” nature of the filopodia surface as described by Doak *et al.* [11]. Furthermore the topography images provided a snapshot of the filopodia engaged in their sensing and exploratory roles. No filopodia were observed when cells had established full contact. Instead a tight seal between neighbouring cells had developed and multiple ridges were found to run parallel to the cell-cell boundaries which we propose represent the circumferential actin belt described by Yonemura *et al.* [12].

These results are in contrast with the observations of PC-3 cells. Examination of the morphology of PC-3 cells through topographic SNOM acquisitions revealed a markedly different appearance to that which was observed on PNT2 cells. Their overall shape was more irregular, and PC-3 cells did not form the typical cobblestone appearance that is characteristically seen in epithelial tissues.

8.1. COMPARISON OF E-CADHERIN DISTRIBUTION

Moreover, some cells appeared more fibroblast-like with long cytoplasmic protrusions, while few fine filopodia were observed. When confluent PC-3 cells were examined, the cells were found to form very loose contacts with their neighbours and large gaps were observed between cells. This was in contrast to the tight seals formed by the healthy PNT2 cells. The morphology of PC-3 cells observed in this study using SNOM confirms earlier work by Lang *et al.* [13]. Fluorescence SNOM acquisitions revealed E-cadherin to be predominantly localised around the nuclear region of cells, with no obvious E-cadherin labelling pattern around the periphery of the cells. These results are exemplified by Figure 8.1 which shows a direct comparison of the distribution of E-cadherin in PNT2 and PC-3 cells.

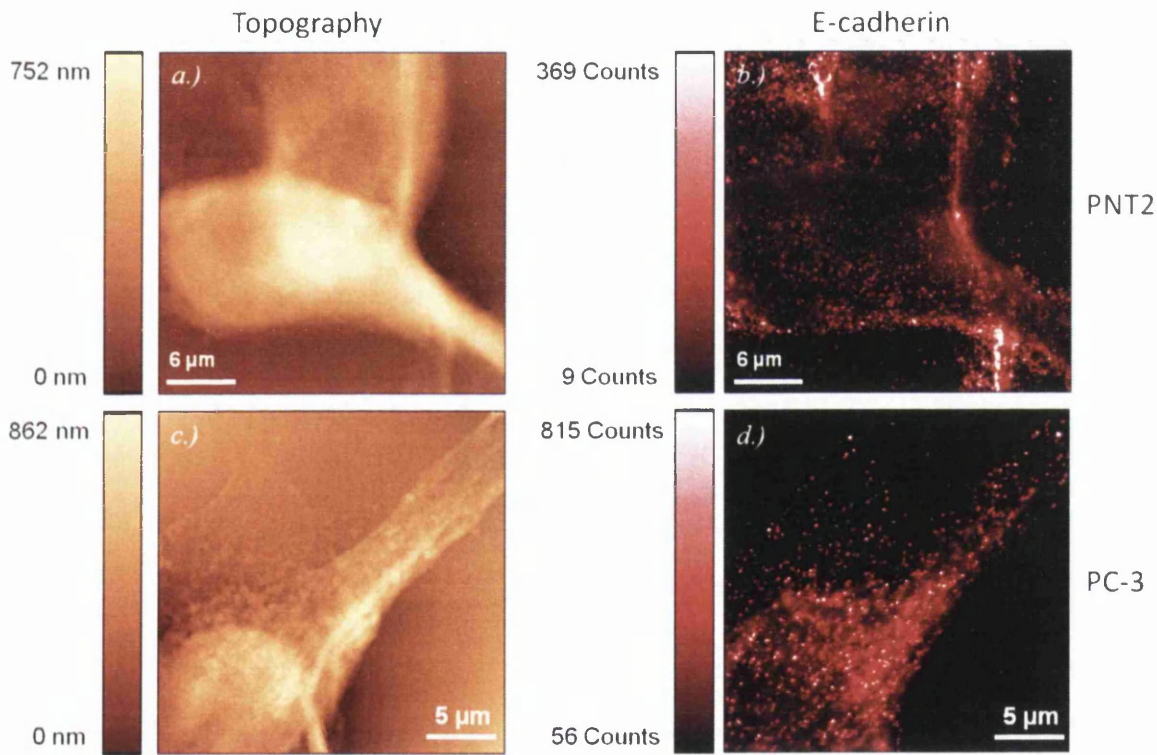


Figure 8.1: Typical SNOM acquisitions comparing E-cadherin localisation in prostate epithelial cell lines PNT2 and PC-3. PNT2 topography (a) and fluorescence SNOM (b) images showing E-cadherin proteins are found along the cell edge and is enhanced when cell-cell contact has been established. PC-3 topography (c) and fluorescence (d) images showing E-cadherin predominantly localised around the nuclear region of the cell. No obvious E-cadherin labelling pattern is observed at the cell boundary in PC-3 cells.

As presented in Chapter 7, E-cadherin can clearly be observed around the

periphery of the PNT2 cells in Figure 8.1(b) and is enhanced in regions of cell-cell contact. Whereas in PC-3 cells, E-cadherin is primarily found around the nuclear region of the cell. This lack of functional E-cadherin in PC-3 cells is likely to be the reason that confluent cells were not observed to form tight cell-cell associations with their neighbours.

This study has led to a greater understanding of the cell-cell adhesion mechanisms in epithelial tissues and how aberrations manifest in the morphology and phenotype of cancer cells. This research further highlights the role that E-cadherin plays in the development of invasive, metastatic cancer.

8.2 Multiplexed detection using quantum dots

In order to fully exploit the high-resolution capabilities afforded by SNOM, sample preparation methods proved to be vital. The protocols developed during this study were fully optimised and rigorously tested. Multiple fluorescence labelling methodologies were evaluated.

Two fluorescent labelling routes were explored; Alexa Fluor 488 and semiconductor quantum dots. The Alexa Fluor labelled samples demonstrated poor signal-to-noise levels of approximately 3.6 and were subject to rapid fading, limiting the extent of analysis of any one region. The quantum dots proved to be significantly brighter and more robust and facilitated multiple scans of the same region, with minimal degradation. Consistently high signal-to-noise levels were observed for samples labelled with quantum dots, even following repeated examination. Signal-to-noise values of greater than 10 were frequently observed.

Adhesion mechanisms in PNT2 cells were successfully analysed through labelling of E-cadherin. However to analyse PC-3 cells using SNOM, a dual labelling approach was necessary to confirm detection instruments were fully optimised. This was particularly important because reduced levels of fluorescence, due to reduced expression of E-cadherin, were expected. As discussed in Chapter 4, E-cadherin expression levels in PC-3 cells have been analysed in numerous other studies. Work by Doak *et al.* [14] has shown through real-time RT-PCR, that

E-cadherin gene expression is downregulated in PC-3 cells. A study by Morton *et al.* [15] detected reduced amount of E-cadherin proteins in PC-3 cells compared to normal expression using Western blotting. The techniques used in these studies show the presence of either RNA (real-time RT-PCR) or the presence of the protein itself (Western blotting). However, neither of these techniques yield information about the location of E-cadherin, and consequently whether it is functional in its role as a cell-cell adhesion mediator. While fluorescence techniques have been employed in other studies in an effort to determine the localisation of E-cadherin in PC-3 cells [13, 16]. However, the techniques utilised do not provide the high-resolution fluorescence imaging afforded by SNOM, nor do they yield the complimentary ultra-structural information required to assess functionality.

This investigation has combined quantum dot dual labelling and the high-resolution imaging capabilities of SNOM to compare E-cadherin localisation in two cell lines. A clear difference has been observed in the morphology and phenotype between healthy PNT2 cells and cancerous PC-3 cells. However, other proteins involved in the formation of adherens junctions, for example α , β , γ -catenins, have not been assessed. As such the reason for the loss of E-cadherin function has not been determined.

8.3 Difficulties addressed

Few reports in the literature have described the potential problems that may be encountered when attempting to multiplex with quantum dots. Reports by other research groups indicate that the major obstacle when utilising multiplexing techniques is the length of time it takes to generate samples. Significant difficulties were encountered during this study when optimising the dual labelling protocol and poor fluorescence signals were observed, particularly from the green fluorescent quantum dots. Numerous routes were explored in an effort to determine the cause of this. This problem was addressed by switching to red emitting

quantum dots for the labelling of E-cadherin, the protein of interest. Red emitting quantum dots are more efficient at absorbing the excitation wavelength used in this work and have a higher quantum yield than quantum dots which emit green fluorescence. This provided a suitable solution and enabled the study of E-cadherin to proceed. However, in other dual labelling studies where a quantitative analysis of protein expression is required, researchers would need to consider the difference in absorption efficiency and emission efficiency of different colour quantum dots.

Preparation of samples and subsequent imaging using SNOM was labour intensive. As such it was necessary to examine samples using fluorescence microscopy to confirm labelling had been successful. Two methods were developed to facilitate examination of each sample using fluorescence microscopy and SNOM. Both methods afforded advantages and disadvantages. The limitations of each of these methods are summarised below.

- **Customised slides to facilitate fluorescence microscopy prior to SNOM:** Enabled a fast and thorough analysis of the sample via a simple adaption which preserved topographic structure. However the same region of the sample is not imaged with both fluorescence microscopy and SNOM.
- **Far-field illumination of samples using SNOM instrumentation:** Enabled selection of region of interest to be scanned using SNOM. However the set-up is time consuming to implement. The far-field images are of a lower quality than the fluorescence microscopy images.

This research has highlighted important instrument requirements that would facilitate future studies of biological samples using SNOM. An ideal equipment configuration would utilise a SNOM unit directly mounted onto an inverted fluorescence microscope. These requirements have been considered and incorporated into the specifications for SNOM instrumentation recently purchased by our research group. The design of the new SNOM will greatly enhance the ease-of-use

for other researchers pursuing SNOM studies of fluorescently labelled samples.

8.4 Future directions

Complete methodologies have been developed during this investigation to facilitate the study of adhesion mechanisms in epithelial tissues. These have been demonstrated in two cell lines and the results compared to assess the differences and similarities in morphology and phenotype of cancerous and healthy epithelial cells.

This study is in itself complete. However, there are areas of this work with the potential to be extended for a more comprehensive investigation of adhesion mechanisms. Proposed avenues of future research to compliment the work contained in this thesis are described in this section.

- Analysis of compact PNT2 cells revealed multiple distinct ridges running parallel to the cell-cell boundaries (Figure 6.12, Chapter 6). We proposed that these ridges represent the circumferential F-actin bundles described by Yonemura *et al.* [12].

To confirm this hypothesis, immunofluorescence labelling of F-actin in compact PNT2 cells is necessary. However, the limitations imposed by SNOM's low depth of illumination require an alternative method for high-resolution fluorescence imaging of such samples (e.g. PALM microscopy).

- Many protocol variations were attempted during the optimisation of a dual labelling approach. However, the cocktail method described by Sweeney *et al.* and Huang *et al.* [17, 18] was not. This "all-in-one" antibody application method may have clarified whether steric effects or repeated washing steps were having a detrimental effect on the quality of the samples. Furthermore the cocktail method would also have reduced the overall sample preparation time, making dual labelling more feasible for larger studies.
- The role of other proteins involved in the formation the adherens junction could be determined through immunofluorescence labelling. For instance

the expression and localisation of α -, β -, γ -catenins could be examined in PNT2, PC-3 and other prostate epithelial cell lines.

- The optical resolution achieved by SNOM largely depends on size of the probe aperture and can also be limited by the number of pixels used to acquire an image. However, the sensitivity of the SNOM probe to interactions with sample often resulted in the probe aperture opening during repeated scanning of samples. Thus, the loss of resolution due to opening of the SNOM probe aperture was common when attempting to zoom in in order to achieve increased resolution.

Samples could be assessed using a novel imaging approach which utilises a nanometer-sized light source to illuminate a sample. This approach is known as FRET SNOM and is realised by functionalising a SNOM probe with particles which act as FRET donors. The principles of FRET SNOM were described in more detail in Chapter 3. The use of a functionalised probe to perform FRET SNOM has been demonstrated to generate improved resolutions which are governed by the FRET radius, instead of the size of the SNOM probe aperture [19, 20]. Thus FRET SNOM could be utilised in future investigations to interrogate samples with even higher resolution than is afforded by conventional SNOM.

Bibliography

- [1] G. Davies, W. G. Jiang, and M. D. Mason. Cell-cell adhesion molecules and signaling intermediates and their role in the invasive potential of prostate cancer cells. *Journal of Urology*, 163(3):985–992, 2000.
- [2] M. J. G. Bussemakers, R. J. A. van Moorselaar, L. A. Girolidi, T. Ichitkawa, J. T. Isaacs, M. Takeichi, F. M. J. Debruyne, and J. A. Schalken. Decreased expression of e-cadherin in the progression of rat prostatic cancer. *Cancer Research*, 52(10):2916–2922, 1992.
- [3] R. Umbas, W. B. Isaacs, P. P. Bringuier, H. E. Schaafsma, H. F. M. Karthaus, G. O. N. Gosse, O. N. Oosterhof, F. M. J. Debruyne, and J. A. Schalken. Decreased e-cadherin expression is associated with poor prognosis in patients with prostate cancer. *Cancer Research*, 54(14):3929–3933, 1994.
- [4] L. Cheng, M. Nagabhushan, T. P. Pretlow, S. B. Amini, and T. G. Pretlow. Expression of e-cadherin in primary and metastatic prostate cancer. *American Journal of Pathology*, 148(5):1375–1380, 1996.
- [5] N. Morita, H. Uemura, K. Tsumatani, M. Cho, Y. Hirao, E. Okajima, N. Konishi, and Y. Hiasa. E-cadherin and alpha-, beta- and gamma-catenin expression in prostate cancers: correlation with tumour invasion. *British Journal of Cancer*, 79:1879–1883, 1999.
- [6] I. M. van Oort, K. Tomita, A. van Bokhoven, M. J. G. Bussemakers, L. A. Kiemeny, H. F. M. Karthaus, J. A. Witjes, and J. A. Schalken. The prognostic value of e-cadherin and the cadherin-associated molecules alpha-, beta-, gamma-catenin and p120(ctn) in prostate cancer specific survival: A long-term follow-up study. *Prostate*, 67(13):1432–1438, 2007.
- [7] Q. Zhou, B. Yan, X. Hu, X.-B. Li, J. Zhang, and J. Fang. Luteolin inhibits invasion of prostate cancer pc3 cells through e-cadherin. *Molecular Cancer Therapeutics*, 8(6):1684–1691, 2009.
- [8] A. A. G. Bryden, A. J. Frecmont, N. W. Clarke, and N. J. R. George. Paradoxical expression of e-cadherin in prostatic bone metastases. *British Journal of Urology International*, 84(9):1032–1034, 1999.
- [9] L. J. McWilliam, W. F. Knox, C. Hill, and N. J. R. George. E-cadherin expression fails to predict progression and survival in prostate cancer. *The Journal of Urology*, 155(Supplement 5):516A, 1996.

-
- [10] V. Vasioukhin, C. Bauer, M. Yin, and E. Fuchs. Directed actin polymerisation is the driving force for epithelial cell-cell adhesion. *Cell*, 100:209–219, 2000.
- [11] S. H. Doak, D. Rogers, B. Jones, L. Francis, R. S. Conlan, and C. Wright. High-resolution imaging using a novel atomic force microscope and confocal laser scanning microscope hybrid instrument: essential sample preparation aspects. *Histochem. Cell. Biol.*, 130(5):909–916, 2008.
- [12] S. Yonemura, M. Itoh, A. Nagafuchi, and S. Tsukita. Cell-to-cell adherens junction formation and actin filament organisation: similarities and differences between non-polarized fibroblasts and polarized epithelial cells. *Journal of Cell Science*, 108(Part 1):127–142, 1995.
- [13] S. H. Lang, R. M. Sharrard, M. Stark, J. M. Vilette, and N. J. Maitland. Prostate epithelial cell lines form spheroids with evidence of glandular differentiation in three-dimensional matrigel cultures. *British Journal of Cancer*, 85(4):590–599, 2001.
- [14] S. H. Doak. Gene expression analysis of prostatic epithelial cell lines. Private communication.
- [15] R. A. Morton, C. M. Ewing, A. NAGAFUCHI, S. TSUKITA, and W. B. ISAACS. Reduction of e-cadherin levels and deletion of the a-catenin gene in human prostate cancer cells. *Cancer Research*, 53(15):3585–3590, 1993.
- [16] S. H. Lang, C. Hyde, I. N. Reid, I. S. Hitchcock, C. A. Hart, A. A. G. Bryden, J. M. Vilette, M. J. Stower, and N. J. Maitland. Enhanced expression of vimentin in motile prostate cell lines and in poorly differentiated and metastatic prostate carcinoma. *Prostate*, 52(4):253–263, 2002.
- [17] E. Sweeney, T. H. Ward, N. Gray, C. Womack, G. Jayson, A. Hughes, C. Dive, and R. Byers. Quantitative multiplexed quantum dot immunohistochemistry. *Biochemical and Biophysical Research Communications*, 374(2):181–186, 2008.
- [18] D. H. Huang, X. H. Peng, L. Su, D. S. Wang, F. R. Khuri, D. M. Shin, and Z. Chen. Comparison and optimization of multiplexed quantum dot-based immunohistofluorescence. *Nano Research*, 3(1):61–68, 2010.
- [19] S. A. Vickery and R. C. Dunn. Scanning near-field fluorescence resonance energy transfer microscopy. *Biophysical Journal*, 76(4):1812–1818, 1999.
- [20] G. T. Shubeita, S. K. Sekatskii, G. Dietler, I. Potapova, A. Mews, and T. Basché. Scanning near-field optical microscopy using semi-conductor nanocrytals as a local fluorescence and fluorescence resonance energy transfer source. *Journal of Microscopy*, 210(3):274, 2003.

Appendix A

Approximate Quantum dot sizes (nm).

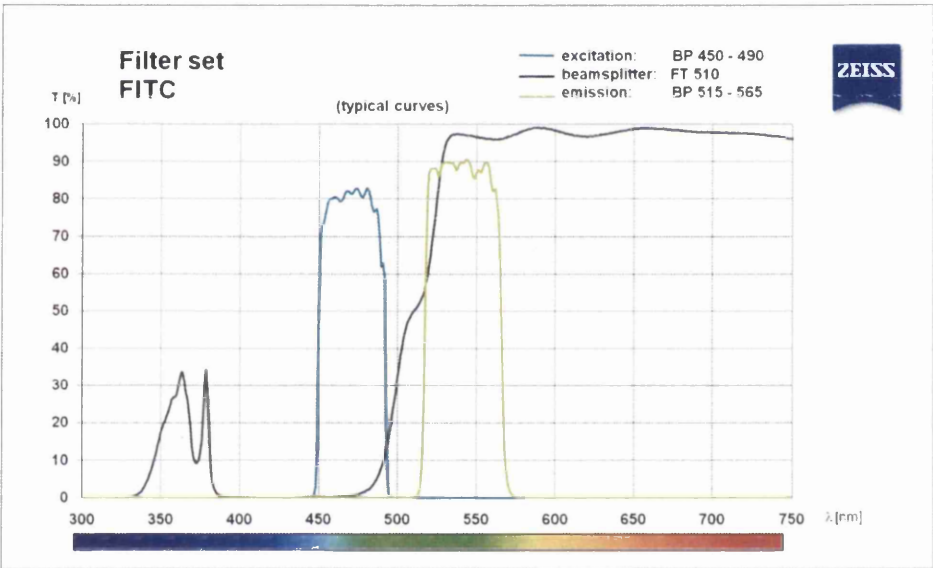
Data provided by Invitrogen ¹.

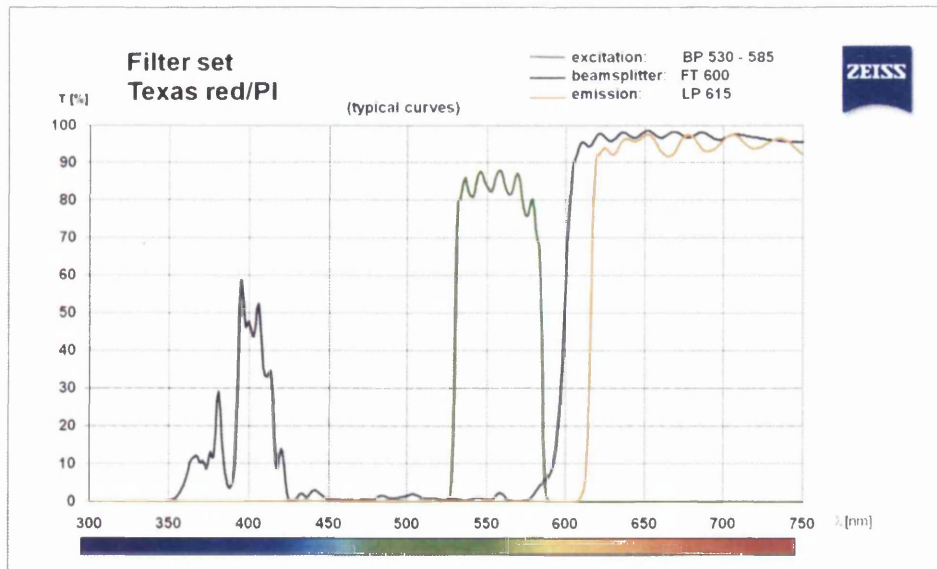
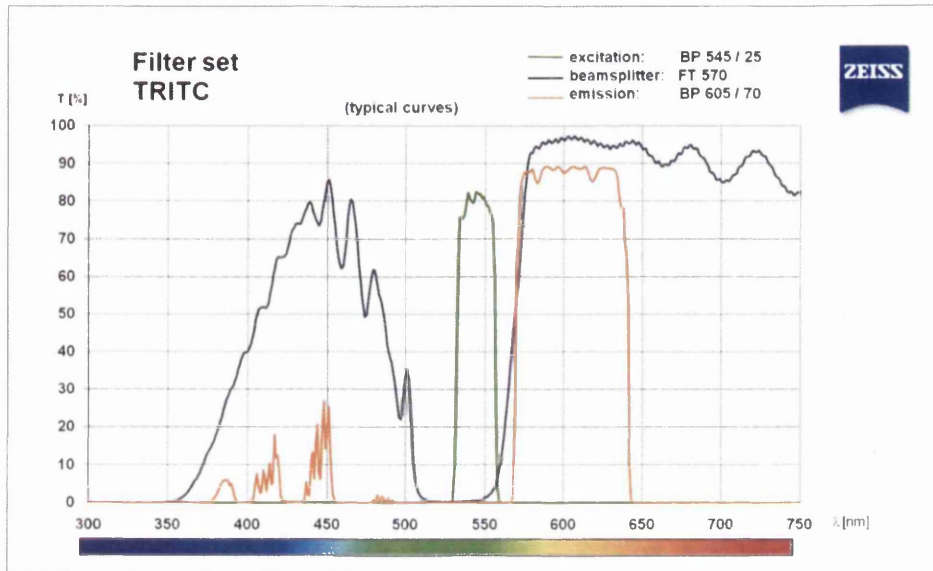
	Qdot 525	Qdot 605	Qdot 655
Core/shell	3 – 4	Ellipsoids: 4 × 9.4	Ellipsoids: 6 × 12
Core/shell composition	CdSe/ZnS	CdSe/ZnS	CdSe/ZnS
Carboxyl Qdot Nanocrystal core/shell/polymer	12	16	17
Carboxyl Qdot Nanocrystal core/shell/polymer/PEG	13	16	20

¹Private communication; Invitrogen, Paisley, UK. Specification of CdSe/ZnS quantum dots.

Appendix B

Optical properties of FITC, TRITC and PI filter sets installed on fluorescence microscope. Data provided by Zeiss Ltd.





Appendix C

Photostability of Alexa Fluor 488

Figure 8.2 illustrates the poor quality of samples fluorescently labelled with Alexa Fluor 488. SNOM topography and fluorescence acquisitions (Figures 8.2(a) and (b) respectively) are shown. The fluorescence image reveals a typical signal-to-noise value of ~ 3.6 . Subsequent topography and fluorescence acquisitions were generated to examine the boxed region in further detail. A reduction in the already low fluorescence signals is observed in fluorescence image (d). Figure 8.2 demonstrates that Alexa Fluor 488 fluorophores are unsuitable for studies requiring repeated examination of samples.

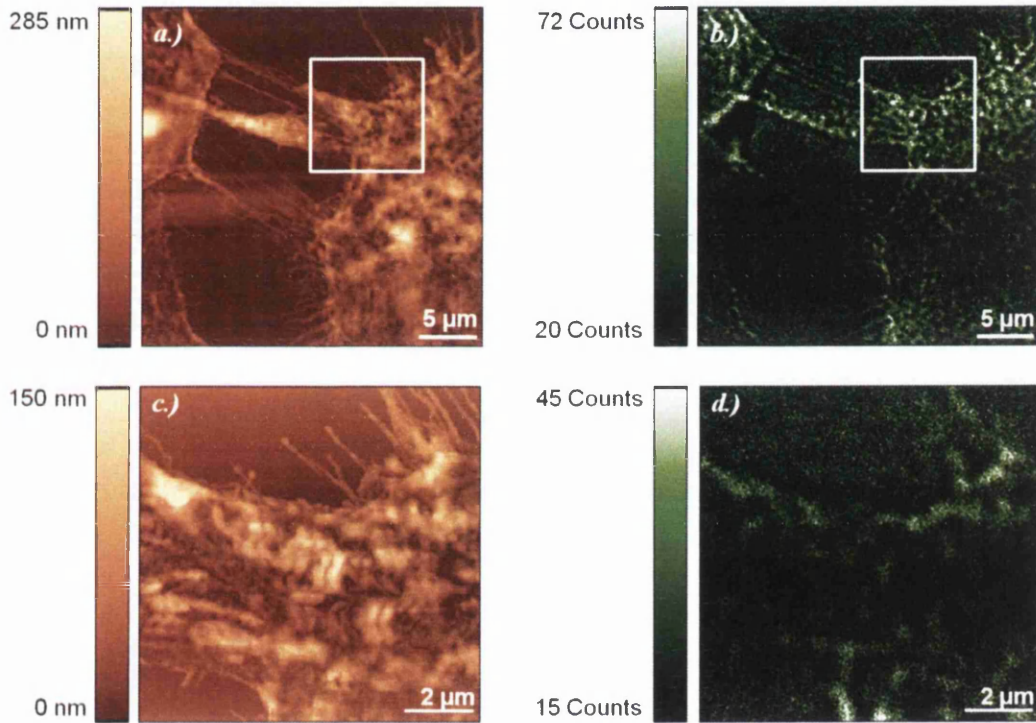


Figure 8.2: *SNOM* acquisitions of PNT2 cells labelled with Alexa Fluor 488. Boxed region in topography image (a) is further resolved in image (c). Corresponding fluorescence acquisitions (b) and (d) demonstrate a reduction in the already low signal-to-noise levels when repeated scanning of a single area is performed.

Appendix D

Mechanisms of cell-cell adhesion identified by immunofluorescent labelling with quantum dots: A scanning near-field optical microscopy approach.

K-A. D. Walker, S.H. Doak* and P.R. Dunstan

School of Physical Sciences, Dept of Physics, Multidisciplinary Nanotechnology Centre, Swansea University, Singleton Park, Swansea, SA2 8PP, UK

*Institute of Life Science, School of Medicine, Swansea University, Singleton Park, Swansea, SA2 8PP, UK

Submitted to Ultramicroscopy, 16 July 2010.

Abstract

Scanning near-field optical microscopy (SNOM) has been employed to simultaneously acquire high-resolution fluorescence images along with shear-force atomic force microscopy from cell membranes. Implementing such a technique overcomes the limits of optical diffraction found in standard fluorescence microscopy and also yields vital topographic information. The application of the technique to investigate cell-cell adhesion has revealed the interactions of filopodia and their functional relationship in establishing adherens junctions. This has been achieved via the selective tagging of the cell adhesion protein, E-cadherin, by immunofluorescence labelling. Two labelling routes were explored; Alexa Fluor 488 and semiconductor quantum dots. The quantum dots demonstrated significantly enhanced photostability and high quantum yield making them a versatile alternative to the conventional organic fluorophores often used in such a study. Analysis of individual cells revealed that E-cadherin is predominantly located along the cell periphery but is also found to extend throughout their filopodia. We have demonstrated that with a fully optimised sample preparation methodology, quantum dot labelling in conjunction with SNOM imaging can be successfully applied to interrogate biomolecular localisation within delicate cellular membranes.